Design and Analysis of an Active Noise Canceling Headrest

Jacob J. Bean

Dissertation submitted to the Faculty of the
Virginia Polytechnic Institute and State University
in partial fulfillment of the requirements for the degree of

Doctor of Philosophy
in
Aerospace Engineering

Chris R. Fuller, Co-Chair
Craig A. Woolsey, Co-Chair
Noah H. Schiller
Michael K. Philen
Cornel Sultan

March 15, 2018
Blacksburg, Virginia

Keywords: Active Headrest, Adaptive Control, Hybrid Control, Numerical Modeling

Design and Analysis of an Active Noise Canceling Headrest

Jacob J. Bean

(ABSTRACT)

This dissertation is concerned with the active control of local sound fields, as applied to an active headrest system. Using loudspeakers and microphones, an active headrest is capable of attenuating ambient noise and providing a comfortable acoustic environment for an occupant. A finite element (FE) model of an active headrest is built and analyzed such that the expected noise reduction levels could be quantified for various geometries as well as primary sound field conditions. Both plane wave and diffuse primary sound fields are considered and it is shown that the performance deteriorates for diffuse sound fields. It is then demonstrated that virtual sensing can greatly improve the spatial extent of the quiet zones as well as the attenuation levels. A prototype of the active headrest was constructed, with characteristics similar to those of the FE model, and tested in both anechoic and reverberant sound fields. Multichannel feedforward and feedback control architectures are implemented in real-time and it is shown that adaptive feedback systems are capable of attenuating band-limited disturbances. The spatial attenuation pattern surrounding the head is also measured by shifting the head to various positions and measuring the attenuation at the ears. Two virtual sensing techniques are compared in both feedback and feedforward architectures. The virtual microphone arrangement, which assumes that the primary sound field is equivalent at the physical and virtual locations, results in the best performance when used in a feedback system attenuating band-limited disturbances. The remote microphone technique, which accounts for the transfer response between the physical and virtual locations, offers the best performance for tonal primary sound fields. In band-limited sound fields, a causal relationship rarely exists between the physical and virtual microphones, resulting in poor performance.

Design and Analysis of an Active Noise Canceling Headrest

Jacob J. Bean

(GENERAL AUDIENCE ABSTRACT)

Excessive noise and vibration levels in aircraft, rotorcraft, launch vehicles, and other aerospace vehicles may create harsh acoustic environments inside the vehicle. In some extreme cases, military applications being a prime example, hearing damage can occur due to the high noise levels associated with certain vehicles. Noise canceling headsets have been proven an effective solution to this problem, although in certain instances their use may not be safe or feasible. In this work, an active noise canceling headrest, or active headrest, is explored as an alternative solution to noise canceling headphones/headsets. An active headrest uses microphones and loudspeakers, typically located non-intrusively behind the head of the seat occupant, to reduce the ambient noise levels in the vicinity of the head and create a comfortable acoustic environment. A thorough investigation of the viability of such a system in a practical vehicle is assessed through the use of theoretical analysis, finite element modeling, and real-time performance experiments. Performance predictions generated using the finite element model were verified by performing real-time experiments, thus providing a level of confidence in additional predictions for alternative headrest geometries and configurations. Factors such as loudspeaker and microphone placement, head movements away from the nominal position, primary acoustic field characteristics, and choice of control strategy are all found to heavily influence the performance of an active headrest. Real-time experiments were performed in anechoic and reverberant sound fields and it is found that the noise canceling capability of the active headrest worsens in reverberant sound fields as compared to free field conditions.

Acknowledgments

First, I would like to thank my advisor, Chris Fuller, for providing me with the opportunity to obtain this degree and for granting me a large amount of flexibility in pursuing various research directions as I saw fit. The quality of this work has significantly benefited from his input. I would also like to thank my NASA mentor, Noah Schiller, for his persistent involvement in this work throughout my tenure as a graduate student. His willingness to discuss new research ideas and provide input to my work whenever I stopped by his office dramatically helped to progress this research in a timely fashion. I also wish to thank the rest of my committee members for their involvement in this endeavor.

Next, I would like to thank all members of the Structural Acoustics Branch at NASA Langley Research Center. I appreciate the feedback that I received from numerous branch members on technical presentations and papers as well as the assistance in using many NASA facilities that I was previously unfamiliar with. I also wish to thank all faculty and staff at the National Institute of Aerospace for their involvement in helping me to complete my coursework via a distance learning program.

Last but certainly not least, I would like to thank my family and friends for their confidence and encouragement throughout this arduous process. Many times you all listened to my complaints and self-doubts and insisted that I could persevere and complete this venture. For that I will always be grateful.

Contents

List of Figures

List of Tables

Chapter 1

Introduction

Excessive noise and vibration levels in aircraft, rotorcraft, launch vehicles, and other aerospace vehicles can result in structural damage as well as create harsh acoustic environments for occupants inside the vehicle. In some extreme cases, military applications being a prime example, hearing damage can occur due to the high noise levels inside certain vehicles. A common approach to reducing the noise transmitted into the vehicle is to use porous materials, such as foam, in the vehicle walls. While this approach can be effective for high frequencies, the materials are typically incapable of attenuating the transmission of low frequency noise. For this reason, the concepts of active structural acoustic control (ASAC) and active noise control (ANC) have been suggested as alternative approaches. Active structural acoustic control is the process of manipulating the dynamic structural response of the vehicle such that the noise transmitted to the interior is reduced [1]. Active noise control, which operates on the principle of acoustic superposition, refers to the process of introducing secondary acoustic sources to destructively interfere with a primary acoustic response, hence reducing the total noise or energy level [2].

While over the ear hearing protection can be a practical and efficient solution for vehicle occupants, there are many instances in which wearing hearing protection is not feasible or safe. Partly for this reason, the concept of active noise cancellation using remotely located, non-intrusive, loudspeakers and microphones has been an active research area over the last 30 or so years. The goal is to provide significant noise reduction levels for a passenger, similar to those that would be achieved using over the ear hearing protection, with remotely located loudspeakers and microphones.

An active noise control system like the one described above is referred to as an active headrest. Loudspeakers are normally located some distance behind or to the side of the head of a passenger, often times situated directly in the headrest (hence the term active headrest), and are driven based on the outputs of nearby microphones to result in lower noise levels. This problem is significantly more challenging, acoustically as well as from a controls perspective, than ANC in a headset. This can be attributed to factors related to increased plant variability, added acoustic propagation delay, the potential need for multichannel control systems, etc. The ma-

terial in this dissertation will focus on both the control-related issues as well as the acoustic performance of such systems.

This chapter aims to provide background material relevant to the work described in the rest of the dissertation. A review of previous literature relevant to active headrests will first be presented, followed by a summary of the significant contributions and the organization of the dissertation.

1.1 Background

1.1.1 Acoustics of active noise control

Active noise control in general can be categorized as being either *global* or *local*. Global ANC systems aim to minimize the total acoustic energy in a given vehicle or enclosure such that noise reduction is achieved at all locations. In his 1936 patent [3], Paul Lueg first suggested the concept of reducing sound oscillations in a 1D acoustic duct. Using a reference transducer to detect the primary waveform, a loudspeaker located downstream of the reference transducer was driven such that the secondary and primary acoustic fields canceled one another. With this approach, global ANC was achieved at all locations downstream of the secondary loudspeaker. Mainly because of their simplicity, acoustic ducts serve as a benchmark test apparatus for testing new ANC algorithms [4, 5, 6]. To extend this idea to more complex environments, the feasibility of achieving global ANC in a modally dense 3D sound field was explored in a series of papers [7, 8, 9]. Using secondary point sources, the authors achieved global reductions in the total time-averaged acoustic potential energy. They found that, in order to obtain significant reductions in the potential energy, the secondary sources must be located sufficiently close to (less than one half wavelength) the primary disturbance source. Although some of the assumptions are idealistic, *i.e.*, diffuse primary sound field and point monopole sources, the fundamental theory has been a valuable contribution to the field of ANC.

While global noise or energy reductions can be achieved in certain scenarios, most ANC approaches focus on controlling a local acoustic sound field. Rather than attempting to reduce the energy in an entire enclosure, it may be sufficient in some scenarios to simply reduce the sound level in the vicinity of a transducer. Most ANC transducers are microphones, although intensity probes and energy density sensors have been suggested as alternatives [10, 11, 12]. A primary example of local ANC occurs in active headsets and headrests [13]. In these applications, the primary goal is to reduce the ambient noise levels for a listener. Numerous studies exploring the behavior of locally controlled sound fields have helped to contribute to the current understanding of the acoustical aspect of local ANC. For example, Elliott examined the effects of using a secondary point source to cancel the pressure at a point in a tonally diffuse sound field [14]. He demonstrated that the region around the point of cancellation in which the primary sound level was reduced by at least 10 dB, often referred to as the *quiet zone*, was

approximately equal to $\lambda/10$, where λ is the acoustic wavelength. This concept was extended in [15] to include cancellation of the pressure gradient in a diffuse field. It was found that by canceling the pressure gradient as well, which requires an additional secondary source, the 10 dB quiet zone had a radius of approximately $\lambda/2$. A number of other authors have considered the effects of pressure cancellation in the near field of a source [16] and in diffracted sound fields [17].

1.1.2 Feedforward control

Most early attempts to design ANC systems made use of feedforward control. Feedforward systems rely on the availability of a reference signal that is at least partially correlated with the primary disturbance [18, 19, 20]. This reference signal may be generated by a tachometer measuring propeller speed in an aircraft, accelerometers measuring structural vibrations in automobiles, microphones placed in the vicinity of a primary noise source, etc.

Feedforward ANC systems, due to their similarity to electrical noise cancellation systems, are often based on adaptive filtering techniques [21]. The filtered reference least mean squares (FxLMS) algorithm [4], which has enjoyed widespread use over the past few decades, is based directly on the least mean squares (LMS) algorithm for adaptive filtering [22]. Several modifications to the FxLMS algorithm, such as the modified FxLMS algorithm [23], the filtered error LMS algorithm [24], and the leaky FxLMS algorithm [2] have been shown to offer improved performance in some scenarios. Although most feedforward ANC systems are designed using adaptive filtering techniques, many authors have presented alternatives. For example, by formulating the feedforward ANC problem in a system identification framework, the authors in [25] computed an optimal feedfoward control filter using the Kalman filtering solution.

Multichannel adaptive filtering has also played a large role in multi-input multi-output (MIMO) control systems. In many cases, it is desirable to reduce signals at a number of error sensors using multiple control sources, which may be driven by multiple reference signals. The FxLMS algorithm was extended to accomodate multiple channels in [26], where the authors refer to it as the multiple error LMS algorithm. The multiple error LMS algorithm may suffer from slow convergence due to partially correlated reference signals and the dynamics and coupling in the plant response [27]. For this reason, numerous authors have explored methods of convergence improvements such as coordinate transformations [28, 29, 30] and variable step sizes [31, 32]. Convergence issues related to plant dynamics and coupling have also received a great deal of attention in the literature. When the transfer paths from different actuators to sensors are linearly dependent, the control system can become ill-conditioned, a problem referred to as collinearity [33]. These approaches typically involve taking advantage of the specific modes in structures to determine optimal locations for sensors and actuators [33, 34].

An adaptive feedforward control system was successfully implemented using an active headrest in [35]. This study was mainly focused on measuring the region around the head where a satisfactory level of noise reduction had been achieved and less so on details of the control

system implementation. They found that using an adaptive feedforward controller, which was based on the LMS algorithm, no appreciable noise reduction was achieved unless the error microphones are located inconveniently close to the ears. Using a virtual microphone [36], the authors found that the 10 dB quiet zone extends approximately 8 cm forward and 10 cm laterally for frequencies less than about 500 Hz.

Paul Lueg's patent [3], mentioned earlier, is also an example of a feedforward ANC system where the reference microphone is located in an acoustic duct, upstream of the secondary loudspeaker. Feedforward control systems have also been successful in controlling vibrations on various structures such as thin beams [37], vibrating panels [38], and cylindrical models of an aircraft fuselage [39, 28].

1.1.3 Feedback control

The concept of an active headrest was first suggested in 1953 by Olson and May [40]. They described a device which consists of a closely spaced microphone-loudspeaker pair. Employing an analog feedback control circuit that was adjusted to minimize the output signal from the microphone, they found that reductions of 10-25 dB were achievable at low frequencies. Applications of such a device in the headrest of aircraft or automobile seats were discussed as well.

Since then, numerous other authors have published studies proposing the use of active headrests in automobiles [41], aircraft [42], rotorcraft [43], railway sleeping cars [44], and luxury yachts [45]. In most of the literature on active headrests, feedback control systems [46] are employed because it is argued that a suitable reference signal would not be available for a general purpose active headrest. However, this is not to say that active headrests designed for specific conditions would not be viable.

Both fixed and adaptive feedback control systems have been proposed for use in active headrests. Using a mixed H_2/H_∞ optimization approach, the authors in [47] designed a fixed feedback control system for an active headrest. The controller minimized the mean squared signal at the error sensor while satisfying constraints on the stability and robustness of the system. A total attenuation of 15.2 dB was achieved at the point of cancellation, which was located $\approx$10 cm away from the manikin ear, for a broadband disturbance with a bandwidth of about 200-400 Hz. This approach was extended in [48] to include the use of a virtual microphone located at the manikin ear. Using a similar design method for the fixed feedback controller, reductions of about 9.5 dB at microphones located in the ears of a manikin head were achieved. The method of controller design employed in these studies is particularly useful, as frequency domain bounds related to spillover and system stability can be prescribed at the outset of the design.

The behavior of multichannel adaptive feedback control systems in an active headrest were analyzed in [49, 50]. The author demonstrated that multichannel systems perform better than separate single channel systems, although this may be less true for non-adaptive systems such

as those described in the previous paragraph. The feedback controllers were implemented using internal model control and a variant of the FxLMS algorithm [51] to adapt the control filters. It was shown that the control system was effective in attenuating tonal disturbances. The use of a virtual microphone was also considered and shown to result in improved attenuation at the ears of a subject.

Most feedback systems in the literature have employed an internal model architecture [52], however some authors have explored various frequency estimation techniques as a method to synthesize a reference signal for the feedback filter [53, 54, 55, 56, 57]. Feedback systems employing internal model control (IMC) are typically susceptible to out of bandwidth noise amplification, or spillover, so classical methods such as loop shaping and more recent H_∞ methods have also been considered to minimize spillover and improve robustness [58, 59, 60, 61, 5]. Some methods that do not require any model of the plant have also been considered, and are typically based on adapting the control filter based on a gradient estimated using a finite difference approximation of the error surface [62, 63, 64, 65].

1.1.4 Hybrid control

Systems comprised of both feedforward and feedback controllers are referred to as hybrid control systems. Most hybrid control systems reported in the literature consist of a feedforward control filter, which is driven by the upstream reference signal, and a feedback control filter, which is driven by an estimate of the disturbance [66, 67, 68]. The estimate of the disturbance signal is generated using an internal plant model [52] and both filters are updated according to the filtered reference LMS algorithm [4].

Hybrid control systems have been implemented in infant incubators [69], headsets [70, 71, 72], motorcycle helmets [73], and in rooms [74]. The main benefit that hybrid systems offer over feedforward systems is improved noise reduction for uncorrelated narrowband disturbances [75, 76]. In scenarios where the disturbance contains spectral components that are not correlated with the reference, the feedback controller aims to minimize the uncorrelated components. This type of architecture has been shown to be successful for uncorrelated tones, although improvements for uncorrelated broadband components are limited [75].

1.1.5 Virtual sensors

In most active headrests, the error sensors are located away from the ears as to not interfere with an occupant's head movements. When the control system minimizes the pressure at the error sensors, as is done in traditional ANC, a comparable level of attenuation will only be achieved at the ears if the distance between the error sensor and the ear is small compared to the wavelengths of the primary field. In most cases, this distance is not small enough and methods of *shifting* the region of maximum attenuation, or the quiet zone, have been devised. The location

of the virtual microphone typically coincides with the ear.

The virtual microphone arrangement [36] was the first proposed virtual sensing algorithm for ANC. The virtual microphone arrangement makes the simple assumption that the primary acoustic field is equal at the physical and virtual microphones. For distances that are small compared with the acoustic wavelength, this is typically a valid assumption. This algorithm was used in the virtual sensing approach in [35] and resulted in significantly improved noise reduction. The remote microphone technique [77], which can be viewed as an extension of the virtual microphone arrangement, uses an additional filter to estimate the primary disturbance at the virtual location. For tonal disturbances and perfect transfer function estimates, the remote microphone technique is capable of generating a perfect estimate of the pressure at the virtual location [78, 79]. It should be noted that this is only true for predictable sound fields. If the primary field is diffuse, the extra filter needed to estimate the virtual pressure will be described by statistically averaged quantities and hence will not result in a perfect estimate for any particular diffuse field realization. A major limitation of the remote microphone technique is that a causal relationship must exist between the physical and virtual microphones. What this means is that the physical microphone must provide *time-advanced* knowledge of the disturbance spectra such that a linear causal filter can be realized that accurately describes the physical microphone-virtual microphone input-output relationship. The performance of an active headrest employing the remote microphone technique was described in [80] and was shown to offer better performance, for a tonal disturbance, than the same system employing the virtual microphone arrangement.

Numerous other virtual sensing algorithms have been proposed such as the forward difference prediction technique [81], the adaptive LMS virtual microphone technique [82], the Kalman filtering virtual sensing algorithm [6], and the stochastically optimal tonal diffuse sound field virtual sensing technique [83]. A comprehensive review of these virtual sensing algorithms can be found in [79].

1.2 Scope and objectives

Several objectives related to advancing the current state of the art for active headrest design were set forth at the outset of this research project. These objectives involved investigating the performance of an active headrest through the use of theoretical, simulation, and experimental tools. The main contributions fromthis work are outlined below.

- Combine the feedforward and feedback control paradigms to form exact/complete expressions for the update mechanisms in single and multichannel hybrid control systems.
- Development a finite element model of an active headrest and evaluate the noise reducing capabilities of the system for various combinations of control actuators/error sensors, listener head positions, and primary sound field characteristics.

- Development of single and multichannel adaptive control systems that can be deployed in real-time to evaluate the performance benefits and limitations associated with various control approaches.
- Design, construction, and real-time testing of an active headrest prototype in anechoic (free field) and fully reverberant (diffuse field) acoustic environments.
- A *comprehensive analysis* of active headrest systems that considers the interaction of control system performance and the local controlled acoustic environment aswell as the benefits and limitations associated with using virtual sensing approaches.

As stated above, a major contribution of this work is the comprehensive investigation of active headrest performance under a broad series of conditions. Table 1.1 provides an overview of the experimental tests performed with the active headrest. The purpose of testing the headrest in anechoic and fully reverberant acoustic environments was to quantify the performance limits for opposite ends of the acoustic spectrum. Test results in anechoic conditions correspond to a heavily damped environment where only the direct field from a noise source is present and the effects of sound wave reflections are minimal. Fully reverberant conditions represent a scenario where multiple spatially separated uncorrelated noise sources are present. In each acoustic environment, feedforward and feedback control systems were evaluated for both tonal and band-limited primary disturbances. Band-limited disturbances were considered to investigate the implications of using feedback control systems and certain virtual sensing techniques to attenuate disturbances with finite bandwidths. These implications, as will be discussed in further detail later, are not evident when simply considering tonal disturbances as many prior studies have done. For every test case listed in Table 1.1, the spatial extent of the quiet zone was measured by shifting a manikin head to various positions and measuring the corresponding noise reduction at the in-ear microphones. This method of measuring the quiet zone varies from past approaches where microphone arrays are used to probe the controlled local sound field around the head. In this way, plant variations are taken into account directly in the measurement and hence lead to more accurate noise reduction predictions. Two virtual sensing algorithms, which are used with the intention of improving attenuation at the ears of a listener, are compared to conventional active noise control and benefits and limitations of their use in spatially complex and band-limited primary sound fields are presented. A final test, not listed in the table, was performed with the active headrest prototype located in a semi-reverberant acoustic environment. For this test, a combined feedforward-feedback control system was employed such that spectral components of the disturbance for which a correlated reference signal was not available could still be attenuated. This experiment serves as, to the best of our knowledge, the first demonstration of hybrid active noise control in an active headrest

Table 1.1: Test matrix for experimental evaluation of the active headrest

	Test environment	
	Anechoic	Fully reverberant
Feedforward	*Tonal* • Cancellation at physical error sensors • Virtual sensing using the virtual microphone arrangement • Virtual sensing using the remote microphone technique *Band-limited* • Cancellation at physical error sensors • Virtual sensing using the virtual microphone arrangement • Virtual sensing using the remote microphone technique	*Tonal* • not applicable *Band-limited* • not applicable
Feedback	*Tonal* • Cancellation at physical error sensors • Virtual sensing using the virtual microphone arrangement • Virtual sensing using the remote microphone technique *Band-limited* • Cancellation at physical error sensors • Virtual sensing using the virtual microphone arrangement • Virtual sensing using the remote microphone technique	*Tonal* • not applicable *Band-limited* • Cancellation at physical error sensors • Virtual sensing using the virtual microphone arrangement • Virtual sensing using the remote microphone technique

1.3 Organization

This dissertation contains information relevant to the design and analysis of a practical active headrest system. Chapter 2 presents background material pertinent to theoretical and experimental results presented throughout the remainder of the dissertation. In Chapter 3, a detailed derivation of the update mechanism in a hybrid control system is presented. Both single and multichannel algorithms are presented, along with some simulation results that demonstrate the advantages and limitations of the proposed algorithm. The finite element model of the active headrest is then presented in Chapter 4. In Chapter 5, specifics detailing the experimental procedure and findings are outlined. Chapter 6 concludes the dissertation and provides some insight into future research directions.

Chapter 2

Adaptive Filtering and Active Control Preliminaries

This chapter includes background material relevant to topics discussed in the remainder of the dissertation. First, a brief overview of adaptive filtering will be presented. Derivations of the LMS algorithm for adaptive FIR filtering and the recursive prediction error (RPE) algorithm for adaptive IIR filtering are included due to their relevance to many of the active control algorithms discussed in later chapters. Specifically, the derivation of the adaptive combined feedforward-feedback control algorithm in Chapter 3 is based on the derivation of the RPE algorithm. Next, the single channel filtered-reference LMS and multiple error LMS algorithms will be presented. A description of tonal active control systems is also included as this has relevance to the numerical modeling analysis of an active headrest in Chapter 4. Lastly, some basic concepts from feedback control, with a main focus on the internal model principle, will be presented. Each of these topics could easily warrant their own chapter, but it is the objective of this chapter to provide only details necessary to understand the work presented in the remainder of this dissertation. Many of the details in this chapter can be found in [2], although additional references are provided throughout the chapter.

2.1 Adaptive FIR filtering

Consider the finite impulse response filter shown in Figure 2.1. The output $y(n)$ is given by the summation of the filter weights with delayed samples of the input signal such that

$$y(n) = \sum_{i=0}^{I-1} w_i x(n-i). \tag{2.1}$$

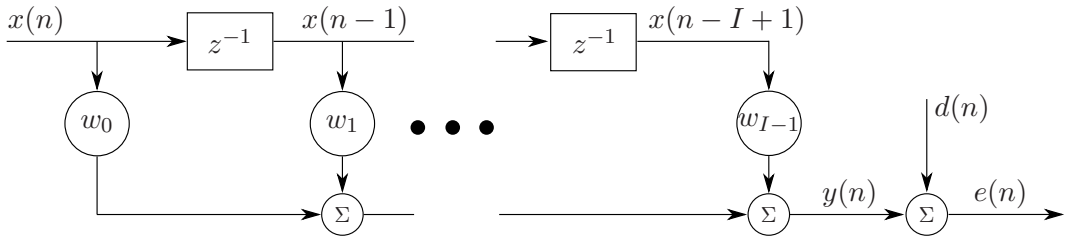

Figure 2.1: Structure of a finite impulse response filter with input signal $x(n)$, output signal $y(n)$, desired signal $d(n)$, and filter weights w_i.

If the elements w_i and past samples of the reference signal are stored in vectors, the output can be written in vector form as

$$y(n) = \boldsymbol{w}^T \boldsymbol{x}(n) = \boldsymbol{x}^T(n)\boldsymbol{w}, \tag{2.2}$$

where $\boldsymbol{w}$ is a vector of filter coefficients and $\boldsymbol{x}(n)$ is a vector of the past $I-1$ reference signal samples.

The objective in a generic transversal filtering problem is to adjust the filter coefficients such that the filter output matches a known desired signal $d(n)$. This can be accomplished by computing the optimal Wiener filter, which minimizes the expected value of the mean squared error signal. Since this work is primarily concerned with adaptive control, the adaptive filtering approach is the only that will be discussed. In this section, the only adaptive FIR filtering algorithm that will be presented is the LMS algorithm, as it is pertinent to the understanding of the adaptive control algorithms in later sections.

2.1.1 LMS algorithm

For the transversal filtering problem shown in Figure 2.1, the LMS algorithm [22] iteratively adjusts the coefficients w_i, based on the method of steepest descent, such that the instantaneous squared error signal $e^2(n)$ is minimized. The error signal is the difference between the filter output and the desired signal and is given by

$$e(n) = d(n) - \boldsymbol{x}^T(n)\boldsymbol{w}. \tag{2.3}$$

The cost function is defined by the instantaneous value of the squared error signal,

$$J = e^2(n), \tag{2.4}$$

and is quadratic in the filter coefficients w_i, ensuring the existence of a unique global minimum. If it is temporarily assumed that the filter coefficients do not vary with time, the gradient of the cost function can be written

$$\frac{\partial e^2(n)}{\partial \boldsymbol{w}} = 2\boldsymbol{x}(n)e(n). \tag{2.5}$$

Now if the coefficients are able to vary, the update equation for the vector of coefficients according to the method of steepest descent is given by

$$\boldsymbol{w}(n+1) = \boldsymbol{w}(n) - \mu \boldsymbol{x}(n) e(n), \tag{2.6}$$

where μ is the learning rate and controls the rate of convergence. It can be shown that the LMS algorithm converges to the minimum value of the cost function if

$$0 < \mu < \frac{1}{\lambda_{max}}, \tag{2.7}$$

where λ_{max} is the largest eigenvalue of the autocorrelation matrix of the reference signal $x(n)$ [22].

2.2 Adaptive IIR filtering

Adaptive IIR filtering is significantly more complicated than adaptive FIR filtering due to stability issues associated with IIR filters. Adaptive IIR filters are based on either the output-error approach or the equation-error approach. The equation-error approach is advantageous in system identification applications because the cost function represented by the mean squared error is unimodal. However, this approach assumes that the desired response of the system is known *a priori*, which is not the case in an adaptive control system. For this reason, the only method that will be included here is the output-error approach [2].

The structure of a generic adaptive IIR filtering problem is shown in Figure 2.2. The input signal $x(n)$ drives the numerator of the IIR to produce an output, which is then fed back to drive the denominator $A(z)$ and generate the output $y(n)$. This can be written as the summation

$$y(n) = \sum_{i=0}^{I-1} b_i x(n-i) + \sum_{j=1}^{J} a_j y(n-j), \tag{2.8}$$

or in vector form as

$$y(n) = \boldsymbol{b}^T \boldsymbol{x}(n) + \boldsymbol{a}^T \boldsymbol{y}(n-1), \tag{2.9}$$

where $\boldsymbol{x}(n)$ and $\boldsymbol{y}(n)$ are vectors containing past samples of the input and output signals. A parameter vector can be formed by combining the feedforward and feedback coefficients in a vector

$$\boldsymbol{w} = \begin{bmatrix} b_0 & b_1 & \cdots & b_{I-1} & a_1 & a_2 & \cdots & a_J \end{bmatrix}, \tag{2.10}$$

along with an information vector

$$\boldsymbol{h}(n) = \begin{bmatrix} x(n) & x(n-1) & \cdots & x(n-I+1) & y(n-1) & y(n-1) & \cdots & y(n-J) \end{bmatrix}, \tag{2.11}$$

such that the filter output can be written

$$y(n) = \boldsymbol{w}^T \boldsymbol{h}(n). \tag{2.12}$$

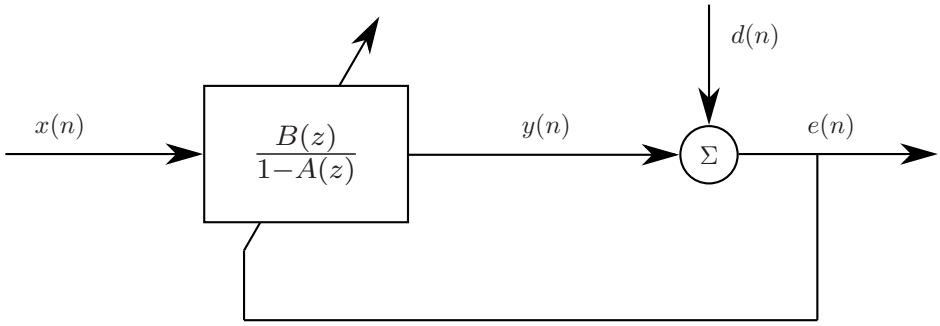

Figure 2.2: Structure of an adaptive IIR filter.

It is clear that there is inherent feedback in an IIR filter, with the current filter output being a function of past outputs. Similar to the adaptive FIR filtering problem, the objective is to adjust the coefficients b_i and a_j such that the output $y(n)$ most closely matches the desired response $d(n)$. Unfortunately, the cost function formed by the mean square error is in general not a convex function of the coefficients and may contain multiple local minima, which makes standard adaptation schemes such as steepest descent unreliable.

Numerous methods for adapting the coefficients b_i and a_j have been proposed, but proving convergence and stability of the algorithms is significantly more difficult than for adaptive FIR filtering algorithms. A derivation of the recursive prediction error algorithm [84] is included in the next section, as this is the same approached used in Chapter 3 to develop an adaptive algorithm for updating the coefficient in single and multichannel hybrid controllers.

2.2.1 Recursive prediction error algorithm

The recursive prediction error algorithm [85] is similar to LMS in the sense that it is based on adjusting the filter coefficients according to an estimate of the gradient of a suitably defined cost function. Again considering Figure 2.2, the error signal is given by

$$e(n) = d(n) - y(n). \tag{2.13}$$

If the cost function is the instantaneous squared error, the gradient can be expressed [85]

$$\frac{\partial e^2(n)}{\partial \boldsymbol{w}(n)} = -2e(n)\frac{\partial y(n)}{\partial \boldsymbol{w}(n)}. \tag{2.14}$$

In contrast to the LMS algorithm, the filter coefficients here are not assumed to be time-invariant. The problem has thus been reduced to calculating the partial derivatives of the IIR filter output $y(n)$ with respect to each of the coefficients. An expression for a vector of these partial derivatives can be formed by computing the partial derivatives with respect to an individual feedfor-

ward and feedback coefficient such that

$$\frac{\partial y(n)}{\partial b_k(n)} = x(n-k) + \sum_{j=1}^{J} a_j \frac{\partial y(n-j)}{\partial b_k(n)}, \tag{2.15}$$

$$\frac{\partial y(n)}{\partial a_k(n)} = y(n-k) + \sum_{j=1}^{J} a_j \frac{\partial y(n-j)}{\partial a_k(n)}. \tag{2.16}$$

The second terms in Equations 2.15-2.16 arise because of the inherent feedback in the filter. This can be understood by computing the partial derivative of Equation 2.8 with respect to any individual filter coefficient. The past values of the filter output $y(n-j)$ are functions of the current coefficient values due to the recursive nature of the update equation, and hence must be included in the partial derivative. The partial derivatives in Equations 2.15-2.16 cannot be explicitly evaluated because both sides of the equation contain partial derivatives with respect to current values of the coefficients. If it is assumed that the coefficients are adapting slowly [85], *i.e.*, $\boldsymbol{w}(n) \approx \boldsymbol{w}(n-1) \approx \cdots \approx \boldsymbol{w}(n-J)$, Equations 2.15-2.16 can be rewritten as

$$\frac{\partial y(n)}{\partial b_k(n)} = x(n-k) + \sum_{j=1}^{J} a_j \frac{\partial y(n-j)}{\partial b_k(n-j)}, \tag{2.17}$$

$$\frac{\partial y(n)}{\partial a_k(n)} = y(n-k) + \sum_{j=1}^{J} a_j \frac{\partial y(n-j)}{\partial a_k(n-j)}, \tag{2.18}$$

which are now recursive in the partial derivatives. Equations 2.17-2.18 can be written in terms of a recursive filter such that

$$\frac{\partial y(n)}{\partial b_k(n)} = \left(\frac{1}{1-A(z)}\right) x(n-k), \tag{2.19}$$

$$\frac{\partial y(n)}{\partial a_k(n)} = \left(\frac{1}{1-A(z)}\right) y(n-k), \tag{2.20}$$

where

$$A(z) = a_1 z^{-1} + a_2 z^{-2} + \cdots + a_J z^{-J}. \tag{2.21}$$

Here, z^{-1} is the unit delay operator such that $z^{-1}x(n) = x(n-1)$. With expressions for the partial derivatives, the update equation used in the recursive prediction error algorithm is

$$\boldsymbol{w}(n+1) = \boldsymbol{w}(n) - \boldsymbol{R}^{-1}\left(\frac{1}{1-A(z)}\right)\boldsymbol{h}(n)e(n). \tag{2.22}$$

The matrix $\boldsymbol{R}$ is the autocorrelation matrix of the reference signal. Multiplying the gradient estimate by the inverse of this matrix normalizes the performance surface and improves the rate of convergence. Similar approaches are taken in some active control algorithms such as recursive least squares (RLS) [86].

2.3 Broadband feedforward ANC

In this section, a brief review of broadband feedforward ANC is included. This has relevance to the experimental results that will be presented in Chapter 5. The single channel filtered-reference LMS and the multichannel multiple error LMS algorithms will be derived in the following sections.

2.3.1 Filtered-reference LMS algorithm

The filtered reference least mean squares (FxLMS) algorithm is based on the well-known least mean squares (LMS) algorithm for adaptive filtering. This brief description of the algorithm is based on the filtered reference signal approach and follows a discussion in [2].

Consider the block diagram of Figure 2.3. The control signal $u(n)$ is generated by filtering the reference signal $x(n)$ by the adaptive controller $W(z)$, which is parameterized as a finite impulse response (FIR) filter, to give

$$u(n) = \sum_{i=0}^{I-1} w_i x(n-i). \tag{2.23}$$

The error signal can be written as the summation of the primary disturbance and the control signal after being filtered by the plant response to give

$$e(n) = d(n) + \sum_{j=1}^{J} \sum_{i=0}^{I-1} g_j w_i x(n-i-j). \tag{2.24}$$

If it is then assumed that the control filter is adapting slowly compared with the timescales of the plant dynamics, the filtering by $W(z)$ and $G(z)$ can be commuted such that the error signal can be rewritten

$$e(n) = d(n) + \sum_{i=0}^{I-1} w_i r(n-i). \tag{2.25}$$

where the filtered reference signal has been defined as

$$r(n) = \sum_{j=1}^{J} g_j x(n-j). \tag{2.26}$$

The error signal can be written in vector form as

$$e(n) = d(n) + \boldsymbol{w}^T(n)\boldsymbol{r}(n). \tag{2.27}$$

where

$$\boldsymbol{r}(n) = \begin{bmatrix} r(n) & r(n-1) & \cdots & r(n-I+1) \end{bmatrix}^T, \tag{2.28}$$

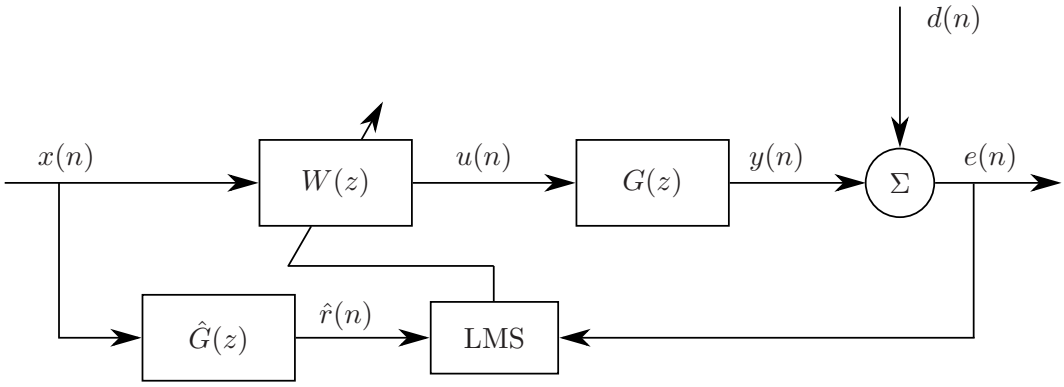

Figure 2.3: Block diagram of a single channel feedforward adaptive control system.

and

$$\boldsymbol{w}(n) = \begin{bmatrix} w_0 & w_1 & \cdots & w_{I-1} \end{bmatrix}^T. \tag{2.29}$$

The coefficients w_i are adapted to minimize the instantaneous mean squared error given by

$$J = e^2(n). \tag{2.30}$$

If it is assumed that the filter coefficients are time-invariant (*i.e.*, slow adaptation), the gradient with respect to an individual coefficient is

$$\frac{\partial e^2(n)}{\partial w_i} = 2e(n)\frac{\partial e(n)}{\partial w_i} = 2e(n)r(n-i). \tag{2.31}$$

The gradient in vector form is thus simply

$$\frac{\partial e^2(n)}{\partial \boldsymbol{w}} = 2e(n)\boldsymbol{r}(n). \tag{2.32}$$

The update law based on the method of steepest descent is then

$$\boldsymbol{w}(n+1) = \boldsymbol{w}(n) - \mu \boldsymbol{r}(n)e(n), \tag{2.33}$$

where μ is the learning rate and controls the rate of convergence. The weight vector will converge to the true minimum given by the Wiener solution,

$$\boldsymbol{w}_{opt} = -E\left[\boldsymbol{r}(n)\boldsymbol{r}^T(n)\right]^{-1} E\left[\boldsymbol{r}(n)d(n)\right], \tag{2.34}$$

provided a perfect model of the plant is available. If instead an estimate of the plant is used, which is always the case in practice, the weight vector will converge to

$$\boldsymbol{w} = -E\left[\hat{\boldsymbol{r}}(n)\boldsymbol{r}^T(n)\right]^{-1} E\left[\hat{\boldsymbol{r}}(n)d(n)\right], \tag{2.35}$$

where $\hat{\boldsymbol{r}}(n)$ implies that the reference signal is filtered by an *estimate* of the plant response. The algorithm will converge provided that the phase of the plant response estimate is within 90° of that of the true plant at the frequency of interest. It can be shown that the maximum step size is dependent upon the spectral characteristics of the input signal and the dynamics associated with the plant response.

In practice it is common to include an effort weighting term in the cost function such that

$$J = e^2(n) + \beta \boldsymbol{w}^T(n)\boldsymbol{w}(n). \tag{2.36}$$

In this case, the update equation becomes

$$\boldsymbol{w}(n+1) = (1-\mu\beta)\boldsymbol{w}(n) - \mu \boldsymbol{r}(n)e(n), \tag{2.37}$$

where β is an effort waiting parameter that puts constraints on the magnitude of the filter coefficients. This approach is referred to as the leaky FxLMS [2] and has been shown to greatly increase the robustness of the algorithm, although it does degrade the steady state performance.

2.3.2 Multiple error LMS algorithm

The multiple error LMS algorithm, proposed by Elliott and Nelson [26], is an extension of the filtered-reference LMS algorithm that accounts for multiple reference signals, control actuators, and error sensors. The derivation of the algorithm, which is based on the method of steepest descent, is similar to that of FxLMS. A brief derivation of the algorithm is presented in this section and follows a discussion in [2].

Consider the block diagram in Figure 2.4. It will be assumed that the control system consists of K reference signals, M control actuators, and L error sensors. The M control signals are generated by filtering K reference signals by an $MK \times MK$ matrix of control filters, each of which is modeled as an FIR filter with I coefficients. Here, $\boldsymbol{x}(n)$ is a $K \times 1$ vector, $\boldsymbol{u}(n)$ is an $M \times 1$ vector, and $\boldsymbol{y}(n)$, $\boldsymbol{d}(n)$, and $\boldsymbol{e}(n)$ are all $L \times 1$ vectors.

An expression for the error signal can be derived by first noting that the m-th control signal is given by

$$u_m(n) = \sum_{k=1}^{K} \sum_{i=0}^{I-1} w_{mki} x_k(n-i), \tag{2.38}$$

where w_{mki} is the i-th coefficient of the control filter driving the m-th control source by the k-th reference signal $x_k(n)$. The l-th error signal is the summation of the l-th disturbance signal and each control signal filtered by the corresponding plant response such that

$$e_l(n) = d_l(n) + \sum_{m=1}^{M} \sum_{j=1}^{J} \sum_{k=1}^{K} \sum_{i=0}^{I-1} g_{lmj} w_{mki} x_k(n-i-j), \tag{2.39}$$

where g_{lmj} is the j-th coefficient of an FIR filter representing the transfer path from the m-th actuator to the l-th sensor. It is again temporarily assumed that the control filter coefficients

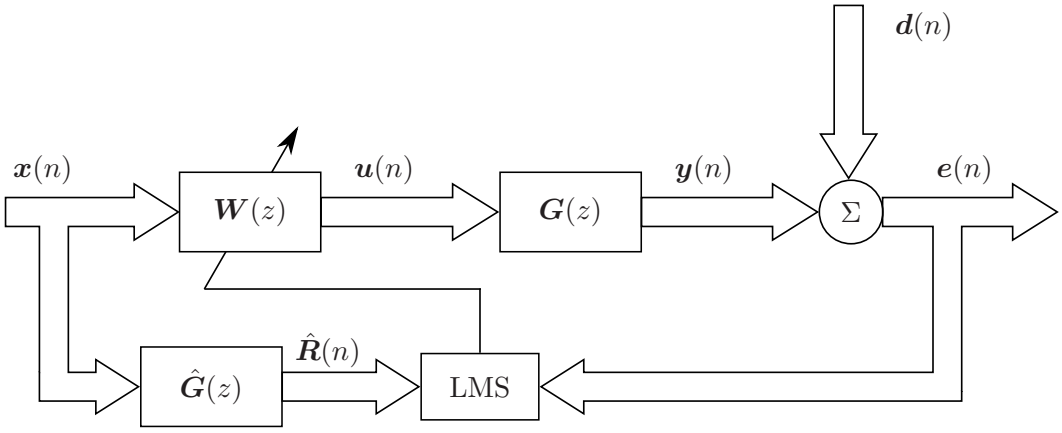

Figure 2.4: Block diagram of a multichannel feedforward adaptive control system.

are time-invariant so that the filtering by the plant and the controller can be commuted such that

$$e_l(n) = d_l(n) + \sum_{m=1}^{M} \sum_{k=1}^{K} \sum_{i=0}^{I-1} w_{mki} r_{lmk}(n-i), \tag{2.40}$$

where the filtered reference signals have been defined as

$$r_{lmk}(n) = \sum_{j=1}^{J} g_{lmj} x_k(n-j). \tag{2.41}$$

This signal is the k-th reference signal after being filtered by the plant response from the m-th actuator to the l-th error sensor. The error signal can be written in vector form as

$$\boldsymbol{e}(n) = \boldsymbol{d}(n) + \boldsymbol{R}(n)\boldsymbol{w}(n), \tag{2.42}$$

where $\boldsymbol{R}(n)$ is a matrix of filtered reference signals defined as

$$\boldsymbol{R}(n) = \begin{bmatrix} \boldsymbol{r}_1(n) & \boldsymbol{r}_1(n-1) & \cdots & \boldsymbol{r}_1(n-I+1) \\ \boldsymbol{r}_2(n) & \ddots & & \\ \vdots & & & \\ \boldsymbol{r}_l(n) & \cdots & & \boldsymbol{r}_l(n-I+1) \end{bmatrix}, \tag{2.43}$$

and

$$\boldsymbol{r}_l(n) = \begin{bmatrix} r_{l11}(n) & r_{l12}(n) & \cdots & r_{l1k}(n) & r_{l21}(n) & \cdots & r_{lmk}(n) \end{bmatrix}. \tag{2.44}$$

The vectors $\boldsymbol{e}(n)$, $\boldsymbol{d}(n)$, and $\boldsymbol{w}(n)$ contain the error signals, disturbance signals, and the filter coefficients. The cost function to be minimized is the sum of the mean squared error signals

$$J = \boldsymbol{e}^T(n)\boldsymbol{e}(n) \tag{2.45}$$

The vector of filter coefficients is adapted in the negative direction of the gradient of the cost function, which is given by

$$\frac{\partial \boldsymbol{e}^T(n)\boldsymbol{e}(n)}{\partial \boldsymbol{w}(n)} = 2\boldsymbol{R}^T(n)\boldsymbol{e}(n). \tag{2.46}$$

The update equation for the multiple error LMS algorithm is thus

$$\boldsymbol{w}(n+1) = \boldsymbol{w}(n) - \mu \boldsymbol{R}^T(n)\boldsymbol{e}(n), \tag{2.47}$$

where μ is the learning rate of the algorithm and controls the rate of convergence. In practice an estimate of the plant is used and the update equation is

$$\boldsymbol{w}(n+1) = \boldsymbol{w}(n) - \mu \hat{\boldsymbol{R}}^T(n)\boldsymbol{e}(n), \tag{2.48}$$

where $\hat{\boldsymbol{R}}^T(n)$ implies that the reference signals have been filtered by an estimate of the plant response. It can be shown that the weight vector will converge to

$$\boldsymbol{w} = -E\left[\hat{\boldsymbol{R}}(n)\boldsymbol{R}^T(n)\right]^{-1} E\left[\hat{\boldsymbol{R}}(n)d(n)\right], \tag{2.49}$$

provided the matrix of plant responses $\boldsymbol{R}(n)$ and its estimate $\hat{\boldsymbol{R}}(n)$ satisfy a strictly positive real condition [87].

Similar to FxLMS, it is common to include an effort weighting term in the cost function such that the cost function is defined

$$J = \boldsymbol{e}^T(n)\boldsymbol{e}(n) + \beta \boldsymbol{w}^T(n)\boldsymbol{w}(n). \tag{2.50}$$

In this case, the update equation becomes

$$\boldsymbol{w}(n+1) = (1-\mu\beta)\boldsymbol{w}(n) - \mu \hat{\boldsymbol{R}}^T(n)\boldsymbol{e}(n), \tag{2.51}$$

where β is an effort weighting parameter that puts constraints on the magnitude of the filter coefficients. Equation 2.51 is referred to as the leaky FxLMS algorithm [18].

2.4 Narrowband feedforward ANC

This section presents information relevant to multichannel control of tonal disturbances. Although the algorithms described in the previous section can certainly be used to attenuate tonal disturbances, they may suffer from prohibitively slow convergence speeds. This section emphasizes the H_2 optimal control solutions for underdetermined, fully determined, and overdetermined systems. This section provides a basis for the calculation of the optimal control laws used in the finite element models considered in Chapter 4. A more in depth discussion of this material can also be found in [88].

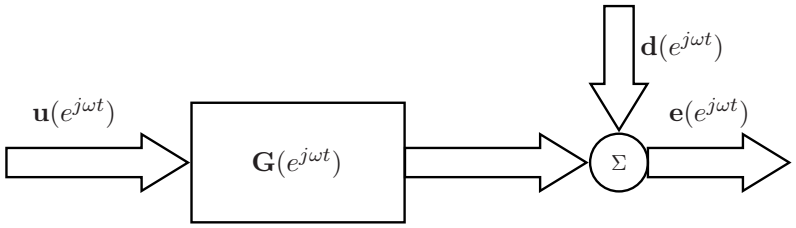

Figure 2.5: Block diagram of a single frequency multichannel feedforward control system.

2.4.1 Problem formulation

Consider the block diagram in Figure 2.5. It will be assumed that the disturbance is a sinusoid with arbitrary amplitude, phase, and frequency. It is further assumed that there is a signal available that is perfectly correlated with the disturbance. The system is composed of L error sensors and M control actuators. In a tonal control system, the signals can be represented as complex numbers with a specific amplitude and phase. The $L \times 1$ vector of primary responses is denoted $\mathbf{d}(e^{j\omega t})$, the $M \times 1$ vector of actuator outputs is denoted $\mathbf{u}(e^{j\omega t})$, and the response of the plant at a single frequency is characterized by an $L \times M$ transfer function matrix denoted $\mathbf{G}(e^{j\omega t})$. The vector of error sensor responses can thus be written

$$\mathbf{e}(e^{j\omega t}) = \mathbf{d}(e^{j\omega t}) + \mathbf{G}(e^{j\omega t})\mathbf{u}(e^{j\omega t}). \tag{2.52}$$

The cost function considered here is the sum of the mean squared error signals. This can be written as the inner product of the complex error vector responses such that

$$J = \mathbf{e}^H \mathbf{e}, \tag{2.53}$$

where the dependence on $e^{j\omega t}$ has been dropped for convenience. Expanding this gives

$$J = (\mathbf{d} + \mathbf{G}\mathbf{u})^H (\mathbf{d} + \mathbf{G}\mathbf{u}) \tag{2.54}$$

$$= \mathbf{u}^H \left(\mathbf{G}^H \mathbf{G}\right) \mathbf{u} + \mathbf{u}^H \mathbf{G}^H \mathbf{d} + \mathbf{d}^H \mathbf{G}\mathbf{u} + \mathbf{d}^H \mathbf{d}, \tag{2.55}$$

which is quadratic in the control inputs. The existence and uniqueness of a minimum value of the cost function will be dictated by the structure of the Hessian matrix $\mathbf{G}^H\mathbf{G}$. The structure of the Hessian matrix will be determined by the number of sensors and actuators and their relative positioning. The next section presents the optimal control inputs for overdetermined, fully-determined, and underdetermined systems.

2.4.2 Optimal control

This section gives a brief summary of H_2-optimal control strategies for overdetermined, fully-determined, and underdetermined systems. The optimal control inputs for these three classes of systems will be used again in Chapter 4 when discussing the spatial extent of quiet zones resulting from implementation of each control strategy.

Overdetermined systems

In an overdetermined system, there are more error sensors than control actuators ($L > M$). This is a common case encountered in practical applications such as the reduction of interior aircraft noise [89], the reduction of sound in an enclosure [7], the reduction of sound radiated from structures [90], and numerous others. In this case $\mathbf{G}^H\mathbf{G}$ will be positive definite as long as multiple actuators or sensors are not located at the same point in space [2]. If this is the case, rows or columns (depending if actuators or sensors are colocated) become linearly dependent, which results in the Hessian matrix being singular, a problem referred to in the literature as collinearity [33]. To compute the optimal control law, the cost function is differentiated with respect to the real and imaginary parts of $\mathbf{u}$ and equated to zero. The details of this derivation will be omitted, but can be found in any standard reference such as [2, 88]. The control input that minimizes the mean squared error is given by

$$\mathbf{u}_{opt} = -\left[\mathbf{G}^H\mathbf{G}\right]^{-1}\mathbf{G}^H\mathbf{d}. \tag{2.56}$$

The minimum value of the cost function is obtained by substituting the optimal set of control inputs back into the cost function to obtain

$$J_{min} = \mathbf{d}^H\left[\mathbf{I} - \mathbf{G}\left[\mathbf{G}^H\mathbf{G}\right]^{-1}\mathbf{G}^H\right]\mathbf{d}. \tag{2.57}$$

A brief discussion regarding the conditioning of overdetermined systems should be included, as this topic arises in Chapter 4. The control input given by Equation 2.56 is guaranteed to minimize the mean squared error provided the matrix $\mathbf{G}^H\mathbf{G}$ is not singular. However, computation of the inverse becomes numerically sensitive to small changes in the elements of $\mathbf{G}$ if the Hessian matrix is close to being singular, *i.e.*, has a large condition number. This will be the case if actuators or sensors are located close to one another, which is an issue that will be discussed in further detail in Chapter 4. One convenient method for improving the conditioning of the control system in this case is to add a regularization term to the Hessian matrix. This is equivalent to adding a term proportional to the control effort into the cost function. The resulting control input is then

$$\mathbf{u}_{opt} = -\left[\mathbf{G}^H\mathbf{G} + \beta\mathbf{I}\right]^{-1}\mathbf{G}^H\mathbf{d}, \tag{2.58}$$

where β is a regularization term and should not be confused with the leakage factor used in previous sections. This approach serves to shift the eigenvalues of $\mathbf{G}^H\mathbf{G}$ by a value of β, hence making calculation of the inverse more numerically stable.

Fully determined systems

When there are as many actuators as sensors ($L = M$), the system is referred to as fully determined. In this case the matrix $\mathbf{G}^H\mathbf{G}$ is square and the inverse can be computed straightforwardly, provided it is not singular. Again, this will be the case as long as multiple actuators or

sensors are not collocated [2, 33]. Since there are as many control actuators as sensors, it is possible to set the error to zero at every error sensor. In this case, the optimal control inputs are particularly simple to calculate. With the vector of error signals is given by

$$\mathbf{e} = \mathbf{d} + \mathbf{G}\mathbf{u}, \tag{2.59}$$

the control input that sets the error to zero is easily found as

$$\mathbf{u}_{opt} = -\mathbf{G}^{-1}\mathbf{d}. \tag{2.60}$$

It is an intuitive result that with as many control actuators as error sensors it is possible to drive each of the error signals to zero. Although it has been noted that this is an uncommon situation in practice, it is somewhat common in the context of active headrests. For instance, several authors have explored active headrests with two loudspeakers and two sensors [49] as well as using seperate single channel systems for each ear [47].

Underdetermined systems

If there are more actuators than sensors ($M > L$), the system is referred to as underdetermined. In this case the matrix $\mathbf{G}^H\mathbf{G}$ is singular. Rather than a single optimal control input, there are now an infinite number of possible control inputs that will set the error to zero. A common approach to solving the minimization problem is to minimize the control effort while constraining the cost function be equal to zero. Again the derivation will be omitted, but can be found in [91]. The resulting optimal control is

$$\mathbf{u}_{opt} = -\mathbf{G}^H\left[\mathbf{G}\mathbf{G}^H\right]^{-1}\mathbf{d}. \tag{2.61}$$

Note that the same regularization approach that was discussed in the context of overdetermined systems can be used here as well, resulting in the control input given by Equation 2.58. Note that this is only valid for $\beta > 0$.

2.5 Feedback control

Feedback control systems do not make use of any time advanced reference signal, and compute the control inputs based solely on the error signals. While feedforward controllers have almost always been implemented digitally, analog feedback controllers have commonly been used in ANC, for the most part in headsets [92, 93]. Nonetheless, all control strategies considered in this dissertation are implemented digitally, therefore only background material relating to digital feedback control will be covered in this section.

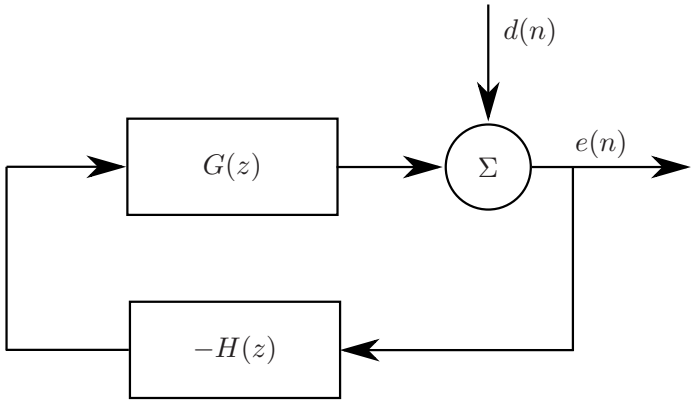

Figure 2.6: Block diagram of a standard single channel negative feedback control system.

2.5.1 Disturbance rejection

A block diagram of a standard negative feedback control system, designed for disturbance rejection, is shown in Figure 2.6. The objective is to design the control filter $H(z)$ such that maximum disturbance rejection is achieved over the entire frequency bandwidth of interest.

The closed loop transfer function from the error signal to the disturbance signal is given by

$$S(z) = \frac{E(z)}{D(z)} = \frac{1}{1 + G(z)H(z)}. \tag{2.62}$$

This function is referred to as the sensitivity function and is used to measure the degree of disturbance rejection [94]. For good disturbance rejection, the sensitivity function should be as small as possible, *i.e.*,

$$1 + G(z)H(z) \gg 1. \tag{2.63}$$

Although Equation 2.63 may suggest a straightforward approach to feedback control design, care must be taken to ensure that the loop gain $G(z)H(z)$ does not exceed unity at phase lags of 180°. This leads to the concept of stability. The stability of a feedback system is determined by the location of the poles of Equation 2.62, that is, the roots of

$$1 + G(z)H(z) = 0, \tag{2.64}$$

which is referred to as the *characteristic equation* of the system. To guarantee stability of the closed loop system, the roots of Equation 2.64 must all lie inside the unit circle in the z-plane. If the controller is fixed, the roots can be explicitly computed and the stability inferred. When the controller is made adaptive, the closed loop transfer function is constantly changing, and it is possible that the filter coefficients will be adapted into a region corresponding to an unstable feedback loop [95].

The concept of robust stability should also be mentioned here. In most active noise control problems, the plant is subject to uncertainties and/or modeling errors. For a control system to

be considered robust, it must remain stable despite varying plant dynamics. Note that system robustness is a fundamentally different concept than system performance. In general, a control system should operate at some predefined minimum level of performance for all expected plant conditions. Modern H_∞ methods have aimed to design controllers with this concept in mind [96].

Although many methods of designing robust control systems have been proposed [97, 98], the most common approach in ANC is based on the concept of multiplicative uncertainty. In this approach, it is assumed that the plant frequency response can be described by

$$G(j\omega) = G_0(j\omega)\left(1 + \Delta(j\omega)\right), \tag{2.65}$$

where $G_0(j\omega)$ is the nominal plant response and $\Delta(j\omega)$ is a frequency dependent bound on the plant uncertainty. Graphically, the complex plant response at a certain frequency can be thought of as lying anywhere in the complex plane within a disk of radius $G_0(j\omega)|\Delta(j\omega)|$ whose center coincides with the nominal plant response. Using results from Nyquist stability theory [99], it can be shown that the feedback system will be robustly stable provided

$$|T_0(j\omega)| < \frac{1}{B(j\omega)}, \tag{2.66}$$

where $B(j\omega)$ is a bound on the magnitude of the uncertainty

$$|\Delta(j\omega)| \leq B(j\omega), \tag{2.67}$$

and $T_0(j\omega)$ is the complimentary sensitivity function given by

$$T(j\omega) = \frac{G_0(j\omega)H(j\omega)}{1 + G_0(j\omega)H(j\omega)}. \tag{2.68}$$

Since the uncertainties in most acoustic plants are unstructured in nature, this approach provides a useful tool for designing robust active control systems. As mentioned before, guaranteeing the stability of adaptive systems is considerably more difficult due to the constantly changing closed loop transfer function. The most common approach to robust adaptive feedback control is thus to penalize the control effort such that the feedback controller does not stray into a region corresponding to an unstable feedback loop. Another method of designing feedback controllers, known as internal model control, will be discussed in the next section.

2.5.2 Internal model control

The internal model principle [52] provides a convenient way of expressing a feedback controller in a feedforward setting. This approach allows feedforward control techniques, which have been widely studied in the context of active noise control, to be used effectively in a feedback system. A feedback system employing internal model control uses an internal model of the plant to synthesize a reference signal that is then used to drive the control filter.

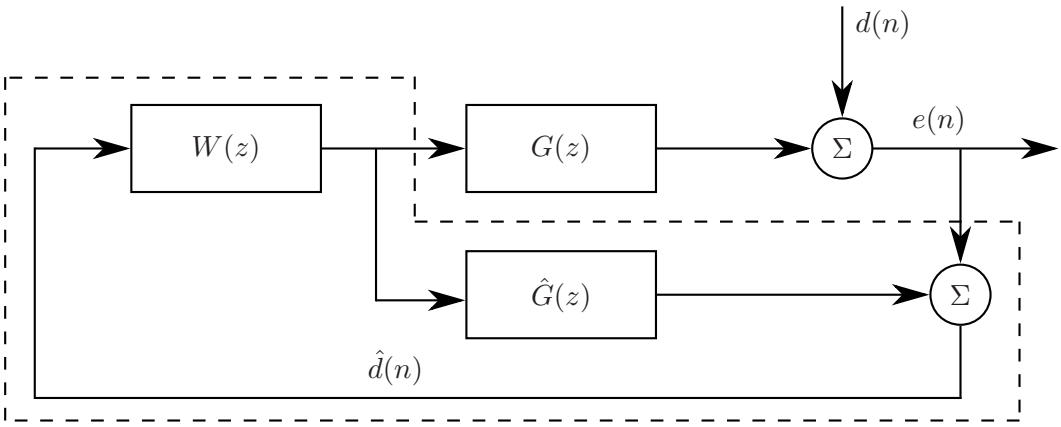

Figure 2.7: Block diagram of the internal model structure. The controller $H(z)$ is contained within the dashed lines.

A block diagram of a single channel feedback system employing internal model control is shown in Figure 2.7. The controller, shown inside the dashed box, is comprised of an internal model of the plant $\hat{G}(z)$ and a control filter $W(z)$. An estimate of the contribution of the control input is subtracted from the error signal such that the signal driving the control filter $\hat{d}(n)$ is an estimate of the disturbance signal.

The transfer function of the internal model feedback controller is given by

$$H(z) = -\frac{W(z)}{1+\hat{G}(z)W(z)}. \tag{2.69}$$

The sensitivity function, which recall is a measure of disturbance rejection, is then

$$S(z) = \frac{1+\hat{G}(z)W(z)}{1-\left[G(z)-\hat{G}(z)\right]W(z)}, \tag{2.70}$$

so that the stability of the closed loop system depends on the roots of

$$1-\left[G(z)-\hat{G}(z)\right]W(z) = 0. \tag{2.71}$$

It is clear that if a perfect plant model is used, the system will be closed loop stable. In this case, the block diagram is reduced to that shown in Figure 2.8. Here, the contribution of the control signal is completely removed from the error signal and the disturbance acts simultaneously as the reference signal. In this case the system is entirely feedforward, with the only major difference being that the reference signal no longer provides time-advanced information on the disturbance. Because the signal driving the control filter no longer provides any time-advanced information, the bandwidth over which attenuation can be expected is more heavily influenced by plant delays than a feedforward system [100].

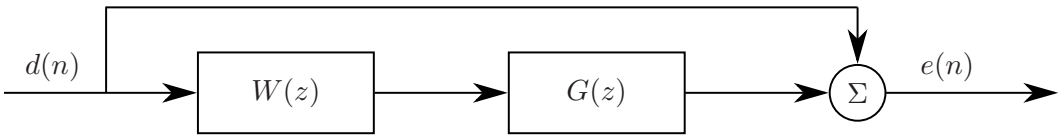

Figure 2.8: Block diagram of the control system with a perfect plant model, *i.e.*, $G(z) = \hat{G}(z)$.

2.5.3 Filtered-reference LMS

The internal model configuration provides a convenient framework for implementing adaptive filtering-based control systems in a feedback architecture. The most common algorithm for adapting the control filter is the leaky filtered-reference LMS algorithm, which recall has an update law described by

$$\boldsymbol{w}(n+1) = (1-\mu\beta)\boldsymbol{w}(n) - \mu\hat{\boldsymbol{r}}(n)e(n). \tag{2.72}$$

Now the vector of filtered reference signals $\hat{\boldsymbol{r}}(n)$ has been formed by filtering the disturbance estimate $\hat{d}(n)$ by the plant model. Although an accurate plant model will reduce the risk of feedback instabilities, any degree of modeling error may result in an unstable system. Even if the modeling error is small at a certain frequency, a large magnitude in the frequency response of $W(z)$ may destabilize the controller. The degree of modeling error necessary to destabilize a system is difficult to quantify analytically. Rafaely [95] investigated this concept using an active headset and showed that the performance surface becomes non-quadratic for certain combinations of modeling errors. Vaudrey [101] showed that the relationship between adaptive algorithm divergence and feedback loop instabilities are highly interrelated and system dependent. For these reasons, it is almost always necessary to use a leak on the control filter coefficients when implementing FxLMS in a feedback system.

Another major limitation of using the FxLMS algorithm, as well as other similar adaptive algorithms, in a feedback setting is that the reference signal no longer provides time-advanced information on the disturbance. Therefore, the delays associated with the plant dynamics play a much more critical role in feedback control than they did for feedforward systems [100]. For this reason, most adaptive feedback systems are best suited for the control of narrowband disturbances, although some degree of broadband attenuation can be attained if the plant delays are small. This would generally involve using a very high sampling rate and having the error sensor located very close to the control source, which can be unfavorable from an acoustics standpoint in certain cases.

Chapter 3

Multichannel Hybrid Active Noise Control

3.1 Single Channel Formulation

This section contains a derivation of what will be referred to as the full gradient algorithm for a single channel adaptive hybrid controller. The single channel formulation will help set the stage for the multichannel case in Section 2. To begin, the gradient is computed with respect to individual feedforward and feedback filter coefficients. A vector notation similar to that in [2] is then presented to compactly express the algorithm. Although this chapter is primarily concerned with the adaptation mechanisms in hybrid controllers, some simulations and experiments of steady state performance in a single channel hybrid controller can be found in Appendix C.

The derivation of the full gradient algorithm is a novel contribution and provides insight into the effects that plant modeling error have on the adaptation mechanisms in hybrid control systems. The resulting algorithm is similar to the filtered reference LMS algorithm discussed in the previous chapter, although the approach taken to the derivation is different and makes no assumptions regarding plant model accuracy. By treating the hybrid control system as a single infinite impulse response (IIR) filter, where the feedforward and feedback control filters act as the numerator and denominator of the IIR, the exact update equation based on the method of steepest descent will be derived for each filter coefficient.

3.1.1 Full gradient algorithm

Consider the block diagram of Figure 3.1. This represents a standard hybrid control architecture. The plant and plant model are assumed linear time-invariant and denoted $G(z)$ and $\hat{G}(z)$, respectively. The feedforward control filter $B(z)$ is driven by the reference signal $x(n)$. The feedback controller uses an internal model of the plant to generate a reference signal $\hat{d}(n)$ that drives the feedback control filter $A(z)$ [52]. Each control filter is adapted to minimize the error signal

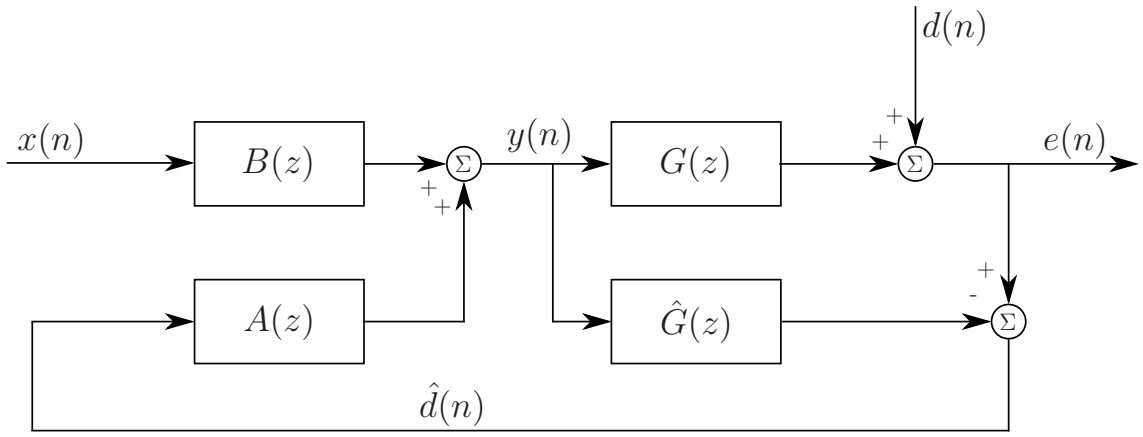

Figure 3.1: Block diagram of a single channel hybrid active noise control system.

$e(n)$. If $A(z)$ and $B(z)$ are parameterized as (FIR) filters with I_a and I_b coefficients, respectively, the system can be viewed as a single adaptive IIR filter with the feedforward part being driven by the reference signal and the feedback part being driven by the estimated disturbance signal. The error signal can be expressed as

$$e(n) = d(n) + \sum_{j=0}^{J-1} g_j y(n-j), \tag{3.1}$$

where g_j is the j-th coefficient of the FIR representing the plant and the control signal is

$$y(n) = \sum_{i=0}^{I_b-1} b_i(n) x(n-i) + \sum_{i=1}^{I_a} a_i(n) \hat{d}(n-i). \tag{3.2}$$

Here, $a_i(n)$ and $b_i(n)$ are the coefficients of the feedback and feedforward filters, respectively. The feedback term is summed from $i = 1$ to represent the inherent delay in estimating the disturbance signal. This can be written as the inner product

$$y(n) = \boldsymbol{h}^T(n)\boldsymbol{w}(n), \tag{3.3}$$

where the vector of reference signals is defined as

$$\boldsymbol{h}(n) = \begin{bmatrix} x(n) & \cdots & x(n-I_b+1) & \hat{d}(n-1) & \cdots & \hat{d}(n-I_a) \end{bmatrix}^T, \tag{3.4}$$

and the vector of adjustable filter coefficients is

$$\boldsymbol{w}(n) = \begin{bmatrix} b_0(n) & \cdots & b_{I_b-1}(n) & a_1(n) & \cdots & a_{I_a}(n) \end{bmatrix}^T. \tag{3.5}$$

The following adaptive algorithm is based on Widrow's LMS algorithm [22] and employs the method of steepest descent. The idea is to adapt the control filter coefficients in the negative

direction of the local gradient of the cost function. The general form of the update equation takes the form

$$\boldsymbol{w}(n+1) = \boldsymbol{w}(n) + \alpha\left(-\boldsymbol{\nabla}_{\boldsymbol{w}(n)} J\right), \tag{3.6}$$

where α is the learning rate, J is the cost function, and $\boldsymbol{\nabla}_{\boldsymbol{w}(n)}$ denotes the partial derivative with respect to the current values of each filter coefficient. The cost function is the mean square error (MSE)

$$J = \frac{1}{2} E\left[e^2(n)\right]. \tag{3.7}$$

Because the above cost function requires the expected value of the MSE, it cannot be evaluated for online adaptation. As an approximation, it is replaced by a stochastic estimate $J(n) = \frac{1}{2}e^2(n)$. Observing that the error signal can be written as $e(n) = d(n) + G(z)y(n)$, the gradient is evaluated as

$$\begin{aligned} \boldsymbol{\nabla}_{\boldsymbol{w}(n)} J(n) &= e(n)\boldsymbol{\nabla}_{\boldsymbol{w}(n)}\left[G(z)y(n)\right] \\ &= e(n)G(z)\boldsymbol{\nabla}_{\boldsymbol{w}(n)}\left[y(n)\right]. \end{aligned} \tag{3.8}$$

The filtering by $G(z)$ can be pulled outside of the differentiation because the plant is independent of the filter coefficients. This assumption is valid under the assumption of slow control filter adaptation. Evaluating the gradient term in Equation 3.8 for a single filter coefficient gives

$$\frac{\partial y(n)}{\partial b_k(n)} = x(n-k) + \sum_{i=1}^{I_a} a_i(n) \frac{\partial \hat{d}(n-i)}{\partial b_k(n)}. \tag{3.9}$$

$$\frac{\partial y(n)}{\partial a_k(n)} = \hat{d}(n-k) + \sum_{i=1}^{I_a} a_i(n) \frac{\partial \hat{d}(n-i)}{\partial a_k(n)} \tag{3.10}$$

These equations result from applying the chain rule to Equation 3.3. The second terms in Equations 3.9-3.10 result from the fact that the signal driving the feedback filter $\hat{d}(n)$ is not independent of the control filter coefficients. Computation of these derivatives is problematic because of their own recursive nature. Due to the presence of the feedback path, the past values of $\hat{d}(n)$ depend on past values of $a_k(n)$ and $b_k(n)$. With the goal of forming a proper gradient filter, it is necessary to express Equations 3.9-3.10 in a form where the output is a filtered version of previous inputs and outputs. Because the partial derivatives on the right hand side are taken with respect to the current filter coefficient values, there is no recursion. A common assumption in adaptive IIR filtering is that for slow adaptation (small α), $\boldsymbol{w}(n) \approx \boldsymbol{w}(n-1) \approx \cdots \approx \boldsymbol{w}(n-I_a+1)$ [85]. Here it is assumed that the adaptation is occurring slowly compared to the timescales (*i.e.*, impulse response time) of the plant dynamics, which is an assumption made in the derivation of the FxLMS algorithm [2]. In this case, Equations 3.9-3.10 become

$$\frac{\partial y(n)}{\partial b_k(n)} = x(n-k) + \sum_{i=1}^{I_a} a_i(n) \frac{\partial \hat{d}(n-i)}{\partial b_k(n-i)}. \tag{3.11}$$

$$\frac{\partial y(n)}{\partial a_k(n)} = \hat{d}(n-k) + \sum_{i=1}^{I_a} a_i(n) \frac{\partial \hat{d}(n-i)}{\partial a_k(n-i)} \tag{3.12}$$

To express the gradient in a true recursive form, observe that

$$\begin{aligned}\hat{d}(n-i) &= e(n-i) - \hat{G}(z)\,y(n-i) \\ &= d(n-i) + \Delta G(z)\,y(n-i),\end{aligned} \tag{3.13}$$

where $\Delta G(z) = G(z) - \hat{G}(z)$. Noting that $\Delta G(z)$ and $d(n-i)$ are independent of the filter coefficients, Equations 3.11-3.12 become

$$\frac{\partial y(n)}{\partial b_k(n)} = x(n-k) + \sum_{i=1}^{I_a} a_i(n) \sum_{j=0}^{J-1} \Delta g_j \frac{\partial y(n-i-j)}{\partial b_k(n-i-j)}, \tag{3.14}$$

$$\frac{\partial y(n)}{\partial a_k(n)} = \hat{d}(n-k) + \sum_{i=1}^{I_a} a_i(n) \sum_{j=0}^{J-1} \Delta g_j \frac{\partial y(n-i-j)}{\partial a_k(n-i-j)} \tag{3.15}$$

where it is assumed that the transfer function of the modeling error can be represented by an FIR filter with J coefficients. These equations can now be computed since they are recursive in the partial derivatives. For convenience, define

$$u_k(n) = \frac{\partial y(n)}{\partial b_k(n)} \qquad v_k(n) = \frac{\partial y(n)}{\partial a_k(n)}, \tag{3.16}$$

so that Equations 3.14-3.15 can be written

$$u_k(n) = x(n-k) + \sum_{i=1}^{I_a} a_i(n) \sum_{j=0}^{J-1} \Delta g_j\, u_k(n-i-j). \tag{3.17}$$

$$v_k(n) = \hat{d}(n-k) + \sum_{i=1}^{I_a} a_i(n) \sum_{j=0}^{J-1} \Delta g_j\, v_k(n-i-j) \tag{3.18}$$

Equations 3.17-3.18 are expressed in form of recursive filters as

$$u_k(n) = \left(\frac{1}{1-\Delta G(z)A(z)}\right) x(n-k) \tag{3.19}$$

$$v_k(n) = \left(\frac{1}{1-\Delta G(z)A(z)}\right) \hat{d}(n-k), \tag{3.20}$$

where

$$A(z) = a_1(n)z^{-1} + \cdots + a_{I_a}(n)z^{-I_a}. \tag{3.21}$$

Note that there are no restrictions on the structure of $\Delta G(z)$; it may be parameterized as a scalar, an FIR, or an IIR filter. Here, it is modeled as a J length FIR filter for notational convenience. The partial derivatives can be written in vector form as

$$\boldsymbol{\phi}(n) = \boldsymbol{h}(n) + \sum_{i=1}^{I_a} \sum_{j=0}^{J-1} a_i(n) \Delta g_j \boldsymbol{\phi}(n-i-j), \tag{3.22}$$

where the vector of partial derivatives is defined as

$$\boldsymbol{\phi}(n) = \begin{bmatrix} u_0(n) & u_1(n) & \cdots & u_{I_b-1}(n) & v_1(n) & v_2(n) & \cdots & v_{I_a}(n) \end{bmatrix}^T. \tag{3.23}$$

It is apparent that if the modeling error is neglected $\boldsymbol{\phi}(n) = \boldsymbol{h}(n)$ and what results is the well known FxLMS algorithm for a hybrid controller. To compute the gradient the vector of partial derivatives is then filtered by the plant response to generate a vector of filtered reference signals given by

$$\boldsymbol{r}(n) = \sum_{j=0}^{J-1} g_j \boldsymbol{\phi}(n-j). \tag{3.24}$$

The gradient in Equation 3.8 can now be written in vector form as

$$\nabla_{w(n)} J(n) = \boldsymbol{r}(n) e(n), \tag{3.25}$$

which leads to the update equation

$$\boldsymbol{w}(n+1) = \boldsymbol{w}(n) - \alpha \boldsymbol{r}(n) e(n). \tag{3.26}$$

Since a perfect model of the plant is not available in practice, an estimate must be used and the update equation is expressed as

$$\boldsymbol{w}(n+1) = \boldsymbol{w}(n) - \alpha \hat{\boldsymbol{r}}(n) e(n), \tag{3.27}$$

where $\hat{\boldsymbol{r}}(n)$ is generated using an estimate of the plant response. These filtered reference signals are generated using the effective plant response, which takes into account the presence of the feedback path. It is expected that the more accurate full gradient estimate will result in better convergence behavior relative to FxLMS, which uses only the first term in Equation 3.22. Unfortunately, the useage of the full gradient does not appear to have any ability to improve the robustness of the algorithm due to the closed loop transfer function remaining unchanged. With this being said, it was pointed out in [101] that LMS based adaptive algorithms can diverge independently of the feedback loop becoming unstable. Therefore, it seems possible that in certain scenarios where the FxLMS algorithm would diverge independent of feedback loop instabilities, the full gradient algorithm could converge to the optimum. However, regardless of the gradient estimate being used, if the coefficients are adapted into a region corresponding to an unstable feedback loop then the performance surface becomes non-quadratic and the controller will diverge.

3.2 Multichannel Formulation

The derivation of the multichannel full gradient algorithm is exactly analogous to the single channel case. As in the single channel case, a vector formulation of the multichannel algorithm will be presented at the end of this section. The approach is similar to that in [2] but is complicated by the non-zero modeling error assumption.

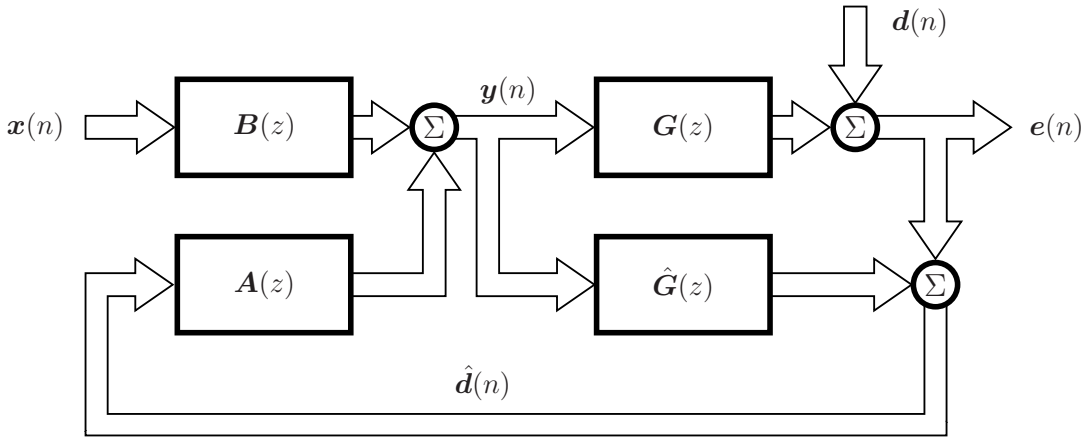

Figure 3.2: Block diagram of a multichannel hybrid active noise control system.

3.2.1 Full gradient algorithm

The block diagram of the multichannel hybrid controller is shown in Figure 3.2. The control system consists of K reference signals, L error sensors, and M control actuators. The matrix of plant responses and its estimate are denoted $\boldsymbol{G}(z)$ and $\hat{\boldsymbol{G}}(z)$, respectively. The internal model of the plant is used to generate L reference signals $\hat{\boldsymbol{d}}(n)$ (one from each error sensor) that drive the matrix of feedback filters $\boldsymbol{A}(z)$. The matrix of feedforward filters $\boldsymbol{B}(z)$ are driven by the vector of reference signals $\boldsymbol{x}(n)$. The matrices of feedforward and feedback control filters are parameterized as MK and ML FIR filters, respectively. If it is assumed that each path can be accurately represented by a J-th order FIR filter, the vector of error signals can be expressed as

$$\boldsymbol{e}(n) = \boldsymbol{d}(n) + \sum_{j=0}^{J-1} \boldsymbol{G}_j \boldsymbol{y}(n-j), \tag{3.28}$$

where $\boldsymbol{G}_j$ is an $L \times M$ matrix containing the j-th coefficient of the impulse responses for each path. The vectors in Equation 3.28 are defined as

$$\boldsymbol{e}(n) = \begin{bmatrix} e_1(n) & e_2(n) & \cdots & e_L(n) \end{bmatrix}^T, \tag{3.29}$$

$$\boldsymbol{d}(n) = \begin{bmatrix} d_1(n) & d_2(n) & \cdots & d_L(n) \end{bmatrix}^T, \tag{3.30}$$

and

$$\boldsymbol{y}(n) = \begin{bmatrix} y_1(n) & y_2(n) & \cdots & y_M(n) \end{bmatrix}^T. \tag{3.31}$$

The cost function to be minimized is the instantaneous sum of the squared error signals. This can be written as the inner product of the error signal vectors as

$$J = \frac{1}{2} \boldsymbol{e}^T(n) \boldsymbol{e}(n). \tag{3.32}$$

Similarly to the single channel case, the gradient can be expressed

$$\nabla_{\boldsymbol{w}(n)} J = \left\{ \sum_{j=0}^{J-1} \boldsymbol{G}_j \frac{\partial \boldsymbol{y}(n-j)}{\partial \boldsymbol{w}(n)} \right\} \boldsymbol{e}(n), \tag{3.33}$$

where $\boldsymbol{w}(n)$ is the vector of control filter coefficients. The vector of control signals can be expressed as

$$\boldsymbol{y}(n) = \sum_{i=0}^{I_b-1} \boldsymbol{b}_i(n)\mathbf{x}(n-i) + \sum_{i=1}^{I_a} \boldsymbol{a}_i(n)\hat{\boldsymbol{d}}(n-i), \tag{3.34}$$

where $\boldsymbol{b}_i(n)$ is an $M \times K$ vector of feedforward filter coefficients defined as

$$\boldsymbol{b}_i(n) = \begin{bmatrix} b_{11i}(n) & b_{12i}(n) & \cdots & b_{1Ki}(n) \\ b_{21i}(n) & b_{22i}(n) & \cdots & b_{2Ki}(n) \\ \vdots & & \ddots & \\ b_{M1i}(n) & b_{M2i}(n) & \cdots & b_{MKi}(n) \end{bmatrix} \tag{3.35}$$

and $\boldsymbol{a}_i(n)$ is an $M \times L$ matrix of feedback filter coefficients defined as

$$\boldsymbol{a}_i(n) = \begin{bmatrix} a_{11i}(n) & a_{12i}(n) & \cdots & a_{1Li}(n) \\ a_{21i}(n) & a_{22i}(n) & \cdots & a_{2Li}(n) \\ \vdots & & \ddots & \\ a_{M1i}(n) & a_{M2i}(n) & \cdots & a_{MLi}(n) \end{bmatrix}. \tag{3.36}$$

If the reference signals are contained in a vector given by

$$\boldsymbol{h}(n) = \begin{bmatrix} x_1(n) & x_2(n) & \cdots & x_K(n) & \hat{d}_1(n-1) & \hat{d}_2(n-1) & \cdots & \hat{d}_L(n-1) \end{bmatrix}^T, \tag{3.37}$$

and the matrices of coefficients are grouped as

$$\boldsymbol{W}(n) = \begin{bmatrix} \boldsymbol{b}_i(n) & \boldsymbol{a}_i(n) \end{bmatrix}, \tag{3.38}$$

then the vector of control signals can be expressed compactly as

$$\boldsymbol{y}(n) = \sum_{i=0}^{I} \boldsymbol{W}_i(n)\boldsymbol{h}(n-i), \tag{3.39}$$

where it was assumed that $I_b = I_a = I$. In general the number of coefficients can vary but the algorithm is simpler to implement if they are equal. To compute the partial derivatives of the control signal with respect to each filter coefficient, it is helpful to look at the derivative of the m-th control signal with respect to an individual feedforward and feedback coefficient. First observe that the m-th control signal can be expressed as

$$y_m(n) = \sum_{k=1}^{K} \sum_{i=0}^{I_b-1} b_{mki}(n)x_k(n-i) + \sum_{l=1}^{L} \sum_{i=1}^{I_a} a_{mli}(n)\hat{d}_l(n-i). \tag{3.40}$$

The partial derivative with respect to the $m'k'i'$-th feedforward filter coefficient is

$$\frac{\partial y_m(n)}{\partial b_{m'k'i'}(n)} = \begin{cases} x_{k'}(n-i') + \sum_{l=1}^{L}\sum_{i=1}^{I_a} a_{mli}(n)\frac{\partial \hat{d}_l(n-i)}{\partial b_{m'k'i'}(n)}, & \text{if m=m'} \\ \sum_{l=1}^{L}\sum_{i=1}^{I_a} a_{mli}(n)\frac{\partial \hat{d}_l(n-i)}{\partial b_{m'k'i'}(n)}, & \text{otherwise.} \end{cases} \tag{3.41}$$

Note that subscripts with 's are simply dummy variables used to indicate an arbitrary coefficient of with we are taking the partial derivative with respect to. As in the single channel case, the second term arises because the signal driving the feedback filter is not independent of the control filter coefficients. The conditional nature of this expression results from the fact that the m-th control signal is independent of the feedforward filters generating the other $M-1$ control signals. To clarify, consider a simple feedforward system with a single reference signal $x(n)$ and $L = M = I_b = 2$. The first control signal is

$$y_1(n) = b_{10}(n)x(n) + b_{11}(n)x(n-1). \tag{3.42}$$

The partial derivatives with respect to the b_{1i} coefficients are delayed versions of the reference signal whereas partial derivatives with respect to the b_{2i} coefficients are zero. Thus the terms where $m \neq m'$ are not functions of the signals driving the filter and consist only of the modeling error term. This was not an issue in the single channel case since there was only a single control signal. The partial derivative with respect to the $m'l'i'$-th feedback filter coefficient is

$$\frac{\partial y_m(n)}{\partial a_{m'l'i'}(n)} = \begin{cases} \hat{d}_{l'}(n-i') + \sum_{l=1}^{L}\sum_{i=1}^{I_a} a_{mli}(n)\frac{\partial \hat{d}_l(n-i)}{\partial a_{m'l'i'}(n)}, & \text{if m=m'} \\ \sum_{l=1}^{L}\sum_{i=1}^{I_a} a_{mli}(n)\frac{\partial \hat{d}_l(n-i)}{\partial a_{m'l'i'}(n)}, & \text{otherwise,} \end{cases} \tag{3.43}$$

where the reason for the conditional nature of the expression is the same as for the feedforward partial derivatives. It will again be assumed that the coefficients are adapting at a rate that is small compared with the timescales of the plant dynamics such that the partial derivatives can be rewritten

$$\frac{\partial y_m(n)}{\partial b_{m'k'i'}(n)} = \begin{cases} x_{k'}(n-i') + \sum_{l=1}^{L}\sum_{i=1}^{I_a} a_{mli}(n)\frac{\partial \hat{d}_l(n-i)}{\partial b_{m'i'}(n-i)}, & \text{if m=m'} \\ \sum_{l=1}^{L}\sum_{i=1}^{I_a} a_{mli}(n)\frac{\partial \hat{d}_l(n-i)}{\partial b_{m'k'i'}(n-i)}, & \text{otherwise} \end{cases} \tag{3.44}$$

$$\frac{\partial y_m(n)}{\partial a_{m'l'i'}(n)} = \begin{cases} \hat{d}_{l'}(n-i') + \sum_{l=1}^{L}\sum_{i=1}^{I_a} a_{mli}(n)\frac{\partial \hat{d}_l(n-i)}{\partial a_{m'l'i'}(n-i)}, & \text{if m=m'} \\ \sum_{l=1}^{L}\sum_{i=1}^{I_a} a_{li}(n)\frac{\partial \hat{d}_l(n-i)}{\partial a_{m'l'i'}(n-i)}, & \text{otherwise.} \end{cases} \tag{3.45}$$

These partial derivatives can be written recursively by observing that the feedback reference signals,

$$\hat{d}_l(n-i) = d_l(n-i) + \sum_{m=1}^{M}\sum_{j=0}^{J-1} \Delta g_{lmj}\, y_m(n-i-j), \tag{3.46}$$

where Δg_{lmj} is the j-th coefficient of the FIR representing the modeling error in the path from the m-th actuator to the l-th sensor, can be substituted into Equations 3.44-3.45 to obtain

$$\frac{\partial y_m(n)}{\partial b_{m'k'i'}(n)} = \begin{cases} x_{k'}(n-i') + \sum_{l=1}^{L}\sum_{i=1}^{I_a} a_{mli}(n) \sum_{m=1}^{M}\sum_{j=0}^{J-1} \Delta g_{lmj} \dfrac{\partial y_m(n-i-j)}{\partial b_{m'k'i'}(n-i-j)}, & \text{if m=m'} \\ \sum_{l=1}^{L}\sum_{i=1}^{I_a} a_{mli}(n) \sum_{m=1}^{M}\sum_{j=0}^{J-1} \Delta g_{lmj} \dfrac{\partial y_m(n-i-j)}{\partial b_{m'k'i'}(n-i-j)}, & \text{otherwise} \end{cases} \tag{3.47}$$

$$\frac{\partial y_m(n)}{\partial a_{m'l'i'}(n)} = \begin{cases} \hat{d}_{l'}(n-i') + \sum_{l=1}^{L}\sum_{i=1}^{I_a} a_{mli}(n) \sum_{m=1}^{M}\sum_{j=0}^{J-1} \Delta g_{lmj} \dfrac{\partial y_m(n-i-j)}{\partial a_{m'l'i'}(n-i-j)}, & \text{if m=m'} \\ \sum_{l=1}^{L}\sum_{i=1}^{I_a} a_{mli}(n) \sum_{m=1}^{M}\sum_{j=0}^{J-1} \Delta g_{lmj} \dfrac{\partial y_m(n-i-j)}{\partial a_{m'l'i'}(n-i-j)}, & \text{otherwise.} \end{cases} \tag{3.48}$$

Now these equations are recursive in the partial derivative terms and their outputs may be computed. Again for convenience define

$$u_{mm'k'i'}(n) = \frac{\partial y_m(n)}{\partial b_{m'k'i'}(n)} \qquad v_{mm'l'i'}(n) = \frac{\partial y_m(n)}{\partial a_{m'l'i'}(n)} \tag{3.49}$$

where the first subscript corresponds to the control signal being differentiated and the remaining correspond to the index of the filter coefficient of which it is being differentiated with respect to. The partial derivatives can then be written

$$u_{mm'k'i'}(n) = \begin{cases} x_{k'}(n-i') + \sum_{l=1}^{L}\sum_{i=1}^{I_a} a_{mli}(n) \sum_{m=1}^{M}\sum_{j=0}^{J-1} \Delta g_{lmj}\, u_{mm'k'i'}(n-i-j), & \text{if } m = m' \\ \sum_{l=1}^{L}\sum_{i=1}^{I_a} a_{mli}(n) \sum_{m=1}^{M}\sum_{j=0}^{J-1} \Delta g_{lmj}\, u_{mm'k'i'}(n-i-j), & \text{otherwise} \end{cases} \tag{3.50}$$

$$v_{mm'l'i'}(n) = \begin{cases} \hat{d}_{l'}(n-i') + \sum_{l=1}^{L}\sum_{i=1}^{I_a} a_{mli}(n) \sum_{m=1}^{M}\sum_{j=0}^{J-1} \Delta g_{lmj}\, v_{mm'l'i'}(n-i-j), & \text{if } m = m' \\ \sum_{l=1}^{L}\sum_{i=1}^{I_a} a_{mli}(n) \sum_{m=1}^{M}\sum_{j=0}^{J-1} \Delta g_{lmj}\, v_{mm'l'i'}(n-i-j), & \text{otherwise.} \end{cases} \tag{3.51}$$

The partial derivatives can be written in vector form as

$$\boldsymbol{\Phi}(n) = \boldsymbol{H}(n) + \sum_{i=1}^{I_a}\sum_{j=0}^{J-1} \boldsymbol{a}_i(n) \Delta \boldsymbol{G}_j \boldsymbol{\Phi}(n-i-j), \tag{3.52}$$

where $\boldsymbol{H}(n)$ is a matrix of appropriate dimensions containing the reference signals, $\Delta\boldsymbol{G}_j$ is an $L \times M$ matrix containing the j-th coefficients of the FIRs representing the modeling errors, and $\boldsymbol{a}_i(n)$ was previously defined. The matrix of partial derivatives is formed by first defining the vectors

$$\boldsymbol{u}_{mi}(n) = \begin{bmatrix} u_{m11i}(n) & u_{m12i}(n) & \cdots & u_{m1Ki}(n) & u_{m21i}(n) & \cdots & u_{m2Ki}(n) & \cdots & u_{mMKi}(n) \end{bmatrix}^T, \tag{3.53}$$

$$\boldsymbol{v}_{mi}(n) = \begin{bmatrix} v_{m11i}(n) & v_{m12i}(n) & \cdots & v_{m1Li}(n) & v_{m21i}(n) & \cdots & v_{m2Li}(n) & \cdots & v_{mMLi}(n) \end{bmatrix}^T, \tag{3.54}$$

where

$$\boldsymbol{u}_{mi}(n) = \frac{\partial y_m(n)}{\partial \bar{\boldsymbol{b}}_i(n)} \tag{3.55}$$

$$\boldsymbol{v}_{mi}(n) = \frac{\partial y_m(n)}{\partial \bar{\boldsymbol{a}}_i(n)} \tag{3.56}$$

correspond to vectors of partial derivatives of the m-th control signal with respect to the i-th coefficient of each filter. Here $\bar{\boldsymbol{b}}_i(n)$ and $\bar{\boldsymbol{a}}_i(n)$ are formed by vectorizing the matrices of coefficients, *i.e.*, $\bar{\boldsymbol{b}}_i(n) = \texttt{vec}\left(\boldsymbol{b}_i^T(n)\right)$ and $\bar{\boldsymbol{a}}_i(n) = \texttt{vec}\left(\boldsymbol{a}_i^T(n)\right)$, where $\texttt{vec}(\boldsymbol{P})$ denotes the vector stacking of the columns of the matrix $\boldsymbol{P}$. Next define the matrices

$$\boldsymbol{U}_i(n) = \begin{bmatrix} \boldsymbol{u}_{1i}(n) & \boldsymbol{u}_{2i}(n) & \cdots & \boldsymbol{u}_{Mi}(n) \end{bmatrix}, \tag{3.57}$$

$$\boldsymbol{V}_i(n) = \begin{bmatrix} \boldsymbol{v}_{1i}(n) & \boldsymbol{v}_{2i}(n) & \cdots & \boldsymbol{v}_{Mi}(n) \end{bmatrix}, \tag{3.58}$$

which again corresponds to partial derivatives taken with respect to the i-th coefficient in each filter. These matrices can be concatenated to form

$$\boldsymbol{U}(n) = \begin{bmatrix} \boldsymbol{U}_0^T(n) & \boldsymbol{U}_1^T(n) & \cdots & \boldsymbol{U}_{I_b-1}^T(n) \end{bmatrix}^T \tag{3.59}$$

$$\boldsymbol{V}(n) = \begin{bmatrix} \boldsymbol{V}_1^T(n) & \boldsymbol{V}_2^T(n) & \cdots & \boldsymbol{V}_{I_a}^T(n) \end{bmatrix}^T. \tag{3.60}$$

The matrix of partial derivatives can now be espressed as

$$\boldsymbol{\Phi}(n) = \begin{bmatrix} \boldsymbol{U}(n) & \boldsymbol{V}(n) \end{bmatrix} \tag{3.61}$$

Recall that computation of the gradient,

$$\boldsymbol{\nabla}_{\boldsymbol{w}(n)} J = \left\{ \sum_{j=0}^{J-1} \boldsymbol{G}_j \boldsymbol{\Phi}(n-j) \right\} \boldsymbol{e}(n), \tag{3.62}$$

requires the matrix of partial derivatives to be filtered by the matrix of plant response. This yields a matrix of filtered reference signals given by

$$\boldsymbol{R}(n) = \sum_{j=0}^{J-1} \boldsymbol{G}_j \boldsymbol{\Phi}(n-j). \tag{3.63}$$

The gradient of the error surface can then be written

$$\nabla_{\boldsymbol{w}(n)} J = \boldsymbol{R}^T(n)\boldsymbol{e}(n). \tag{3.64}$$

A particularly simple expression for the update equation can be written if the filter coefficients are written in vector form such that

$$\boldsymbol{w}(n) = \begin{bmatrix} \boldsymbol{b}(n) & \boldsymbol{a}(n) \end{bmatrix}^T, \tag{3.65}$$

where

$$\boldsymbol{b}(n) = \begin{bmatrix} \mathtt{vec}\left(\boldsymbol{b}_0^T(n)\right) & \mathtt{vec}\left(\boldsymbol{b}_1^T(n)\right) & \cdots & \mathtt{vec}\left(\boldsymbol{b}_{I_b-1}^T(n)\right) \end{bmatrix}^T \tag{3.66}$$

$$\boldsymbol{a}(n) = \begin{bmatrix} \mathtt{vec}\left(\boldsymbol{a}_1^T(n)\right) & \mathtt{vec}\left(\boldsymbol{a}_2^T(n)\right) & \cdots & \mathtt{vec}\left(\boldsymbol{a}_{I_a}^T(n)\right) \end{bmatrix}^T. \tag{3.67}$$

With the vector of coefficients defined, the update equation for the adaptive filters is described by

$$\boldsymbol{w}(n+1) = \boldsymbol{w}(n) - \alpha \boldsymbol{R}^T(n)\boldsymbol{e}(n). \tag{3.68}$$

In practice a perfect model of the plant is not available and an estimate must be used. The corresponding update equation is

$$\boldsymbol{w}(n+1) = \boldsymbol{w}(n) - \alpha \hat{\boldsymbol{R}}^T(n)\boldsymbol{e}(n), \tag{3.69}$$

where $\hat{\boldsymbol{R}}(n)$ is generated using an estimate of the plant response.

3.3 Algorithm analysis

In this section, some qualitative observations regarding the discussion of the multichannel full gradient algorithm are discussed. These observations also carry over to the single channel case. It is apparent that the difference between the full gradient and the filtered reference LMS algorithms involves the recursive filtering of the term that is a function of the modeling error and the feedback filter coefficients. Since the filter coefficient's values are set according to the update equation, the only term that can be chosen by the designer is the modeling error. Recall that the gradient is

$$\hat{\nabla}_{\boldsymbol{w}(n)} J = \left\{ \sum_{j=0}^{J-1} \hat{\boldsymbol{G}}_j \boldsymbol{\Phi}(n-j) \right\} \boldsymbol{e}(n), \tag{3.70}$$

where

$$\boldsymbol{\Phi}(n) = \left[\frac{\partial \boldsymbol{y}(n)}{\partial \boldsymbol{w}(n)} \right]^T. \tag{3.71}$$

Recall that the quantity $\boldsymbol{\Phi}(n)$ is composed of two terms,

$$\boldsymbol{\Phi}(n) = \boldsymbol{H}(n) + \boldsymbol{F}(\Delta \boldsymbol{G},\ \boldsymbol{A}(n)) \tag{3.72}$$

where the term $\sum_{i=1}^{I_a}\sum_{j=0}^{J-1} \boldsymbol{a}_i(n)\Delta\boldsymbol{G}_j\boldsymbol{\Phi}(n-i-j)$ has been written as a general matrix function of the modeling error and the feedback filters, $\boldsymbol{F}(\Delta\boldsymbol{G},\ \boldsymbol{A}(n))$. The matrix of filtered reference signals, obtained by filtering $\boldsymbol{\Phi}(n)$ by the plant response, can then be written

$$\hat{\boldsymbol{R}}(n) = \hat{\boldsymbol{G}}(z)\boldsymbol{H}(n) + \hat{\boldsymbol{G}}(z)\boldsymbol{F}(\Delta\boldsymbol{G},\ \boldsymbol{A}(n))\,. \tag{3.73}$$

Some interesting observations regarding the performance of the full gradient algorithm can be made from this equation. The first term in Equation 3.73 is what would be used in the traditional implementation of the FxLMS algorithm to form the filtered reference signals. The convergence behavior of the feedforward multichannel FxLMS algorithm is known to depend on the eigenvalue spread of the matrix

$$E\left[\hat{\boldsymbol{R}}_x^T(n)\boldsymbol{R}_x(n)\right], \tag{3.74}$$

where $\hat{\boldsymbol{R}}_x(n)$ is assumed to have been generated by filtering only the external reference signals $\boldsymbol{x}(n)$ by the plant model [2]. The subscript is meant to imply that the matrix of filtered reference signals is generated using only the first term in Equation 3.73. It can be shown that the adaptation process will be stable and converge to it's optimum value provided the plant and plant model satisfy a strictly positive real condition. In a hybrid control setting, the situation is slightly more complicated due to the dependence of the feedback reference signals on prior filter coefficient values, which are changing with time. In this case, stability of the adaptive algorithm depends on the eigenvalue spread of the matrix

$$E\left[\hat{\boldsymbol{R}}^T(n)\boldsymbol{R}(n)\right], \tag{3.75}$$

where $\hat{\boldsymbol{R}}(n)$ is now given by Equation 3.73. It is important here to note the difference between adaptive algorithm stability and feedback loop stabilities. The conclusion is that the convergence behavior of the full gradient algorithm relies on the ability of the term $\boldsymbol{F}(\Delta\boldsymbol{G},\ \boldsymbol{A}(n))$ to vary the eigenvalue spread of Equation 3.75 such that faster convergence is achieved. This can be problematic since computation of the gradient requires this term to be filtered by the model of the plant response, which recall is in error.

A convenient case to consider is when the modeling error is known exactly. Although this scenario has limited practical relevance and is only achievable in a simulation environment, it can be used to draw some conclusions regarding the performance of the full gradient algorithm. In this case, the term $\boldsymbol{F}(\Delta\boldsymbol{G},\ \boldsymbol{A}(n))$ is known with perfect accuracy and using the full gradient in the update equation should theoretically allow the algorithm to converge faster. Intuitively, the fastest convergence should be expected when $\boldsymbol{F}(\Delta\boldsymbol{G},\ \boldsymbol{A}(n))$ has the largest influence in the gradient, since this term is not present in FxLMS. For this to be possible, $\Delta\boldsymbol{G}$ will likely have to be large, implying that the plant model $\hat{\boldsymbol{G}}$ is in error by a similar amount. Since to compute the gradient, $\boldsymbol{H}(n)$ and $\boldsymbol{F}(\Delta\boldsymbol{G},\ \boldsymbol{A}(n))$ are filtered by the plant model, the gradient estimate becomes decreasingly accurate as the modeling error grows. Thus while the partial derivative (before filtering by the plant model) is mathematically correct, with the exception of the slow

adaptation assumption, the gradient estimate will still be in error due to the imperfect plant model. Consequently, the convergence speed of the full gradient algorithm is expected to improve relative to FxLMS as $\Delta \boldsymbol{G}$ increases up to the point where $\Delta \boldsymbol{G}$ is large enough to destabilize the feedback loop. This being said, many algorithms that offer improved convergence properties rely on normalizing the performance surface by inverting potentially large autocorrelation matrices, or performing an eigen-decomposition to rotate the signals into their principle axes, both of which can be computationally intensive. The full gradient algorithm only requires an estimate of the modeling error.

A natural question is that if a somewhat accurate estimate of the modeling error is available, why would it not simply be used to form a more accurate plant model

$$\hat{\boldsymbol{G}}_1 = \hat{\boldsymbol{G}} + \Delta \hat{\boldsymbol{G}}, \tag{3.76}$$

where $\Delta \hat{\boldsymbol{G}}$ is the estimate of the modeling error and $\hat{\boldsymbol{G}}_1$ is the improved plant estimate. If it is known that the plant will take on a particular value and not vary, then this question is valid and it likely wouldn't make sense to use the full gradient algorithm. Although in general, typical plants in active noise and vibration control are subject to uncertainties due to operating conditions and changes in the environment. For instance, the plant response in an industrial duct will change due to turbulent air flow & temperature, the plant in an active headrest/headset will change based on the listener's head position/headset fit, etc. [19]. Knowledge of the plant response would thus allow $\Delta \boldsymbol{G}$ to be designed based on this information and provide faster convergence over a wider range of expected plant responses.

3.4 Simulation

This section presents simulation results of the full gradient and FxLMS algorithms. The results presented here are for the single channel case, but the results are similar for the multichannel case. It has been shown that the update equation in the feedback and hybrid FxLMS algorithm uses an approximation of the full gradient expression. A series of simulations have been constructed to illustrate the performance differences in using the full gradient as opposed to the approximation used in FxLMS.

In each simulation, the reference signal is a 100 Hz sine wave. The disturbance is the reference signal filtered through the primary path plus a 140 Hz sine wave (i.e. an uncorrelated disturbance). The primary path from the reference signal to the error sensor is a five sample delay with unity magnitude. A low level broadband signal was added to the disturbance to simulate measurement noise. In all simulations, the sample rate was set to 1 kHz. The plant model is represented by the following FIR filter

$$\hat{G}(z) = -0.03 + 0.3z^{-1} + 1.4z^{-2} + 0.9z^{-3} - 0.4z^{-4} - 1.1z^{-5} - 0.2z^{-6} + 0.3z^{-7} + 0.07z^{-8}, \tag{3.77}$$

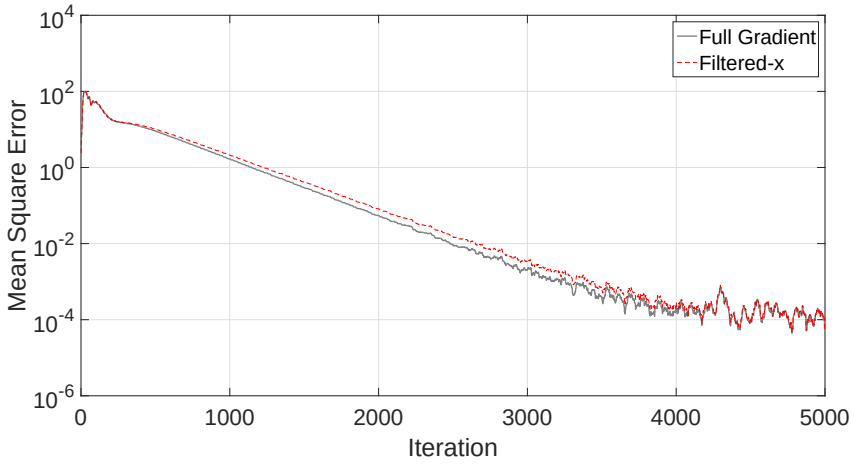

Figure 3.3: Mean squared error signal in the case of modeling errors. $G(z) = \frac{3}{4}\hat{G}(z)$

which is representative of a simple ANC plant. It is assumed that the plant is subject to a multiplicative uncertainty [52] $\Delta_m(j\omega)$, where

$$G(j\omega) = \hat{G}(j\omega)\left(1 + \Delta_m(j\omega)\right) \tag{3.78}$$

and that the uncertainty is bounded by $|\Delta_m(j\omega)| \leq \frac{1}{8}$. Therefore for the simulations, it was assumed that the modeling error $\Delta G(j\omega)$ had a magnitude of $|\frac{1}{8}\hat{G}(j\omega)|$ and zero phase. A digital FIR filter was constructed to closely match this desired magnitude and phase response. The FIR is constructed based on a weighted least squares curve fit of the desired frequency response and thus will not have exactly zero phase. The resulting FIR filter is used in the full gradient algorithm in all subsequent simulations.

To compare the performance of the simplified gradient algorithm and FxLMS, three separate simulations are presented. In the first two cases, $G(j\omega) = \frac{3}{4}\hat{G}(j\omega)$ and $G(j\omega) = \frac{5}{4}\hat{G}(j\omega)$. In these cases, the multiplicative error is $\frac{1}{4}$ and $-\frac{1}{4}$, respectively. Each case represents a scenario where the actual modeling error exceeds the bounds that were used to generate $\Delta G(j\omega)$, *i.e.*, the bounds in Equation 3.78. In the final simulation $G(z) = \hat{G}(z)$.

The control filter consists of two feedback ($I_a = 2$) and two feedforward ($I_b = 2$) coefficients. In general, only two filter weights should be necessary for the suppression of a tone. In each simulation, the step size was chosen to be half of the value that resulted in instability. The step size used in both algorithms were nearly the same value in each simulation. The results are shown in Figs. Equations 3.3-3.5. For both cases where the plant model is imperfect, the full gradient algorithm converges slightly faster than FxLMS due to a more accurate gradient estimate in the update equation. In the nominal case, the system is entirely feedforward and the gradient used in the FxLMS update is correct. The difference in convergence speed in the nominal case is negligible, as can be seen in Fig. 3.5.

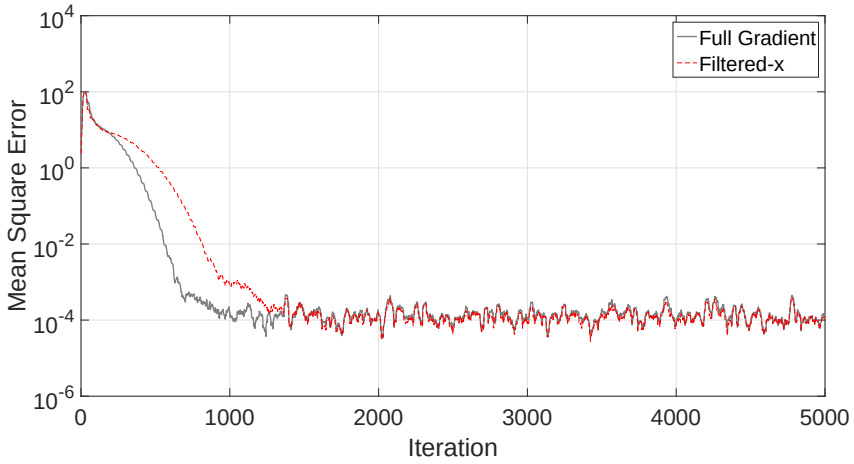

Figure 3.4: Mean squared error signal in the case of modeling errors. $G(z) = \frac{5}{4}\hat{G}(z)$

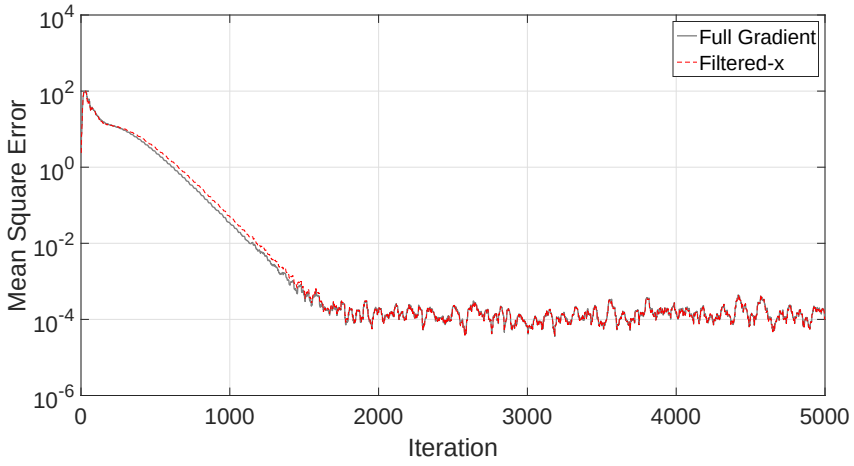

Figure 3.5: Mean squared error signal in the case of no modeling errors. $G(z) = \hat{G}(z)$

The simulation results indicate that very modest convergence improvements can be achieved by using the full gradient algorithm in cases where the plant is not operating in its nominal configuration. Even in the nominal case (Figure 3.5), where using the full gradient expression is technically incorrect (since $\Delta G(z) = 0$), no real deterioration in performance is observed. The cases where the modeling error is known exactly was also considered and the results were similar to those obtained by using the estimate given by $|\Delta G(j\omega)| \leq \frac{1}{8}$.

Some attempts to prescribe larger magnitude errors on the plant response were explored, but generally resulted in feedback loop instabilities. Pure phase errors, as well as a combination of magnitude and phase errors were also examined and generally resulted in similar performance to what is presented here. This being said, the plant model under consideration is relatively flat with a simple phase response. It is quite possible that more complicated plants, such as those containing lightly damped resonances and complex phase behavior, could exhibit considerably different performance than what is considered here.

3.5 Conclusion

In this chapter, detailed derivations of a new adaptive algorithm, referred to as the full gradient algorithm, for single channel and multichannel hybrid active control systems have been presented. The full gradient algorithm, similar to the FxLMS algorithm, is based on the method of steepest descent. By treating the hybrid control system as a single IIR filter, mathematically exact adaptation equations were derived for both single channel and multichannel hybrid control systems. Although it was found that the complete gradient depends explicitly on the modeling error, which will likely be unknown in practice, this is the first documentation of the complete update equations for hybrid control systems.

The full gradient algorithm takes into account a non-zero modeling error in the computation of the gradient and was shown in simulations to offer modest convergence improvements in certain scenarios at the expense of increased computational expense. It was then shown that the FxLMS algorithm could be easily arrived at by neglecting the modeling error in the derivation of the full gradient algorithm.

The multichannel full gradient algorithm, derived for an arbitary number of reference sensors, control actuators, and error sensors, was then presented in a compact vector form that is useful for practical implementation. The expressions for the full gradient also provide insight into how modeling errors in individual paths can influence the accuracy of the gradient estimates taken with respect to many of the seemingly unrelated filter coefficients. Some qualitative observations regarding the performance of the full gradient algorithm were also discussed.

In most practical scenarios, the FxLMS algorithm typically provides sufficient performance in most situations. Nonetheless, this approach to the derivation of FxLMS, *i.e.*, by assuming a perfect plant model in the full gradient algorithm, provides helpful insight into the algorithm's

behavior when applied in a hybrid or feedback control setting.

Chapter 4

Finite Element Modeling of an Active Headrest

In a practical active headrest, it is unlikely that microphones will be located at the ears of an occupant such that the primary noise can be canceled and noise reduction perceived. More than likely, the microphones will be located some distance behind or to the side of the head of the occupant and it will be necessary to model the local acoustic environment near the head in order to predict the noise reduction at the ears. The local acoustic environment in an active headrest, after a control system has already been implemented and is operating at steady state, will determine the spatial region around the head where noise reduction can be expected. The main focus of this chapter will be the study of these actively generated quiet zones in the context of an active headrest.

The initial results in this Chapter are similar to those presented in [35], although in this work results are presented for diffuse primary sound fields, which are considerably more difficult to model. Also, since the approach used in this chapter is based on finite element modeling, it is possible to more readily include diffraction and scattering effects, as well as to visualize the quiet zones for arbitrary geometries and headrest configurations. Both conventional ANC systems using physical error sensors as well as systems employing virtual error sensors will be explored. It is confirmed that virtual sensing is necessary in an active headrest to achieve appreciable quiet zones in the vicinity of a listener's ears.

A primary benefit of using a finite element approach to model the local acoustic environment in an active headrest is the flexibility in analyzing the system performance in practical environments. For instance, designing, fabricating, and performing an experiment to quantify the noise reduction capability of an active headrest in an automobile would be costly and time-consuming. If a suitable FE model of the vehicle were available, possibly from a computer aided design modeling tool, it would likely be much quicker to evaluate the performance in a simulation environment.

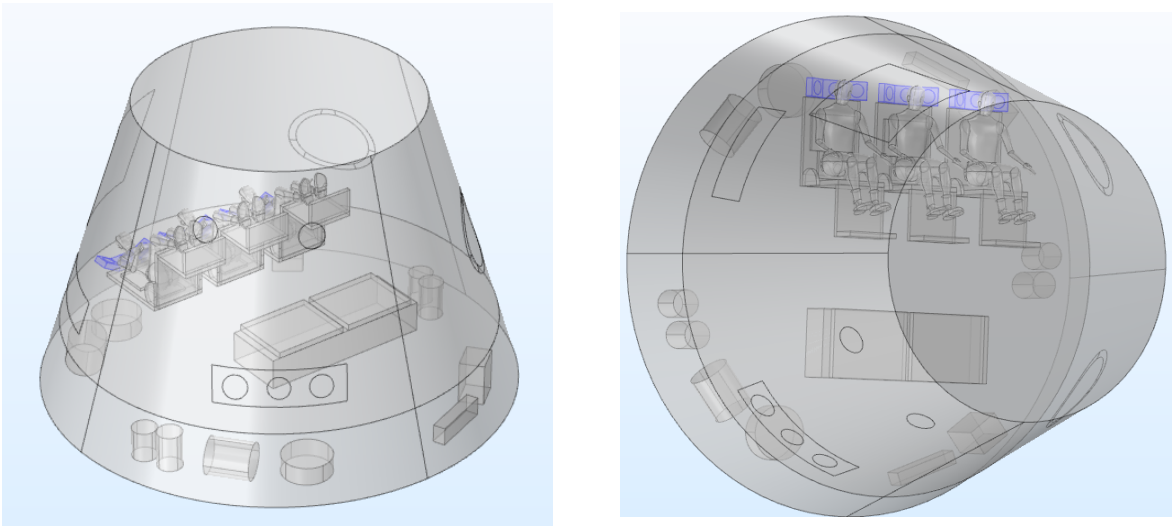

Figure 4.1: Finite element model of a semi-reverberant crew module equipped with noise canceling headrests.

The crew module on new launch vehicles will be exposed to harsh acoustic environments. The NASA Space Launch System (SLS), for example, will have the capability of delivering 70 metric tons to a low Earth orbit [102], whereas current launch vehicles are capable of only 28 metric tons [102]. The acoustic and vibration environment associated with such a high thrust vehicle will consequently be more severe than those encountered in past missions. For this reason, novel concepts and methods of reducing both low and high frequency noise in these vehicles has been a recent area of research [103, 104].

With this application in mind, a finite element model of a generic crew module has been constructed and is shown in Figures 4.1-4.2. Shown are three crew members situated in their individual seats. A conceptual design of an active headrest, highlighted in purple, can be seen in each of the figures. Each headrest contains three loudspeakers located behind each crew member. Ideally, the loudspeakers are driven such that the harsh acoustic environment inside the vehicle is mitigated, at least in the vicinity of the crew member's heads. The main focus of this chapter will be concerned with the steady state local acoustic environment surrounding the head of an occupant after the loudspeakers in the active headrest have been adjusted to minimize the ambient noise in the crew module. To make the problem slightly more tractable and to evaluate the performance of the active headrest in greater detail, a simplified numerical model is used. Details of the numerical model will be presented in the following section.

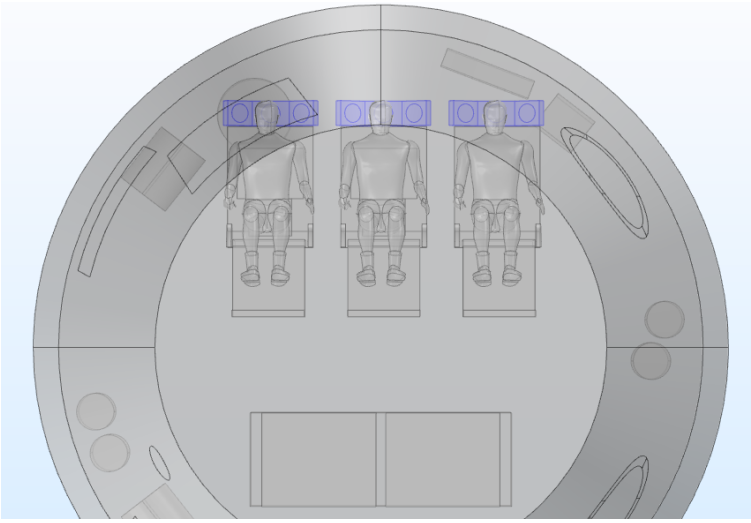

Figure 4.2: Closer view of the active headrest systems for each passenger.

4.1 Numerical model

A simplified model of the active headrest is depicted in Figure 4.3. Shown is the baffle structure which houses the loudspeakers, the microphones (represented as points), and a sphere which is meant to represent the head of a listener. Both the sphere as well as the baffle are modeled as perfectly rigid. The loudspeakers are modeled as 5-1/4" diameter circular active segments of the baffle and are driven by assigning a complex-valued normal acceleration to their surfaces. Two microphones, which will be referred to as *control microphones* or *physical microphones*, are located on either side of the head, but far enough away as to not interfere with practical head movements. These microphones are also commonly referred to as error sensors in the context of a control system. Two other microphones are located on the sphere, where the listener's ears would be, however these are not used in the operation of the control system, and are only included to monitor the attenuation at the ears. The shape of the headrest was chosen such that the side speaker baffles form 30 degree angles with respect to the yz plane. Since the frequencies at which active control is typically viable are relatively low ($<$ 1 kHz), the acoustic effects of a torso and finer geometric details associated with a seat can be ignored [35].

The boundary conditions for the model, not shown in Figure 4.3, are set to mimic an anechoic space. This is accomplished within the acoustic FE model using Perfectly Matched Layers [105]. These boundary conditions minimize reflections off the domain boundaries and ensure that only the prescribed primary field is influencing the acoustic performance of the active headrest. Although there are minimal reflections off of the domain boundaries, there are reflections off the rigid head and baffle. The mesh was chosen such that at every frequency at least six elements per acoustic wavelength were used, although to visualize the quiet zones the domain was probed using a much finer resolution. Initially, a series of two-dimensional simulations were carried out for the geometry in Figure 4.3. It was found that at certain frequencies the in-

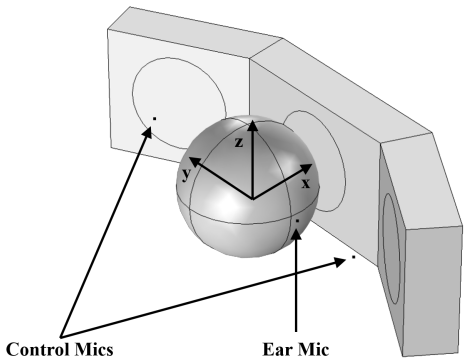

Figure 4.3: Geometry of the active headrest used in the finite element model.

terference between the incident and reflected sound fields created unrealistic pressure nodes that heavily influenced the performance of the control system. It was for this reason that a full 3D modeling approach was taken instead.

In the following sections, the acoustic performance of the active headrest will be evaluated in both plane wave and diffuse sound fields. These sound fields are chosen such that the acoustic performance can be evaluated at opposite ends of the acoustic spectrum, that is, free field (entirely anechoic) and diffuse field (entirely reverberant) conditions. Insight into the performance in a semi-reverberant acoustic environment, such as inside a crew module, can be inferred by considering the performance in these contrasting acoustic environments. In each simulation, the sound fields are modeled as background pressure fields that are described by one or more progressive plane waves with a given amplitude and phase. The next two subsections provide some details on each sound field.

4.1.1 Plane wave field formulation

The first sound field considered in this chapter is one consisting of a single progressive plane wave with an arbitrary angle of incidence. To obtain unbiased estimates of the acoustic performance, the plane wave was chosen to be symmetric about the headrest, *i.e.*, no y component. Unless otherwise noted, the plane wave is assumed to be traveling in the negative x direction. Since the plane wave is arriving from behind the headrest, the control region is in the shadow zone of the headrest. An important characteristic of the plane wave sound field is that the results are exactly repeatable. This is in contrast to the diffuse sound field, which will be discussed next, where the acoustic variables of the field are described in a statistical sense.

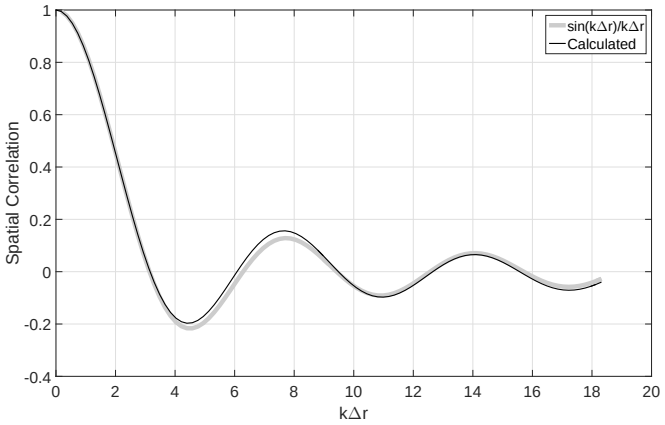

Figure 4.4: Spatial correlation function computed from the simulated acoustic field compared to the theoretical value.

4.1.2 Diffuse field formulation

A diffuse sound field can be defined as a field with sound arriving from all directions. Such a field can be approximated by a finite number of plane waves, like those discussed above, arriving from multiple directions with random phases. This model of a diffuse field is referred to as plane wave superposition [106, 107]. Because each realization is only one sample of an infinitely large population, it is necessary to consider the ensemble average of a sufficiently large set of realizations to accurately quantify the diffuse field. The pressure due to the superposition of N plane waves with random phases at any point can be written in cartesian coordinates as [108]

$$p(x,y,z,e^{j\omega t}) = \frac{1}{\sqrt{N}} \sum_{n=1}^{N} \exp\left[j\left(kxsin\theta_n cos\phi_n + kysin\theta_n sin\phi_n + kzcos\theta_n + \tilde{\phi}_n \right) \right], \qquad (4.1)$$

where the elevation angle θ_n and the azimuthal angle ϕ_n are chosen from two separate populations consisting of angles spread uniformly around a sphere. The phase $\tilde{\phi}_n$ is also chosen from a uniform distribution between 0 and 2π. To validate that the sound field described by Equation 4.1 is in fact diffuse, the spatial correlation function was compared with the theoretically predicted sinc function [109], as shown in Figure 4.4, and found to be in agreement.

Figure 4.5 shows pressure contours corresponding to plane wave and diffuse primary sound fields at 1.5 kHz and provides some visual insight into their differences. In Figure 4.5a, a single plane wave is traveling from right to left and is diffracted and scattered symmetrically by the headrest. In Figure 4.5b, the plave wave superposition method is used to form the primary sound field and it can be seen that the pressure contours are spatially random. As will be discussed in greater detail later, the spatial randomness of the diffuse sound field has adverse effects on the acoustics performance of the active headrest.

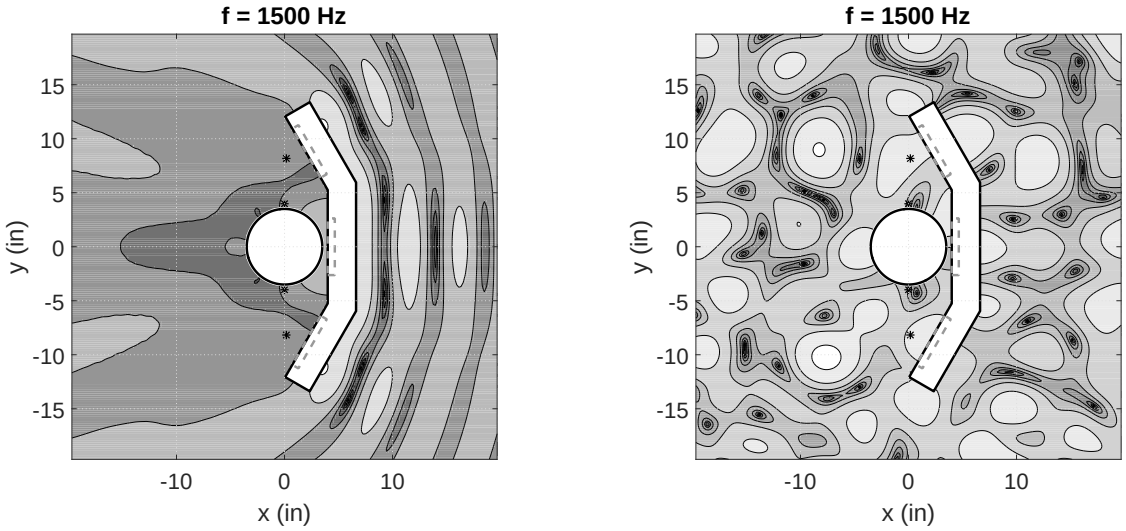

(a) Plane wave traveling from right to left.

(b) One realization of a diffuse field.

Figure 4.5: Pressure contours in plane wave and diffuse primary sound fields.

4.2 ANC at control microphones

In order to obtain sufficient attenuation at the ears of a listener, it is typically necessary to locate the error microphones, which are the control microphones in Figure 4.3, near the desired cancellation points [35]. For an active headrest, this can be challenging due to listener head movements. For the first case discussed here, the control system is adjusted to cancel the pressure at the control microphones on each side of the head. This represents the practical case where the microphones are located in non-intrusive positions, such that the listener's head is free to move. This scenario is depicted in Figure 4.8a, where the transfer responses between the right speaker and both physical microphones are also shown.

Most prior investigations of active headrests have used two loudspeakers, one for each ear. In this section, the addition of a third source will be considered. First, the dynamics describing the acoustic systems are presented.

4.2.1 Two speakers - two microphones

Initially, it will be assumed that the multichannel control system consists of two loudspeakers, located on either side of the head, whose inputs are adjusted to minimize the sum of the squared error signals measured by two control microphones. In this case, it is assumed that loudspeaker located directly behind the head is inactive and acts as a rigid segment of the speaker housing. Because there are as many loudspeakers as error microphones, the control system is able to exactly cancel the measured pressures. This configuration is initially consid-

ered because of its similarities to previous studies of active headrests [35, 47, 48]. The vector of complex responses at the error microphones is the summation of the responses due to the primary disturbance and the secondary loudspeakers such that

$$\mathbf{e}(e^{j\omega t}) = \mathbf{d}(e^{j\omega t}) + \mathbf{G}(e^{j\omega t})\mathbf{u}(e^{j\omega t}), \tag{4.2}$$

where it has been assumed that the control system is operating at steady state and at a single frequency. Here, $\mathbf{d}(e^{j\omega t})$ is the vector of complex responses due to the primary disturbance alone, $\mathbf{u}(e^{j\omega t})$ is the vector of control inputs to the loudspeakers, and $\mathbf{G}(e^{j\omega t})$ is the transfer function matrix describing the relationship between the inputs to the loudspeakers and the outputs from the error microphones. The vector of control inputs that completely cancels the pressure at the error microphones is given by

$$\mathbf{u}_{opt}(e^{j\omega t}) = -\mathbf{G}^{-1}(e^{j\omega t})\mathbf{d}(e^{j\omega t}). \tag{4.3}$$

Although this choice of control will completely cancel the pressure at the physical error sensors, it is quite possible that it may result in pressure amplifications in areas away from the error sensors [2]. It is for this reason that it is common in larger control systems to minimize the pressure at an array of sensors.

4.2.2 Three speakers - two microphones

In this section, the acoustic performance is considered with the addition of a third loudspeaker. This configuration is illustrated in Figure 4.8a, where the transfer paths between one of the secondary sources and the two physical error sensors are also shown. Because there are more loudspeakers than error microphones, the system is underdetermined and there are an infinite number of control inputs that will set the error vector to zero. One approach to compute the control input is to minimize the squared modulus of the control effort $\mathbf{u}^H\mathbf{u}$ while simultaneously constraining the error vector to be equal to zero. This constrained optimization problem can be solved using the method of Lagrange multipliers, which results in a vector of control inputs given by [2]

$$\mathbf{u}_{opt}(e^{j\omega t}) = -\mathbf{G}^H(e^{j\omega t})\left[\mathbf{G}(e^{j\omega t})\mathbf{G}^H(e^{j\omega t})\right]^{-1}\mathbf{d}(e^{j\omega t}). \tag{4.4}$$

Note that $\mathbf{G}$ is now a 2×3 matrix whose elements consist of the transfer responses from each of the three secondary sources to each physical error sensor. In general, underdetermined systems have been avoided in active noise and vibration control due to the risk of error signal amplifications and large control inputs. However, it will be seen below that the use of an additional control source can have positive effects in an active headrest control system. For a more detailed discussion of underdetermined systems, the reader is referred to [2].

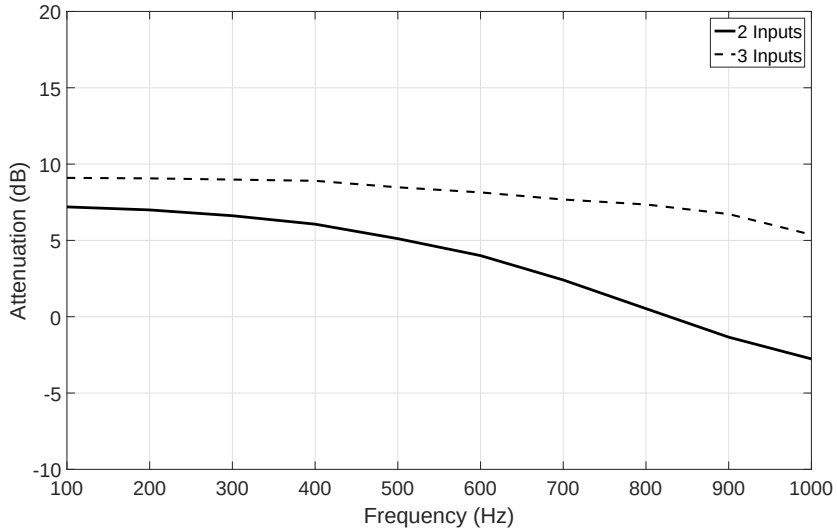

Figure 4.6: Attenuation as a function of frequency at the ear microphones when the control system is adjusted to cancel the pressure at the two control microphones. The addition of a third speaker, located behind the head, helps to improve attenuation at low frequencies.

4.2.3 Acoustic performance in a plane wave primary field

To compute the optimal control inputs, it was first necessary to identify the transfer function matrix. This is accomplished by assigning a value of unity to each of the loudspeaker elements (in the absence of the disturbance) and evaluating the complex responses at each of the control microphones. The disturbance is then measured by switching the control sources off and evaluating the complex responses at each of the control microphones. With the complex transfer function matrix and disturbance vectors formed, the optimal control input is then calculated according to either Equation 4.3 or Equation 4.4, depending on the number of loudspeakers.

The attenuation evaluated at the ear microphones has been evaluated from 100 Hz to 1000 Hz, at 100 Hz intervals for the plane wave primary field described above, and is shown in Figure 4.6. Even at lower frequencies, both systems are unable to achieve 10 dB attenuation. This was also found to be the case in the experimental results in [35]. Although quiet zones are formed around the control microphones, the characteristics of the primary pressure field near the head prevent these zones from extending to the ears. This is mainly due to the distance between the cancellation points and the ear microphones (≈ 4").

A takeaway from this figure is that the attenuation can be improved over the entire frequency range by adding a third loudspeaker, located behind the head, to the control system. Although the addition of a third loudspeaker causes the control system to be underdetermined, control inputs can still be computed that cancel the sound at the control microphones while simultane-

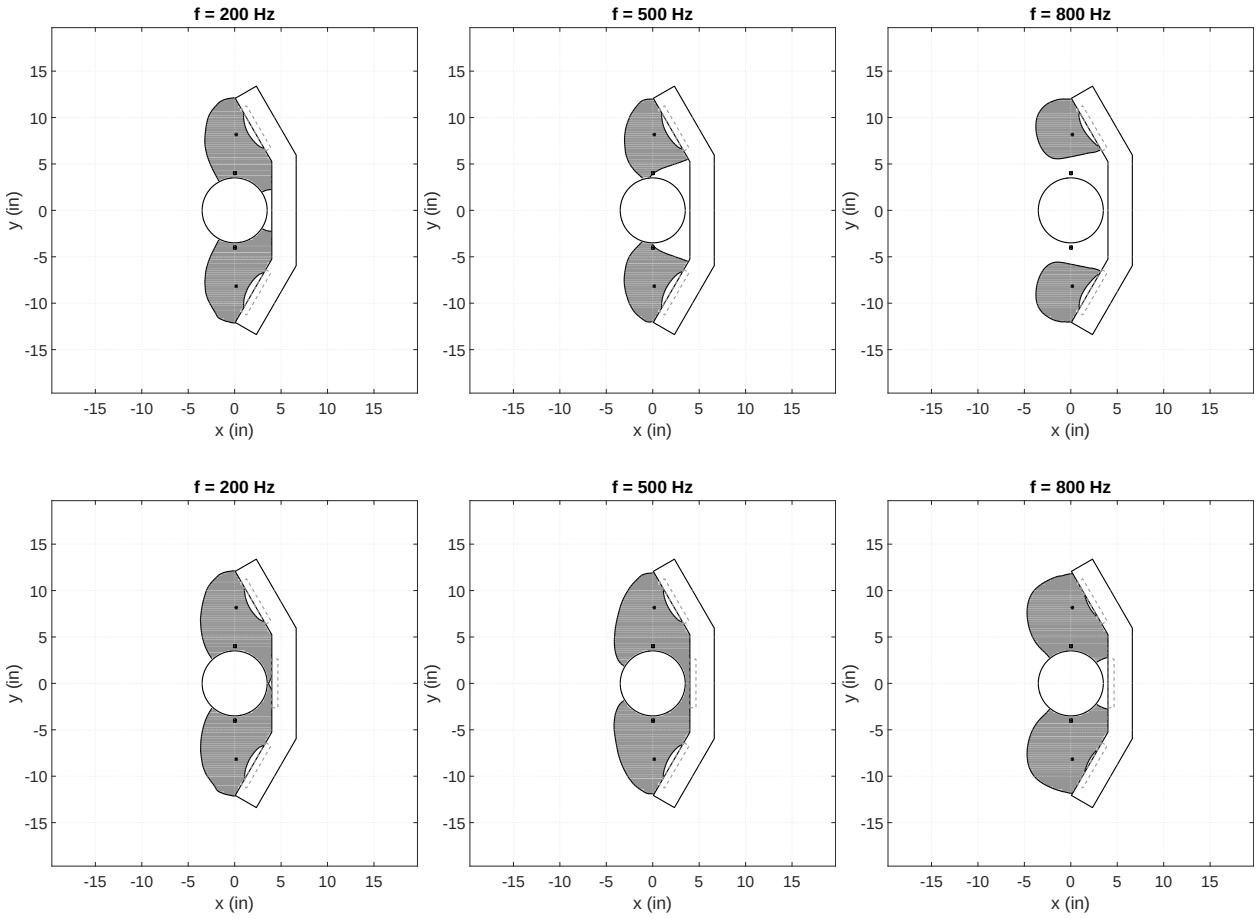

Figure 4.7: 5 dB quiet zones for an active headrest with two and three loudspeakers adjusted to cancel the pressure at the two control microphones.

ously minimizing the control effort. The other pronounced effect of adding a third loudspeaker is a broadening of the quiet zone, as can be seen in Figure 4.7. Although only the 5 dB quiet zones are shown here, it is clear that the addition of a third control source improves attenuation as well as the spatial extent of the quiet zone. This broadening of the quiet zone is due to the effect that the third loudspeaker has on the secondary radiation pattern around the head, *i.e.*, the radiation pattern due solely to the secondary loudspeakers. By locating an additional loudspeaker in the headrest, the array of secondary loudspeakers is more capable of accurately reproducing the primary sound field (although 180° out of phase) over a larger spatial region. The remaining results will correspond to the case where three control sources are used.

4.3 ANC at virtual microphones

Although the addition of a third loudspeaker improves the acoustic performance of the active headrest, the attenuation levels are still lower than what would likely be required in a practical system. The 10 dB quiet zone, which is a typical metric used to evaluate the performance of ANC systems, is not achieved at the ears using a control strategy that ignores the separation distance between the control microphones and ears. It is therefore necessary to either locate the control microphones closer to the ears, or consider an approach that will create quiet zones closer to the ears.

In this section, methods of shifting the quiet zone away from the control microphones and toward the ears are considered. This approach is referred to as virtual sensing [79]. Based on the pressures measured at the control microphones, the pressures at the ear microphones are then estimated. The control microphones, which are used in the operation of the control system, are commonly referred to as the *physical sensors*, or *physical microphones*. The locations at which the pressures are to be estimated are referred to as *virtual microphones*, or *virtual locations*.

The first virtual sensing approach considered here is the virtual microphone arrangement [36]. This virtual sensing technique is simple to implement and has been used in several other studies related to active headrests [35, 48]. The remote microphone technique [77], which can be viewed as an extension of the virtual microphone arrangement, is then considered.

In any control system employing virtual sensors, the control signals are adjusted to cancel the vector of error signals at the virtual locations. Using subscript v to denote signals at the virtual locations, the vector of virtual error signals is given by

$$\mathbf{e}_v(e^{j\omega t}) = \mathbf{d}_v(e^{j\omega t}) + \mathbf{G}_v(e^{j\omega t})\mathbf{u}(e^{j\omega t}). \tag{4.5}$$

Here, the transfer function matrix $\mathbf{G}_v(e^{j\omega t})$ represents the input-output relationship from the loudspeakers to the virtual microphones, as can be seen in Figure 4.8b-4.8c. It is therefore necessary to perform an additional system identification task with microphones temporarily located at the virtual locations. These microphones would then be removed during operation of the control system. The following sections describe how to estimate the virtual error and disturbance signals according to the virtual microphone arrangement and the remote microphone technique.

4.3.1 Virtual microphone arrangement

An illustration of the transfer paths used in the virtual microphone arrangement is shown in Figure 4.8b. In the virtual microphone arrangement [36], the pressure due to the primary sound field is assumed equal at the physical and virtual locations, *i.e.*, $\hat{\mathbf{d}}_v(e^{j\omega t}) \approx \mathbf{d}_p(e^{j\omega t})$. This is usually a valid assumption when the distance between the physical and virtual sensors is small compared with the wavelength of the primary disturbance.

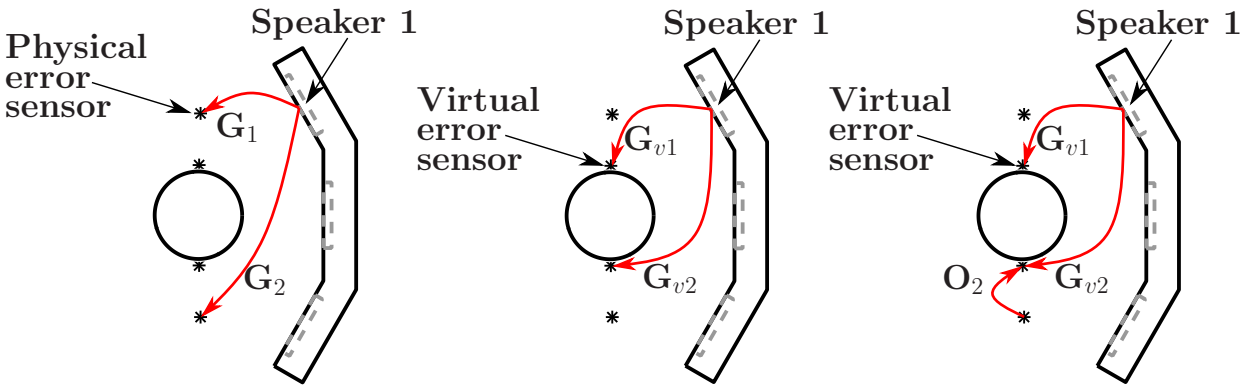

(a) Traditional ANC (b) Virtual microphone (c) Remote microphone

Figure 4.8: Definitions of transfer paths used in the computation of the control inputs for each sensing approach.

The vector of control inputs is formed using the same approach as above. This results in the vector of control inputs

$$\mathbf{u}_{opt}(e^{j\omega t}) = -\mathbf{G}_v^H(e^{j\omega t})\left[\mathbf{G}_v(e^{j\omega t})\mathbf{G}_v^H(e^{j\omega t})\right]^{-1}\mathbf{d}_p(e^{j\omega t}). \tag{4.6}$$

If the physical and virtual microphones are located at the same point in space, Equation 4.6 reduces to the case of canceling the pressure at physical error sensors.

4.3.2 Remote microphone technique

In the remote microphone technique [77], the disturbance signals at the virtual microphones $\mathbf{d}_v(e^{j\omega t})$ are estimated by filtering the physical disturbance signals by an observation filter $\mathbf{O}(e^{j\omega t})$. This can be seen in Figure 4.8c by the additional path between the physical and virtual error sensor. An estimate of the virtual disturbance signals is thus obtained by

$$\hat{\mathbf{d}}_v(e^{j\omega t}) = \mathbf{O}(e^{j\omega t})\mathbf{d}_p(e^{j\omega t}). \tag{4.7}$$

The physical disturbance signals $\mathbf{d}_p(e^{j\omega t})$ can be computed by subtracting the contribution of the control inputs from the physical error signals. The least squares solution for the observation filter can be computed by first forming the virtual estimation error,

$$\begin{aligned}\boldsymbol{\xi} &= \hat{\mathbf{d}}_v(e^{j\omega t}) - \mathbf{d}_v(e^{j\omega t}) \\ &= \mathbf{O}(e^{j\omega t})\mathbf{d}_p(e^{j\omega t}) - \mathbf{d}_v(e^{j\omega t}).\end{aligned} \tag{4.8}$$

The observation filter is then obtained by minimizing the expectation of the 2-norm of the estimation error,

$$E\left[\boldsymbol{\xi}^H\boldsymbol{\xi}\right], \tag{4.9}$$

which results in the solution [110]

$$\mathbf{O}_{opt}(e^{j\omega t}) = \mathbf{S}_{pv}(e^{j\omega t})\mathbf{S}_{pp}^{-1}(e^{j\omega t}). \tag{4.10}$$

Here, $\mathbf{S}_{pv} = E\left[\mathbf{d}_v\mathbf{d}_p^H\right]$ is the cross spectral density matrix between the physical and virtual primary disturbance signals and $\mathbf{S}_{pp} = E\left[\mathbf{d}_p\mathbf{d}_p^H\right]$ is the power spectral density matrix of the physical disturbance signals.

The vector of control inputs that minimizes the virtual error signals can then be computed by minimizing the squared modulus of the control effort $\mathbf{u}^H\mathbf{u}$ while simultaneously constraining the *virtual* error vector to be equal to zero. Making use of Equation (4.7), the vector of virtual error signals is estimated as

$$\hat{\mathbf{e}}_v(e^{j\omega t}) = \mathbf{O}(e^{j\omega t})\mathbf{d}_p(e^{j\omega t}) + \mathbf{G}_v(e^{j\omega t})\mathbf{u}(e^{j\omega t}). \tag{4.11}$$

The resulting vector of control inputs is thus given by

$$\begin{aligned}\mathbf{u}_{opt}(e^{j\omega t}) &= -\mathbf{G}_v^H(e^{j\omega t})\left[\mathbf{G}_v(e^{j\omega t})\mathbf{G}_v^H(e^{j\omega t})\right]^{-1}\hat{\mathbf{d}}_v(e^{j\omega t}) \\ &= -\mathbf{G}_v^H(e^{j\omega t})\left[\mathbf{G}_v(e^{j\omega t})\mathbf{G}_v^H(e^{j\omega t})\right]^{-1}\left[\mathbf{O}(e^{j\omega t})\mathbf{d}_p(e^{j\omega t})\right].\end{aligned} \tag{4.12}$$

If the observation filter gives a perfect estimate of the virtual disturbance signal, such that $\hat{\mathbf{d}}_v(e^{j\omega t}) = \mathbf{d}_v(e^{j\omega t})$, this choice of control input is equivalent to canceling the pressures directly measured at the virtual locations, provided the transfer function matrices are accurate [79]. For this reason, the maximum achievable attenuation using the remote microphone technique is infinite for any frequency, provided the primary sound field is tonal and predictable.

4.3.3 Virtual sensing performance in a plane wave primary field

In this section, the performance of the virtual microphone arrangement is compared to that of the remote microphone technique for primary sound fields consisting of a single plane wave. Up to this point, it has been assumed that the transfer functions are known exactly. If in the remote microphone technique it is further assumed that the observation matrix is known exactly, a perfect estimate of the virtual pressure can be obtained and the control system will completely cancel the pressure at the virtual microphones.

To compare the performance of the virtual microphone arrangement and the remote microphone technique, the spatial extent of the quiet zones have been computed for a set of frequencies and forward head positions. Shown in Figures 4.9-4.10 are the regions in which the primary sound field has been attenuated by 10 and 20 dB for frequencies of 300 Hz, 500 Hz, and 700 Hz. In each figure, the top row corresponds to the virtual microphone arrangement and the bottom corresponds to the remote microphone technique. In Figure 4.9, the head is in the nominal configuration, while in Figure 4.10, the head is moved 2 inches forward. For both cases, the

transfer function matrix used to compute the control inputs was identified with the head in the nominal configuration. It is important to compute the local acoustic field for head positions other than the nominal position, rather than probing the pressure in a static control volume surrounding the head and using these measurements to predict the attenuation at other locations. By moving the head to various positions, the variations in the plant are being accounted for and hence the noise reduction predictions will be more accurate as compared to neglecting these plant variations by simply probing the pressure at locations around the head.

With the head in the nominal position, the remote microphone technique is capable of forming a 20 dB quiet zone at the ear for every frequency. At frequencies below about 500 Hz, there is little difference in the quiet zones generated using the virtual microphone arrangement and the remote microphone technique. At these frequencies, the wavelengths are large enough such that the assumption of equal primary pressure at the physical and virtual locations is valid. Also for frequencies lower than about 500 Hz, $ka << 1$, where k is the wavenumber and a is the radius of the secondary sources, implying that the secondary sources are radiating uniformly and creating quiet zones of similar shape and size regardless of the virtual sensing approach used. At higher frequencies, the directivity of the secondary sources becomes more pronounced and leads to differences in the spatial extent of the quiet zones achieved using the two methods, as can be seen in Figure 4.9. The assumption of equal primary pressure at the physical and virtual locations, as made in the virtual microphone arrangement, also becomes less valid as the wavelengths decrease at higher frequencies.

When the head is shifted forward, as shown in Figure 4.10, the quiet zones formed using the virtual microphone arrangement remain comparable to those formed using the remote microphone technique for frequencies below 500 Hz. However, at higher frequencies it is apparent that the observation filter used in the remote microphone technique helps to more accurately estimate the virtual pressure and thus shift the quiet zone towards the ears. When the head is moved from its nominal configuration, two factors contribute to the degradation of the quiet zone. First, the transfer function matrix used to compute the control inputs is now incorrect. Secondly, the desired cancellation points are no longer located at the virtual locations. Moving virtual sensing algorithms have been proposed for the second problem, although they require some form of a real-time head tracking system [79]. For a more comprehensive summary of the performance of the active headrest in a plane wave primary field, the reader is referred to Appendix B.

At this point it should be mentioned that the acoustic performance (shape of quiet zone and attenuation levels) is fairly sensitive to the geometry of the headrest and the primary sound field. It was found that the performance generally improved by setting the angles of the side speakers such that they were directly facing the ears. Results corresponding to this geometric configuration can be found in Appendix B. The reason for this improvement in performance stems from how quiet zones are generated in the presence of reflecting/diffracting surfaces. The on-axis cancellation performance of a baffled piston source is generally superior to the off-axis performance [108], and is further improved by the presence of reflecting surfaces near the cancellation point [17]. Some physical understanding of the acoustic behavior can be gained by

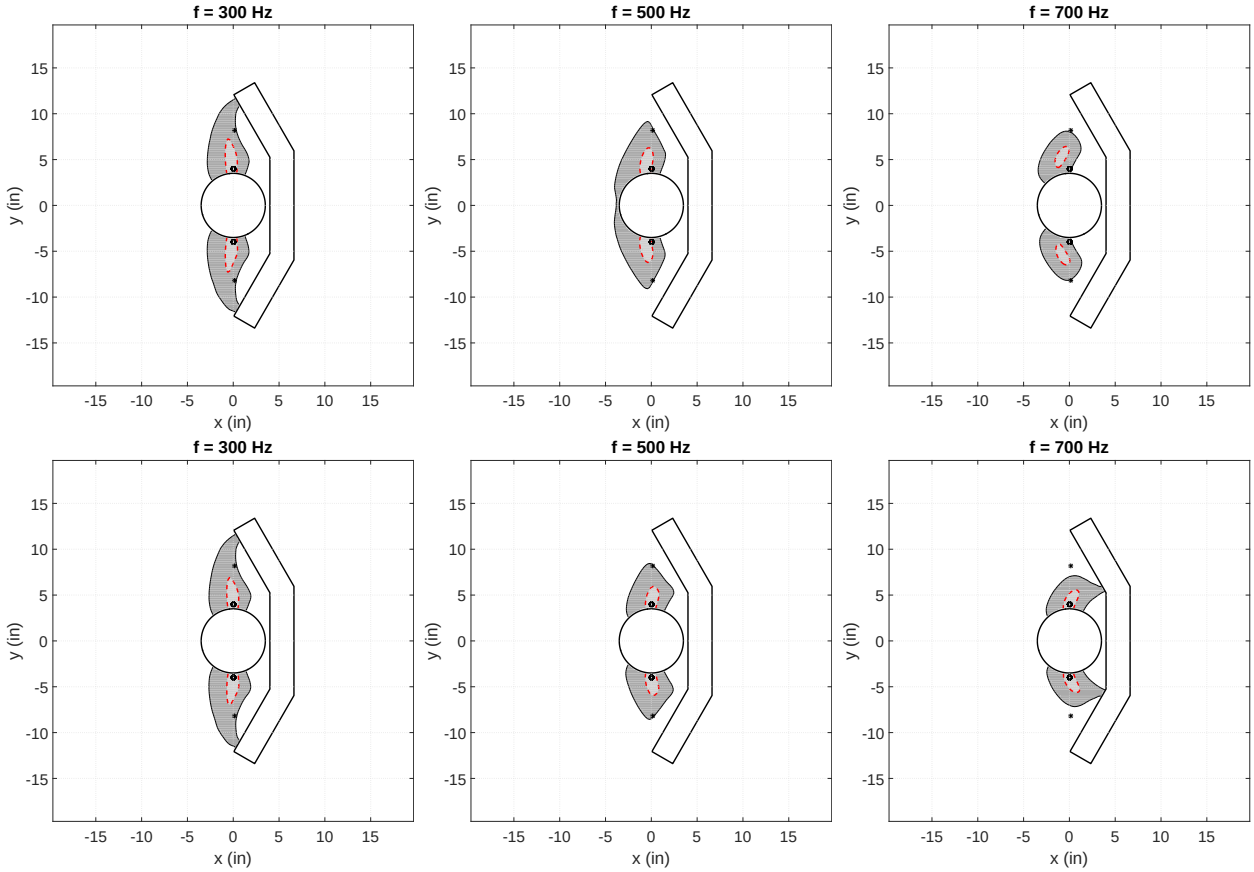

Figure 4.9: 10 dB (dark gray) and 20 dB (light gray) quiet zones for the virtual microphone arrangement (first row) and the remote microphone technique (second row) with the head in the nominal position for a plane wave primary field.

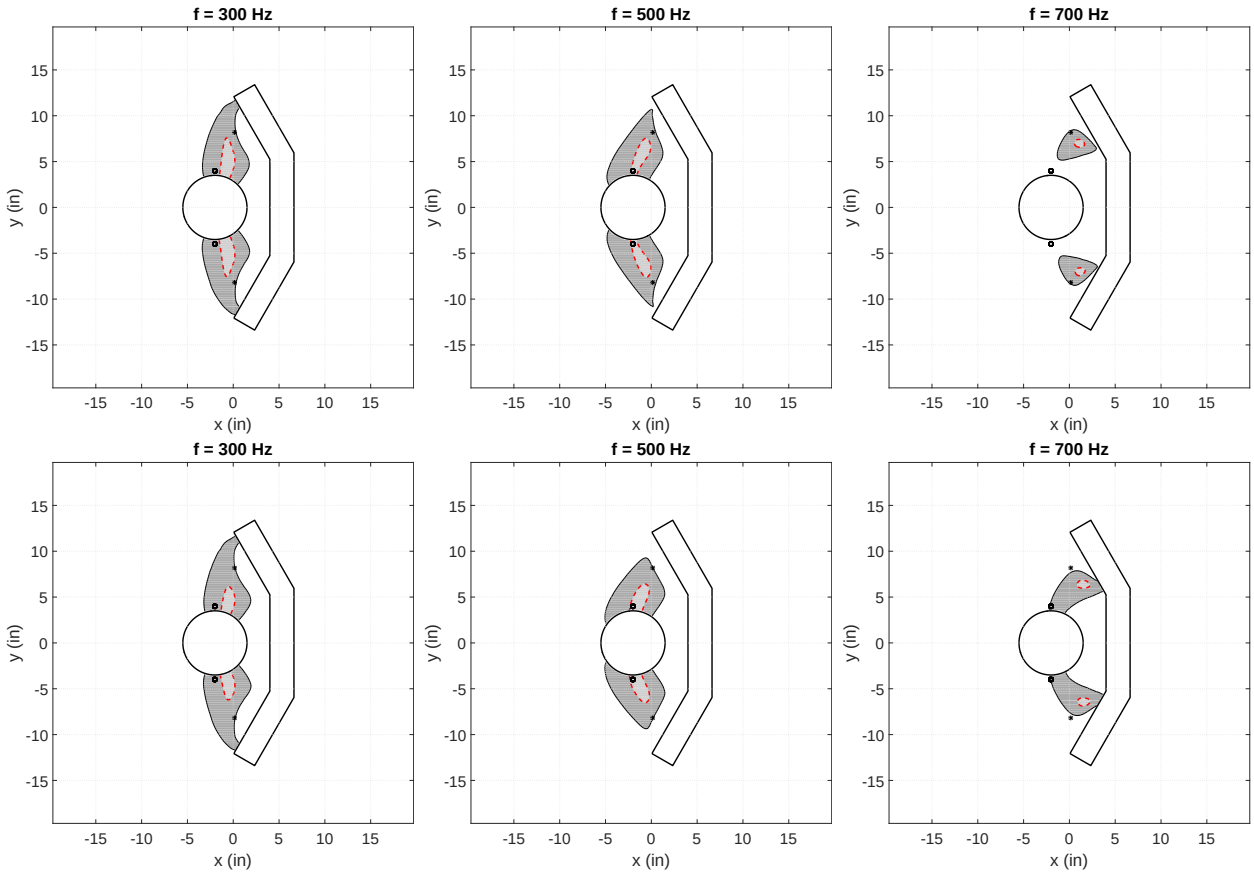

Figure 4.10: 10 dB (dark gray) and 20 dB (light gray) quiet zones for the virtual microphone arrangement (first row) and the remote microphone technique (second row) with the head shifted 2" forward for a plane wave primary field.

visualizing the quiet zones for various frequencies and head positions. It can be seen in Figures 4.9-4.10 that the head has a spreading effect on the quiet zone. This is attributed to the zero pressure gradient condition that the head imposes on the local sound field, resulting in a larger quiet zone [17].

4.4 Effects of a diffuse sound field

It has been demonstrated that by using virtual sensors, the location of the quiet zones can be shifted away from the control microphones and to the virtual locations. In this section, the acoustic performance in diffuse sound fields will be considered. In a diffuse field, the pressure is spatially random, with an equal probability of acoustic energy arriving from any direction [109]. Although the concept of a diffuse field is a mathematical idealization, it is representative of practical scenarios in which multiple uncorrelated noise sources are present. For instance, the sound field inside a lightly damped enclosure, such as the crew module described at the beginning of this Chapter, will likely be highly complex, and perhaps more easily described by a diffuse field rather than by a modal response.

For the plane wave primary field described in Section 4.1, the sound field was completely predictable and well-behaved. The control microphones were also located at the same x positions such that the primary disturbance at the control and ear microphones were very similar at low frequencies (they were not, however, identical because of the diffraction pattern around the headrest). In a diffuse sound field, this is not the case. Random phase shifts due to the spatial characteristics of the sound field result in an unpredictable and thus more difficult to control primary field. The acoustic performance predicted in a diffuse sound field will likely lead to results that may be more representative of practical scenarios.

It should be emphasized that the performance of the remote microphone technique presented in the previous section assumes that the virtual pressure is known with complete accuracy. Even with the virtual pressure known exactly, the resulting quiet zones were very similar to those generated using the virtual microphone arrangement for low frequencies mainly due to the uniform radiation pattern of the secondary sources at low values of ka. Since in a diffuse field, the virtual pressure cannot be estimated with perfect accuracy, the performance benefits associated with the remote microphone technique are expected to be even less significant. To clarify, consider the implications of Equation 4.10. In a sound field consisting of a single frequency plane wave arriving at a nominal angle of incidence, S_{pv} and S_{pp} are constant values and can be used to compute the observation matrix that provides the exact virtual pressure values (Equation 4.7). In a diffuse field, however, each specific realization represents one sample of a random process. In this case, S_{pv} and S_{pp} are computed by ensemble averaging over a finite number of realizations. The matrix of observation filters given by $O = S_{pv}S_{pp}^{-1}$ hence represents a best least-squares estimate of the virtual pressure for a given realization, rather than its exact value for that particular realization. For this reason, the only virtual sensing approach that will

be considered in the diffuse field simulations is the simpler virtual microphone arrangement.

To estimate the attenuation in a diffuse sound field, it was necessary to average the results from an ensemble of realizations. For each diffuse field realization, the control system was adjusted to minimize the primary pressures at the ear microphones using the virtual microphone arrangement, *i.e.*, Equation 4.6. The number of realizations used in the average was increased until the resulting quiet zone converged to a constant size and shape. In the results below, 100 diffuse field realizations were averaged to produce the resulting quiet zones.

The spatial extent of the quiet zones in tonal diffuse sound fields have been computed for frequencies of 100 Hz, 300 Hz, 500 Hz, and 700 Hz for two cases. The first is when the control system is adjusted to cancel the pressure at the control microphones (conventional ANC). The second corresponds to minimizing the virtual signals estimated according to the virtual microphone arrangement. The quiet zones are shown in Figures 4.11-4.14 for three forward and lateral head positions. In each case, the transfer function matrix used to compute the optimal control inputs was computed with the head in the nominal position. The asymmetries in the quiet zones are present due to the finite number of realizations used to form the predictions. In Figure 4.11, the control system is adjusted to cancel the pressure at the control microphones. For the nominal head location, the 10 dB quiet zone extends to the ears at a frequency of 100 Hz. When the head is shifted forward or the frequency is increased, however, the quiet zone no longer reaches the ears. At higher frequencies, the quiet zones become smaller and localized around the points of cancellation. The same set of conditions is shown in Figure 4.12, with the difference being that now the virtual microphone arrangement is used to minimize the estimated pressure at the ears. In this case, nearly 10 dB attenuation is achieved for the nominal head position for frequencies up to 500 Hz. The quiet zone also reaches the ears for forward head positions of up to 2" for frequencies up to 300 Hz. Overall, it is clear that the shape and locations of the quiet zones are far improved by using the virtual microphone arrangement to estimate the pressure at the ears. Similar results are shown in Figures 4.13-4.14 for lateral head movements.

Differences in the spatial extent of the quiet zones in plane wave and diffuse primary fields can be ascertained by comparing the top rows of Figures 4.9-4.10 and the two left columns of Figure 4.12. Each case corresponds to minimizing the virtual pressure estimated using the virtual microphone arrangement for nominal and 2" forward head positions. Compared to the top row of Figure 4.9, it is clear that the shapes of the quiet zones in the diffuse field are significantly smaller, and that the primary pressure is not attenuated more than 20 dB at any point for frequencies above 100 Hz. It can also be seen that the quiet zones in the diffuse field are much narrower in the x direction than in the plane wave primary field. In the plane wave primary field simulations, the wave propagation directions were similar for the primary and secondary pressure fields, which results in a broadening of the quiet zone in this direction. In the diffuse field, the random phases and angles of incidence of each plane wave create arbitrary phase shifts between the physical and virtual microphones, hence this broadening behavior is not observed. In these cases, the shape of the quiet zone is mainly dictated by the radiation pattern of the loudspeakers and the diffraction pattern around the head.

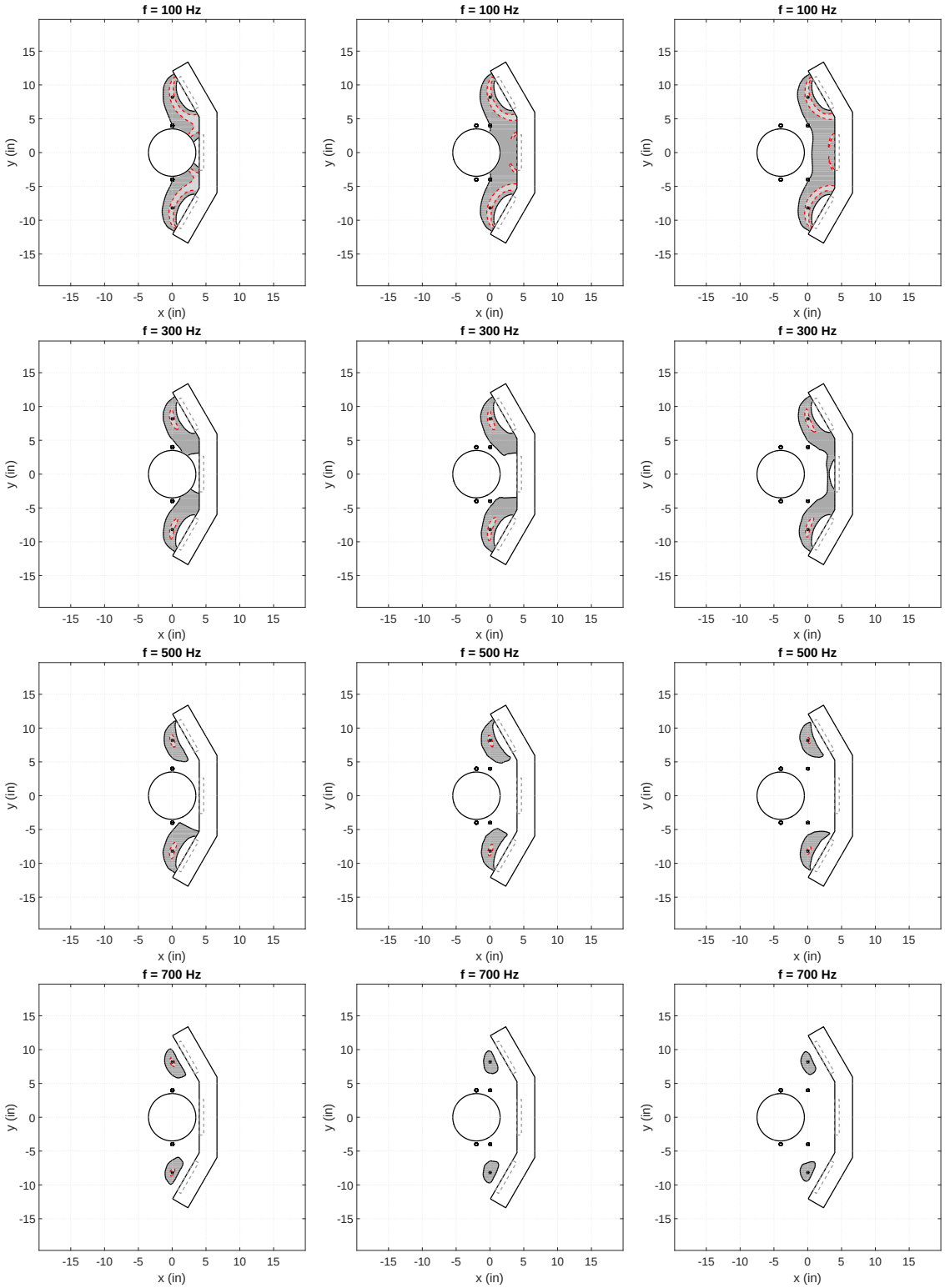

Figure 4.11: Cancellation at control microphones in a pure tone diffuse field for forward head positions of $x = 0$", 2", and 4".

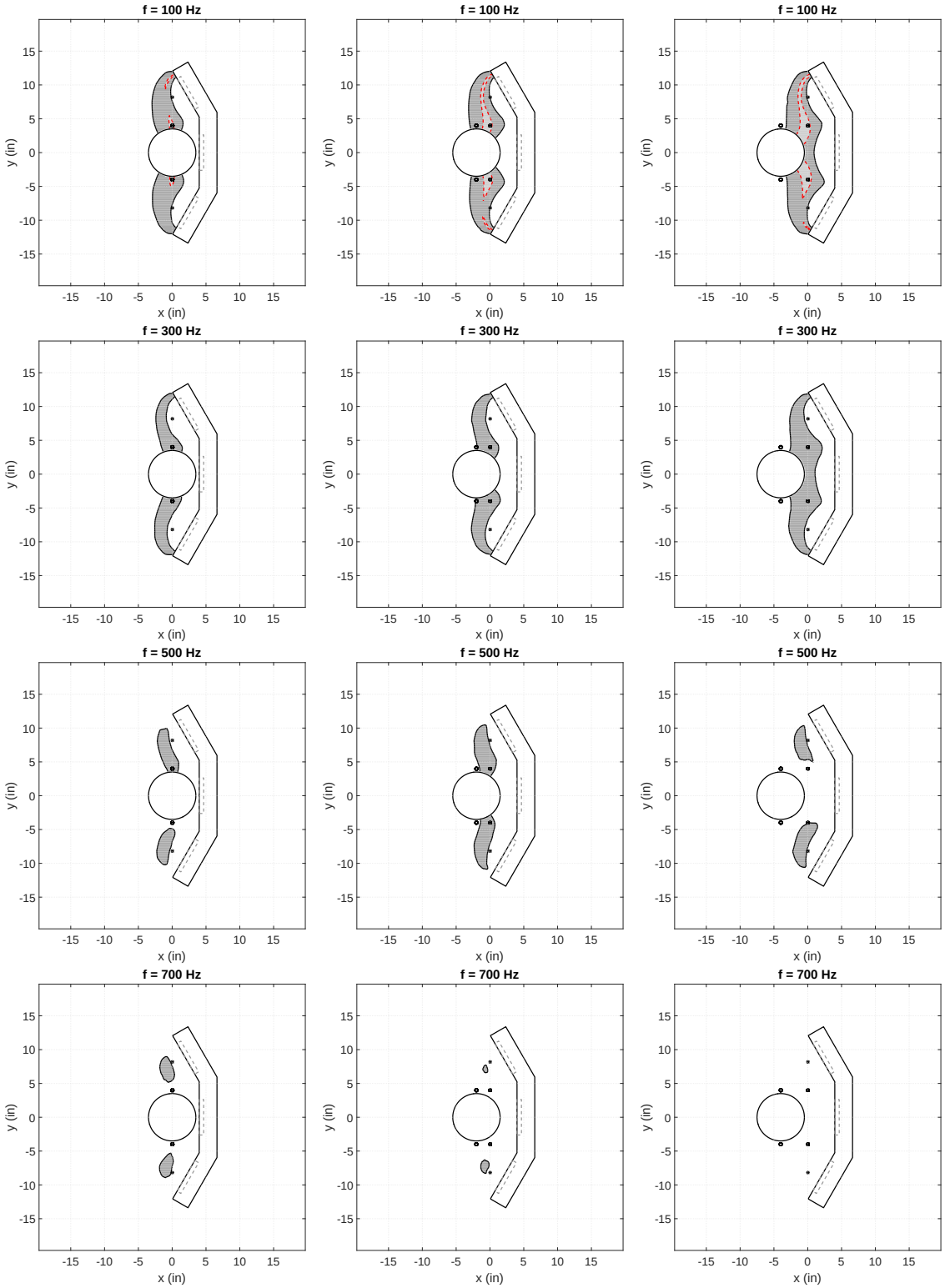

Figure 4.12: Minimizing the virtual error signals estimated according to the virtual microphone arrangement in a pure tone diffuse field for forward head positions of $x = 0$", 2", and 4".

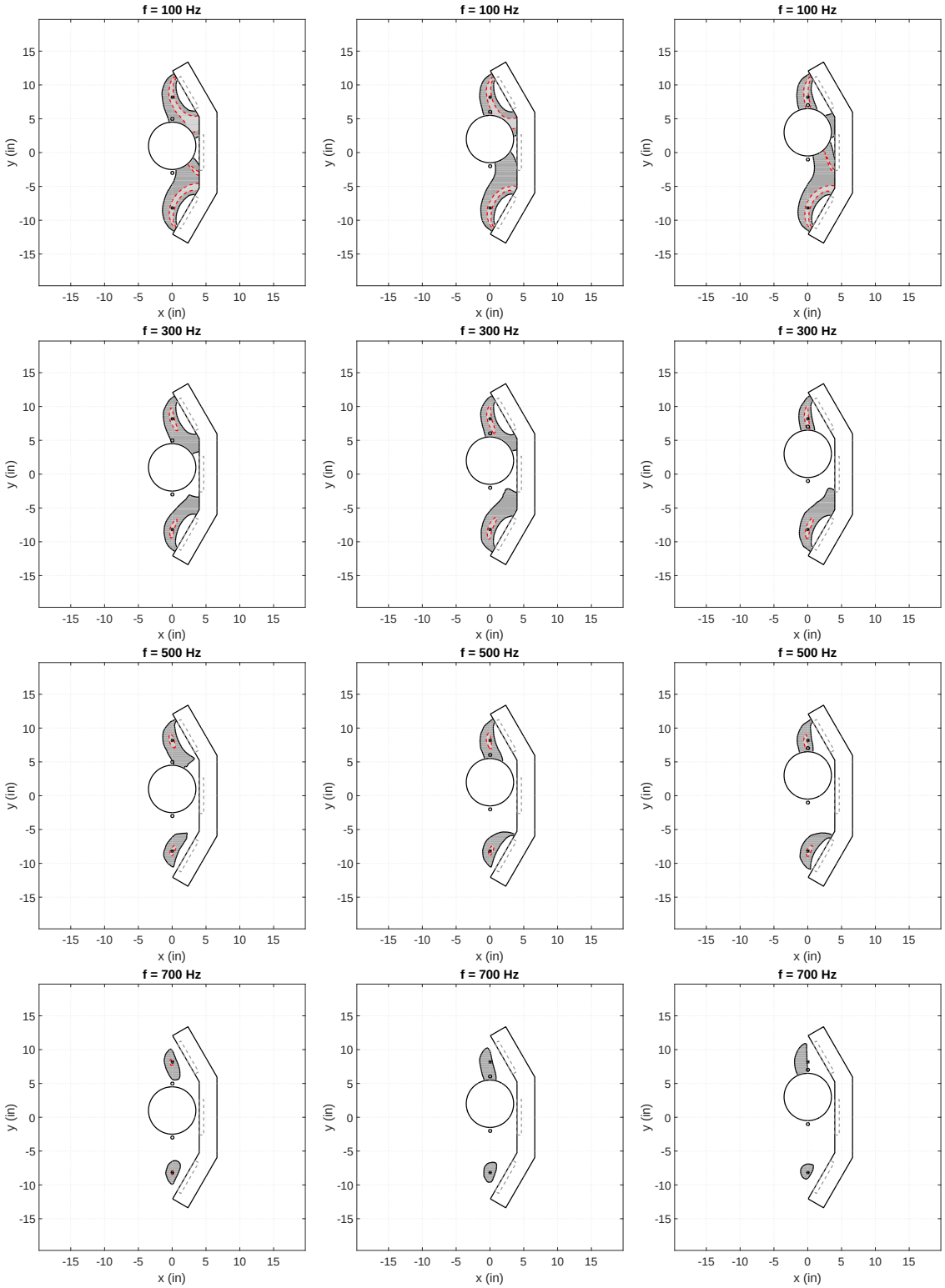

Figure 4.13: Cancellation at control microphones in a pure tone diffuse field for lateral head positions of $y = 1"$, $2"$, and $3"$.

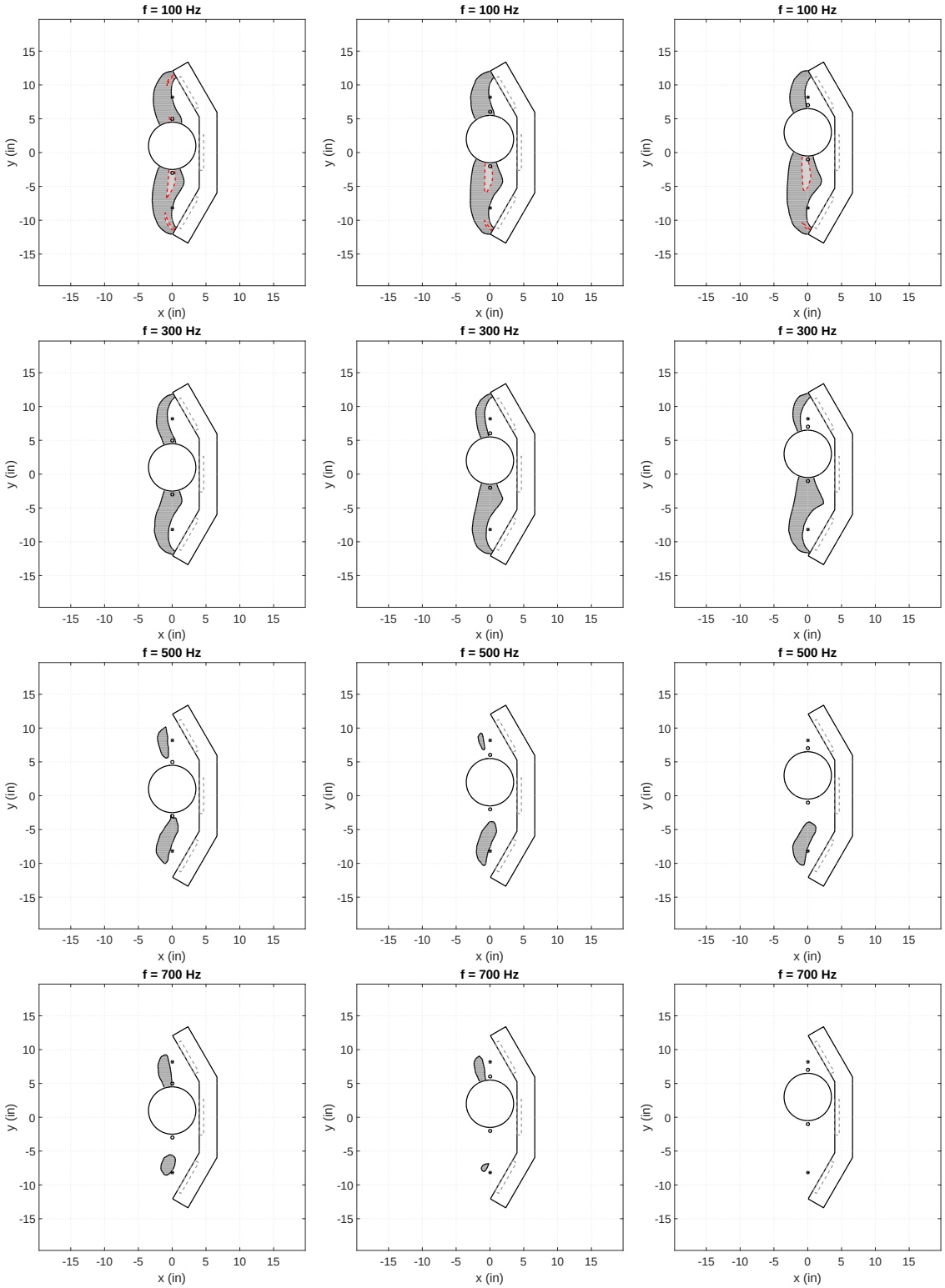

Figure 4.14: Minimizing the virtual error signals estimated according to the virtual microphone arrangement in a pure tone diffuse field for lateral head positions of $y = 1"$, $2"$, and $3"$.

4.5 Alternate headrest configurations

The acoustic performance of an active headrest is influenced by numerous factors such as the number and relative placement of the loudspeakers and microphones, the characteristics of the primary sound field, and the geometry of the baffle structure that houses the loudspeakers. This section provides some preliminary analysis of the effects that these factors have on the acoustic performance.

4.5.1 Primary sound field effects on acoustic performance

The local controlled sound field,which is the superposition of the primary and secondary sound fields, is a strong function of the primary sound field characteristics. Even for simple sound fields consisting of an individual plane wave, the size and shape of the quiet zones are dependent on the angle of incidence. Some understanding into the effects that the angle of incidence has on the acoustic performance can be gained by observing Figure 4.15. In each figure, the virtual microphone arrangement is employed to minimize the pressure at the ear microphones. When the primary sound field consists of an individual plane wave arriving from behind the head, as shown in the first figure, the local sound field around the head is dominated by the diffraction pattern around the baffle structure. If, on the other hand, the plane wave is traveling toward the head, as shown in the middle figure, the local sound field is seemingly more characterized by the superposition of the incident wave as well as the reflection off of the baffle. In the third figure, the plane wave is arriving from above/below the headrest and the effects of reflections are less pronounced. Lastly, the acoustic performance in a diffuse sound field is shown. For all primary sound fields consisting of an individual plane wave, regardless of the angle of incidence, the 20 dB zone of quiet extends to the ears. In a diffuse field, however, only a 10 dB quiet zone is formed around the ears. This is due entirely to the spatial complexity of the primary sound field and can be further understood by reconsidering Figure 4.5. The spatial variation in pressure between the physical and virtual microphones in a plane wave primary field is fairly insignificant, especially at the lower frequencies considered here, although the spatial variation in a diffuse field is much more notable.

4.5.2 Varying secondary source locations

Insight into behavior of the locally controlled sound field in an active headrest can be gained by understanding the acoustic consequences associated with canceling the pressure at a point near a reflecting/diffracting surface, such as a head. The effects of canceling the pressure at a point near a diffracting sphere was analyzed in [35] using an expansion of spherical harmonics to represent the diffracted sound field. It was shown that the presence of a diffracting surface near the cancellation point actually broadens the quiet zone and creates a similar effect to what would be observed if both the pressure and pressure gradient were canceled at a point.

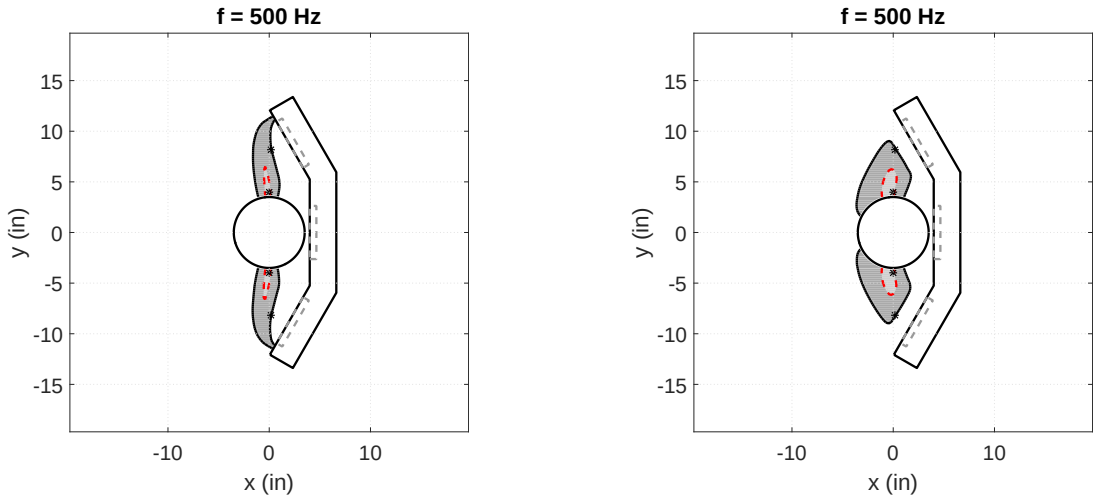

(a) Plane wave in $-x$ direction

(b) Plane wave in $+x$ direction

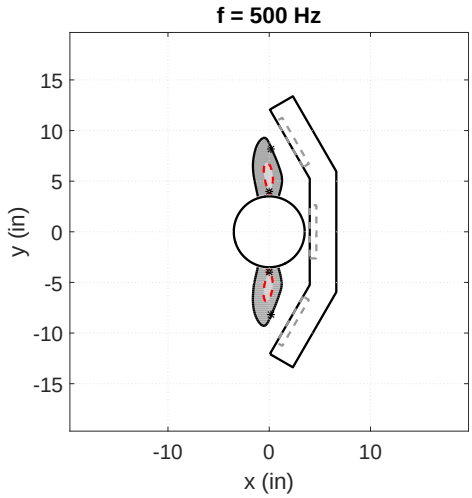

(c) Plane wave in $+z$ direction

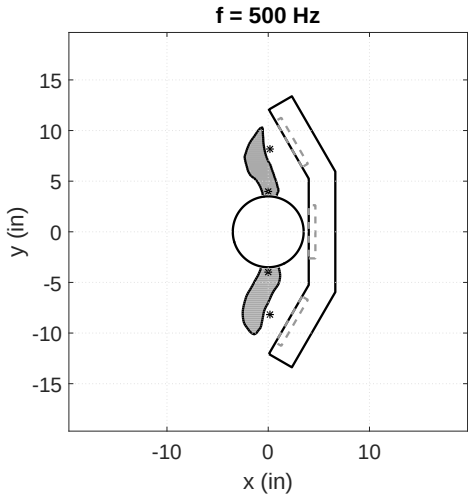

(d) Diffuse field

Figure 4.15: Influence of the primary sound field on the acoustic performance. The 10 dB and 20 dB quiet zones are shown in dark and light gray.

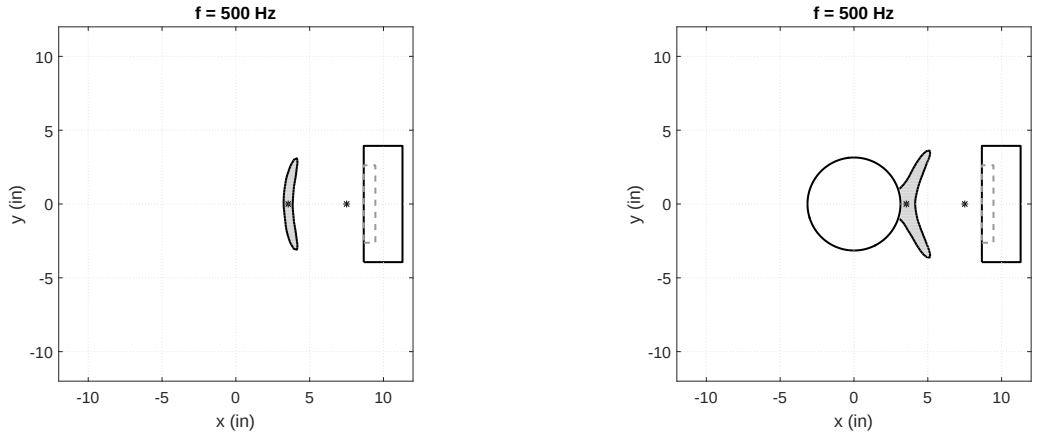

(a) Sphere not present (b) Sphere present

Figure 4.16: Effects of pressure cancellation near a diffracting surface. 20 dB quiet zones shown in gray.

The spreading effect that the rigid sphere has on the quiet zone can be seen in Figure 4.16. The span of the quiet zone along the speaker axis (x-direction) is nearly doubled when the sphere is included in the model. This is due to the fact that a zero pressure gradient condition is imposed at the surface of the sphere, leading to an increase in the spatial extent of the quiet zone [15]. In both cases, the pressure at the microphone nearest the sphere is canceled exactly.

The locations of the secondary sources relative to the cancellation points also influence the acoustic performance. To demonstrate, a simple model consisting of a single secondary source, modeled as a baffled piston, and a rigid sphere was constructed. The influence that the relative angle of the secondary source has on the resulting quiet zone can be inferred from Figure 4.17. It is clear that the spatial extent of the quiet zone is largest when the axis of symmetry of the secondary source coincides with both the cancellation point as well as the center of the rigid sphere. To visualize this effect in an active headrest like the one considered in previous sections, a second simulation was constructed that analyzes the effects of headrest geometry on the resulting quiet zones. The resulting quiet zones are shown in Figure 4.18 and correspond to the case where the head is in the nominal position. As the relative angle between the axes of symmetry of the secondary source and the center of the sphere approaches zero, the spatial extent of the quiet zone is increased for forward and lateral head movements. In each case, the primary sound field consists of a single plane wave traveling in the $-x$ direction. These results are presented in greater detail in Appendix B.

4.5.3 Varying the number of secondary sources/sensors

It has been shown that the addition of a third loudspeaker results in a broadening of the quiet zone as well as improved attenuation. A natural question that arises is whether or not the in-

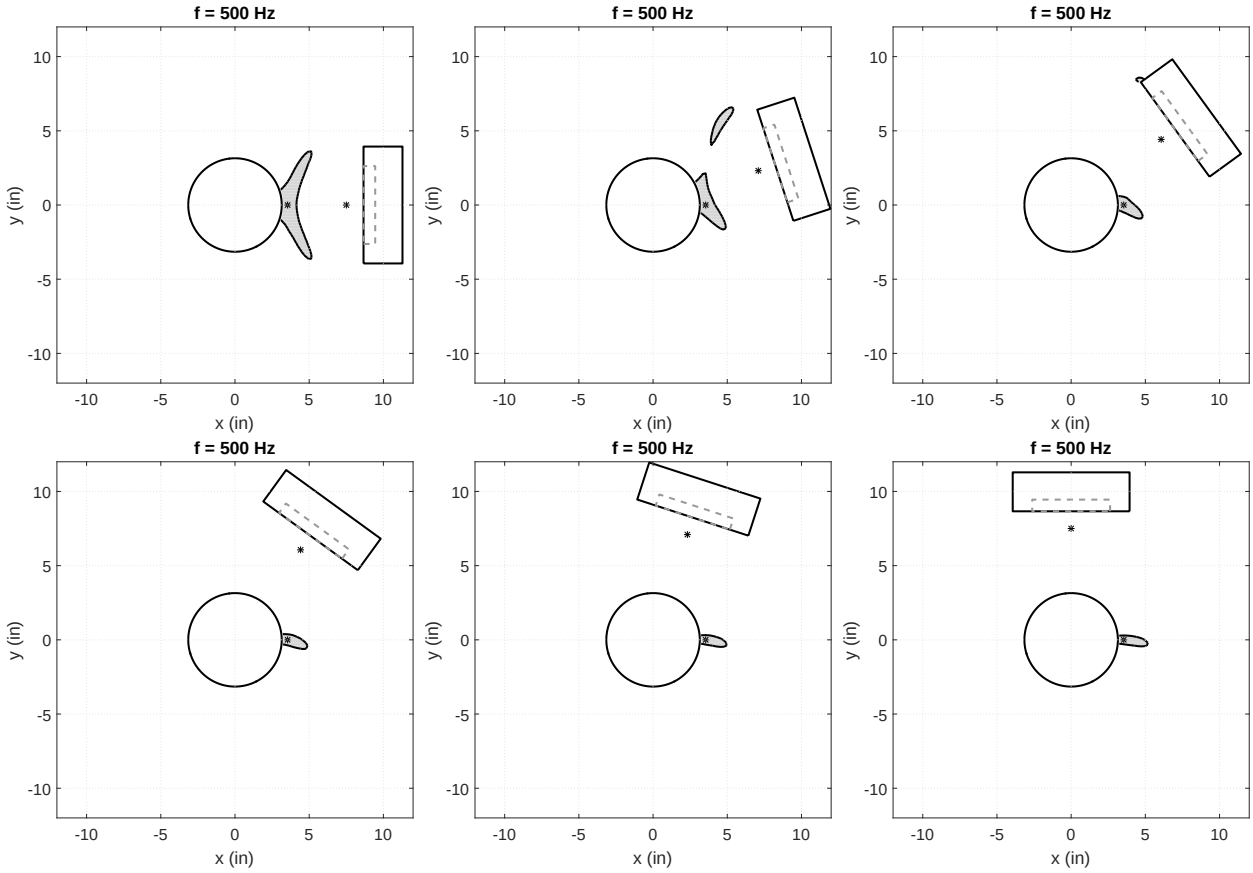

Figure 4.17: Effects of secondary source placement. 20 dB quiet zones shown in gray.

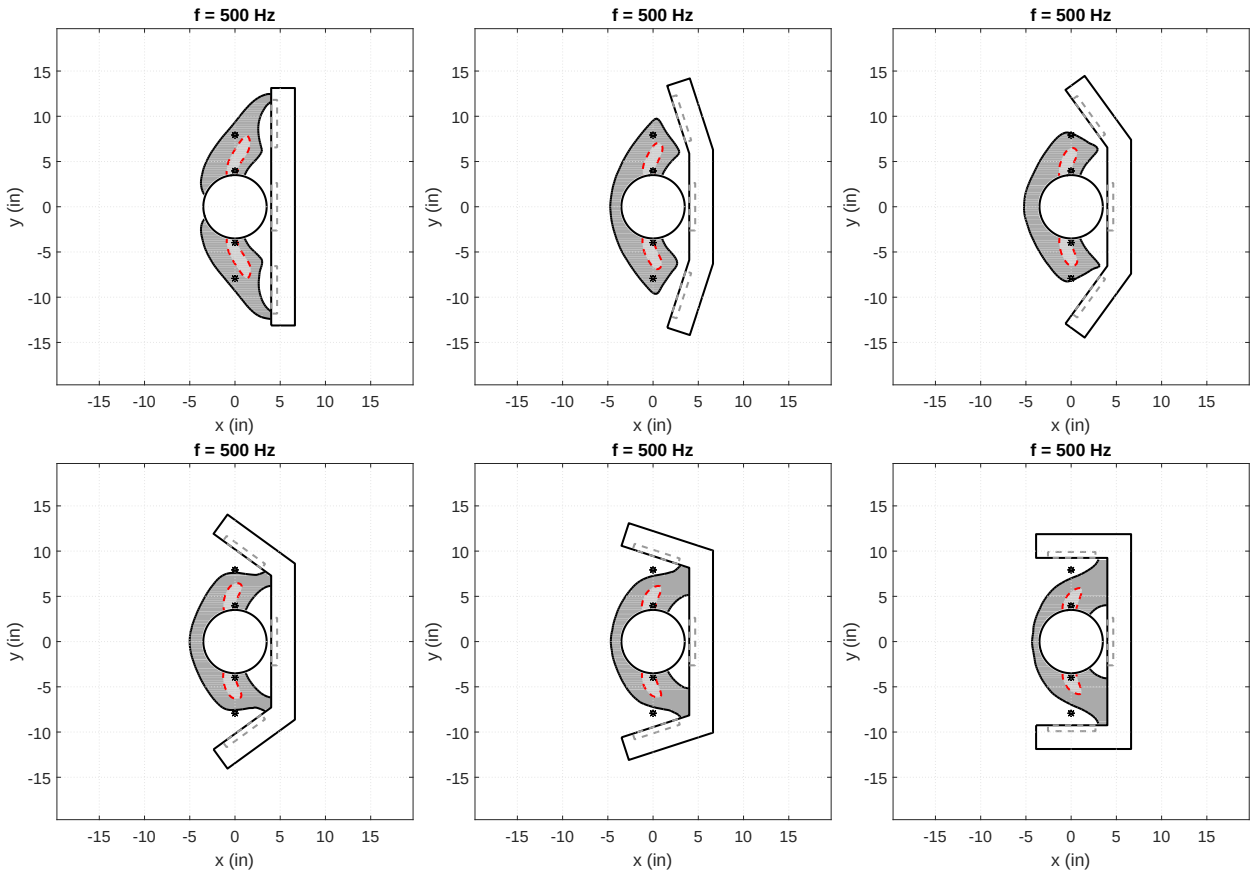

Figure 4.18: Effects of secondary source placement. 10 dB (dark gray) and 20 dB (light gray) quiet zones shown in gray.

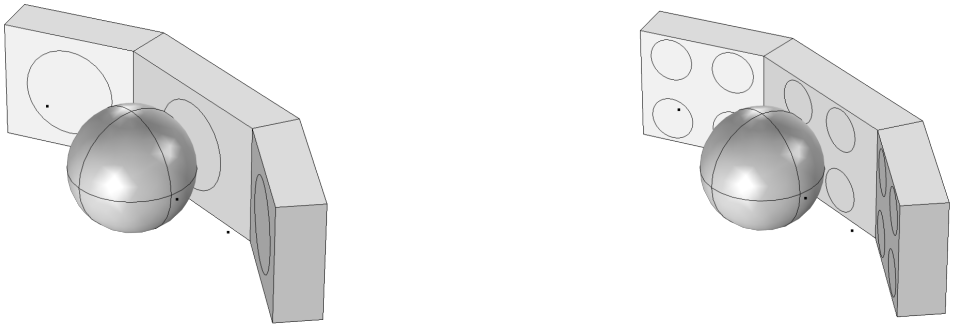

(a) Three secondary sources

(b) Twelve secondary sources

Figure 4.19: FE models of an active headrest with various secondary source configurations.

clusion of additional secondary sources can further improve the acoustic performance. In this section, a headrest using twelve secondary sources, as opposed to three, is considered in an attempt to further broaden the spatial extent of the quiet zone. A finite element model of the twelve-speaker headrest is shown in Figure 4.19 alongside the three-speaker model analyzed in previous sections. The form factors for both headrests are identical as to perform a fair comparison, although the size of the secondary sources in the twelve-input headrest was decreased as to comply with geometric constraints.

For a simple plane wave primary field at 500 Hz, the acoustic performance has been computed for both three and twelve loudspeaker configurations and is shown in Figure 4.20. In both cases, the virtual microphone arrangement is used to estimate the pressure at the ear microphones. It is apparent that the additional loudspeakers do little to improve the acoustic performance of the active headrest. Although the secondary source configuration is changed, the locations of the secondary sources (*i.e.*, behind and to the side of the head) are similar. For this reason, the secondary radiation pattern is not significantly changed by adding more loudspeakers. If, for instance, the angle of the side speakers were changed or the geometry of the baffle was varied such that the secondary sources wrapped more around the head, the secondary radiation pattern would be changed and the acoustic performance could be further improved. An investigation into the effects that headrest topology has on the acoustic performance is left for a future study.

After investigating the effects of additional secondary sources on the acoustic performance, another attempt to improve the spatial extent of the quiet zone was made by increasing the number of virtual sensors used in the control system. In this approach, the control system was adjusted to minimize the pressure at an array of virtual microphones whose locations coincide with the desired region of attenuation. Various clusters of virtual microphones arranged in lines, squares, diamonds, etc., resulted in worse performance than simply using two virtual microphones located at the ears. The poor performance using arrays of virtual sensors can be

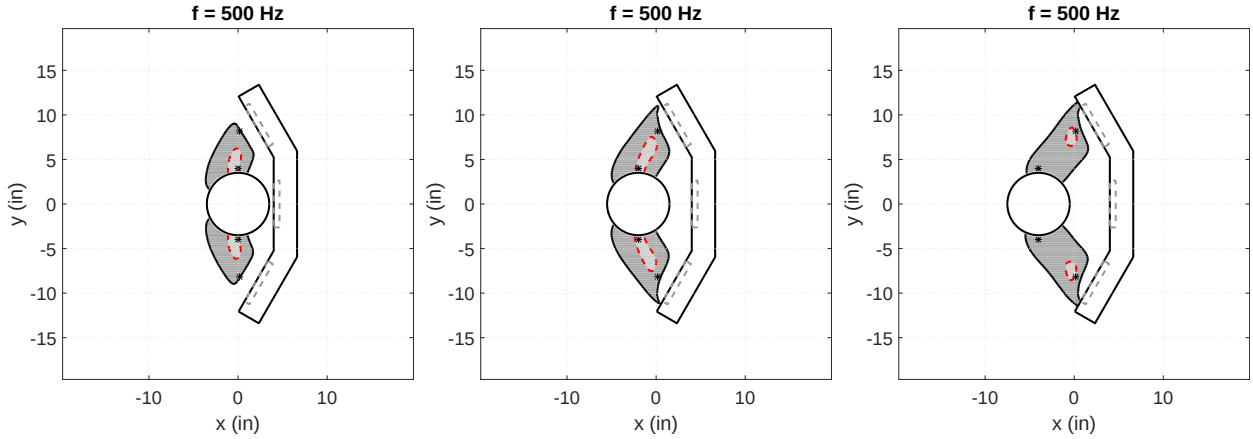

(a) Three secondary sources

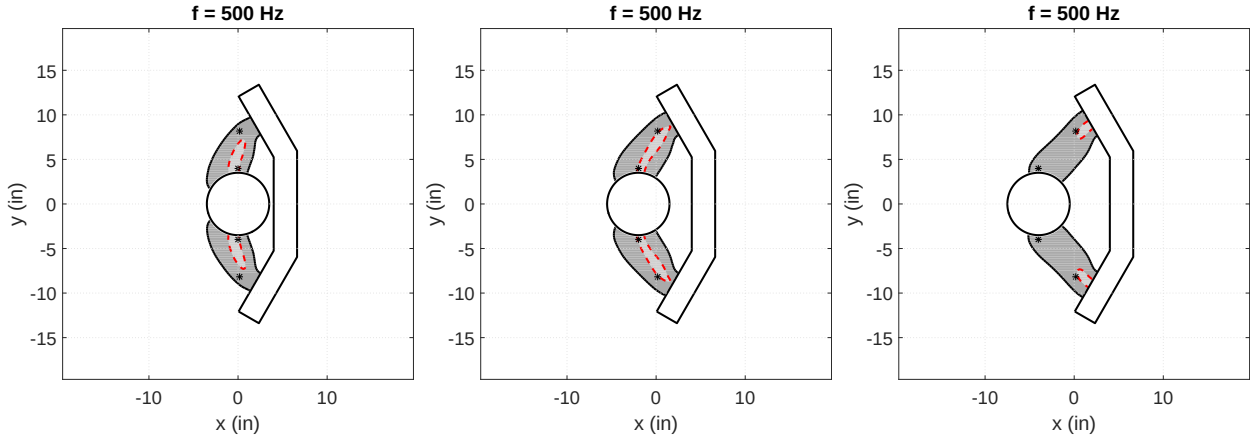

(b) Twelve secondary sources

Figure 4.20: Quiet zones for a headrest with either 3 or 12 secondary sources. 10 dB (dark gray) and 20 dB (light gray) quiet zones shown in gray.

attributed to ill-conditioning in the control system. The transfer responses from a single secondary source to each virtual microphone on either side of the head are very similar due to the close spatial proximity. This is a common problem, referred to as collinearity [33], in designing control systems with large numbers of sensors and actuators. In this case, the problem arises due to the geometric symmetry of the system.

4.6 Summary

An FEM-based numerical model of an active headrest was developed in which the geometry, the placement of microphones/loudspeakers, and primary sound field characteristics can be easily varied. For a specified geometry, it was initially shown that the addition of a third loudspeaker is beneficial in improving the attenuation as well as broadening the quiet zone. It was then shown that the attenuation can be significantly improved by using virtual sensors to shift the regions of maximum attenuation away from the control microphones and toward the ears. For the plane wave primary field in which the virtual sensing approaches were compared, it was shown that the remote microphone technique produces greater attenuation than the virtual microphone arrangement, although the spatial extent of the 10 dB quiet zone is largely similar. This is mainly due to the fact that the secondary sources radiate uniformly at low frequencies.

To evaluate the performance in a more complicated primary sound field, a diffuse field was then considered. Due to the spatial randomness of the diffuse field, the attenuation as well as the spatial extent of the quiet zones were degraded compared to the case of a plane wave primary field. To account for practical listener head movement, the system was evaluated at several frequencies and forward/lateral head positions. By observing the quiet zones in each type of field, insight into the behavior of the quiet zones could be inferred. The quiet zones obtained in a diffuse field were significantly smaller and more sensitive to head movement than those obtained in a plane wave primary field.

A brief study into the effects of including additional loudspeakers and error sensors was also performed and it was found that, without varying the geometry/form-factor of the active headrest, a three loudspeaker configuration performs comparably to systems with more secondary sources. This conclusion is drawn based upon the specific geometry, actuator/sensor placement, and virtual sensing approaches considered here. Some preliminary simulations suggest that, for alternate placements of the physical error sensors and when the control system is adjusted to simply cancel the pressure at the physical sensors, the addition of more secondary sources can more significantly influence the spatial extent of the quiet zone. It was also found that minimizing the pressure over arrays of virtual sensors resulted in degraded acoustic performance due to the issue of collinearity. If virtual sensing is used in the active headrest, simply using two virtual sensors located at either ear results in the best performance. Again, a comprehensive study of the effects that error sensor placement and headrest topology has on the acoustic performance is left for a future study.

Chapter 5

Experimental Results

This chapter presents the experimental testing procedure and results for an active headrest. An active headrest consisting of three speakers and two microphones has been fabricated and fastened to an aircraft seat. In order to quantify the performance in contrasting acoustic environments, the active headrest was tested in anechoic and reverberant acoustic conditions. In this way, performance limits can be formed for opposite ends of the acoustic spectrum. A final test was performed with the headrest located in a normal room where the primary sound field can be described as semi-reverberant.

5.1 Experimental setup

5.1.1 Structural acoustics loads and transmission facility

The structural acoustics loads and transmission (SALT) facility at NASA Langley Research Center serves as a test suite for transmission loss, absorption, and qualification testing. The facility, which is depicted in Figure 5.1, is comprised of a reverberant source room and an anechoic receiving room. The 278 m^3 reverberant room is outfitted with 18 high frequency compression drivers and 4 two-way speaker boxes for low and mid frequency (<1 kHz) sound generation. The concrete walls and ceiling of the reverberant room are splayed to reduce the effect of standing waves in the room. Furthermore, the reverberant room is structurally isolated from the rest of the building to reduce the effect of structure borne noise propagating into the room. The 327 m^3 anechoic room is lined with foam wedges on the walls and ceiling and can be used to perform transmission loss measurements. Additional wedges may be situated on the floor such that the room can be used to perform acoustic measurements in a nearly anechoic environment. A data acquisition system (DAS) computer, located outside the room, is used to generate the driving signals for the sources as well as record any relevant data.

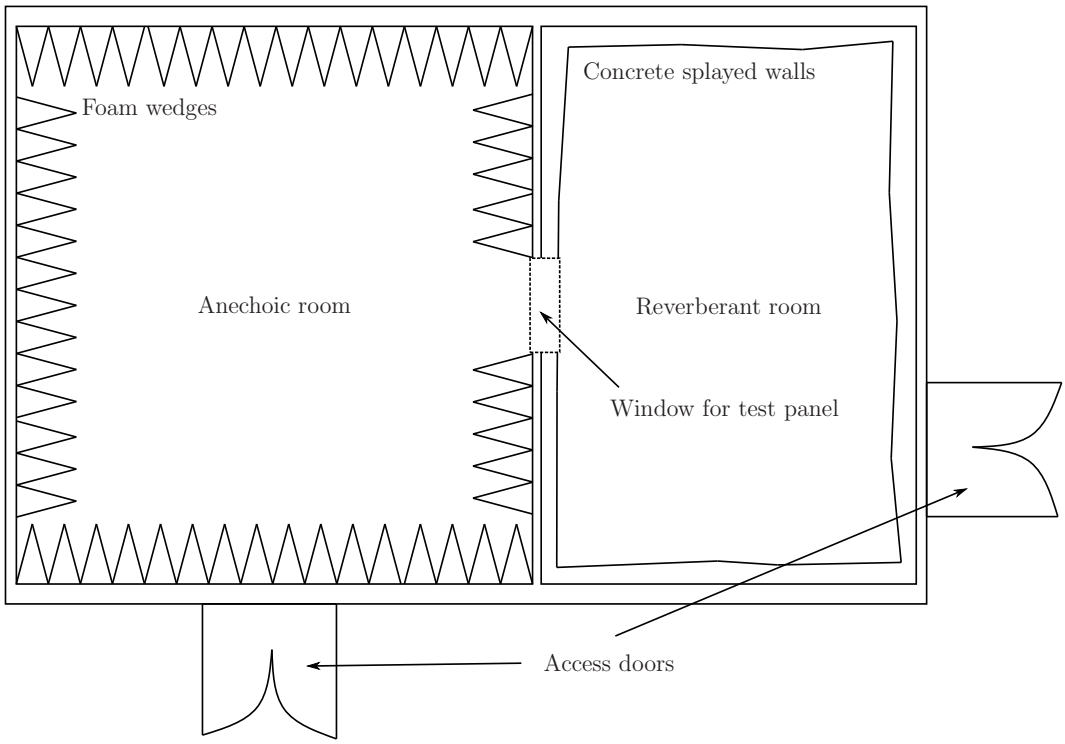

Figure 5.1: Floorplan of the structural acoustics loads and transmission facility at NASA Langley.

For the active headrest tests, it was only necessary for the performance of the headrest to be tested in reverberant and anechoic conditions. Completion of these tests hence did not involve utilizing many of the capabilities of the SALT facility. For a thorough discussion on the capabilities and characterization of the facility, the reader is referred to [111, 112].

5.1.2 Active headrest configuration

The active headrest used in the experiments is shown in Figures 5.2-5.3. The headrest was constructed using plywood and fastened to an aircraft seat. As it was shown in the previous chapter that the addition of a third loudspeaker improves the acoustic performance of an active headrest, three JBL 5.25" loudspeakers are housed in the structure and serve as the control sources. Microphones located at the ears of a manikin head are used to monitor the performance of the control system. In order to quantify the noise canceling performance of the system for various head positions, a mechanical positioning system, shown in Figure 5.4, was fabricated using 80/20 T-slotted aluminum framing and a linear stage. With this positioning system, the head could be accurately situated anywhere within a range of 3.5 inches ($\approx$ 11.5 cm) both laterally and in the forward direction. A schematic showing relevant dimensions in the headrest is shown in Figure 5.5. The control microphones, which are shown in the figure, are located a certain distance, d_1, behind each ear and a distance, d_2, horizontally away from each ear. The

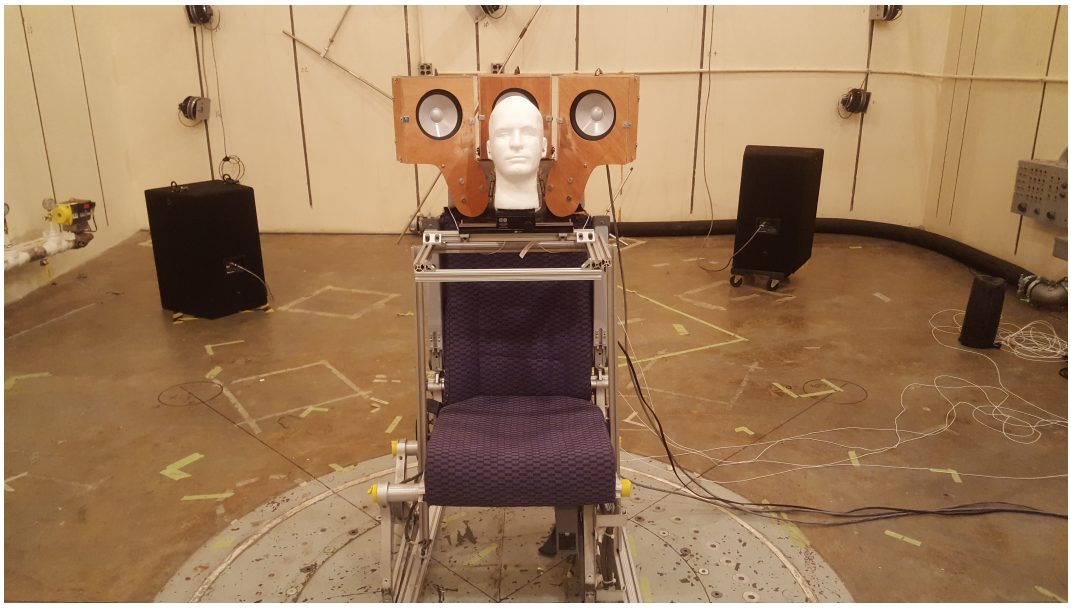

Figure 5.2: The active headrest in a reverberant environment.

distances are chosen such that the head is free to move ± 3 inches side to side and in the forward direction without making contact with the microphones. To remain consistent with the numerical model, the side speakers were adjusted to form a 30° angle with the horizontal.

5.1.3 Real-time instrumentation

A diagram of the signal paths and all hardware used in the real-time system identification and control tasks is shown in Figure 5.6. The host PC communicates with the control system via analog I/O blocks. The system consists of 3 analog outputs for the speakers and 4 analog inputs corresponding to the microphone signals. Along with 2 error microphones, 2 additional microphones are located in the manikin ears to monitor the control performance. The sensors used in the control system are electret condenser microphones (Model TMS130A10) with a nominal sensitivity of ± 20 mV/Pa. Individual calibration factors for each microphone are used in all tests to convert the responses into Pascals. The actuators in the control system are 5.25" JBL loudspeakers. Anti-aliasing and reconstruction filters are implemented using a 16 channel PCB Piezotronics signal conditioning unit (Model 481 A), which employs an 8-pole low pass filter on each channel. Two Carver Magnetic Field Power Amplifiers (Model TFM-42) were used to amplify the loudspeaker signals.

The control system was implemented using xPC Target and Simulink Real-Time. This platform allows control systems to be modeled and deployed in real-time using Simulink blocks and MATLAB functions. The system is comprised of a host computer and a target computer. The host computer serves as an environment to build and troubleshoot the model. Analog I/O

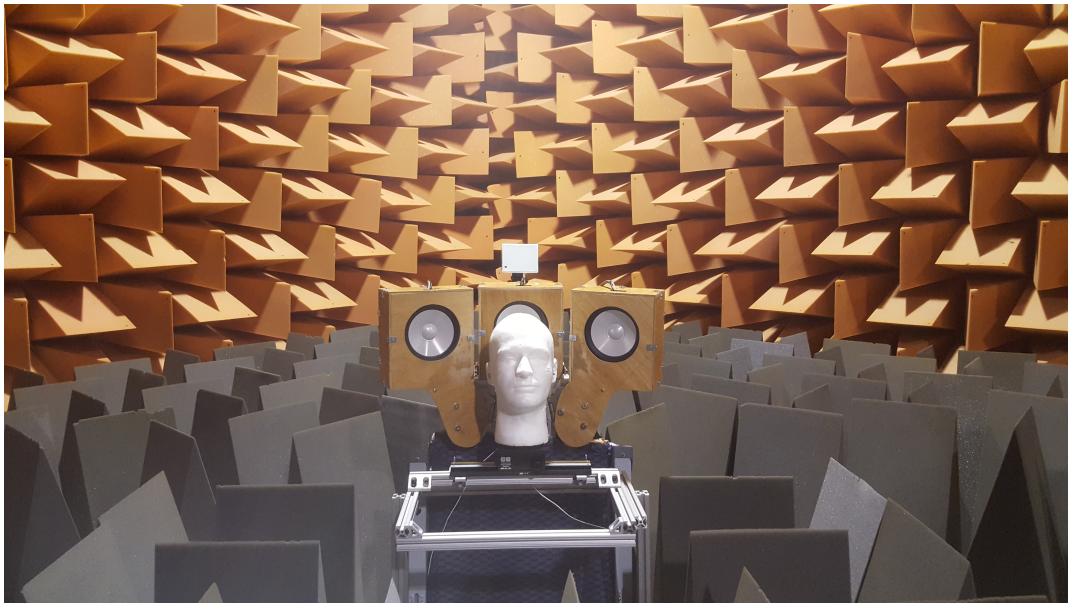

Figure 5.3: The active headrest in an anechoic environment.

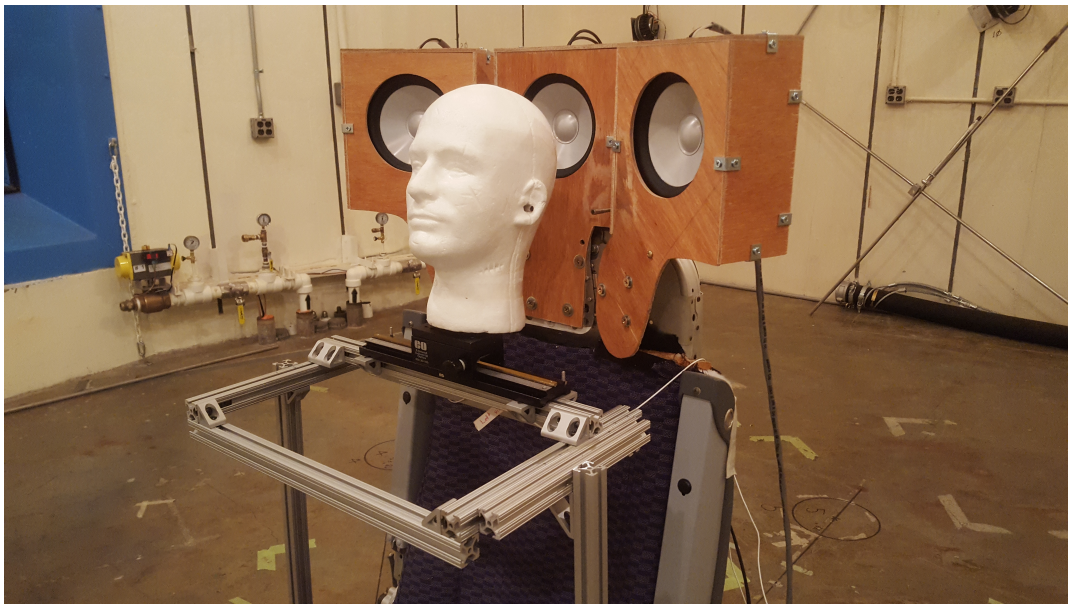

Figure 5.4: Close-up view of the active headrest. Here, the left side in-ear and control microphones as well as the mechanical positioning system can be seen.

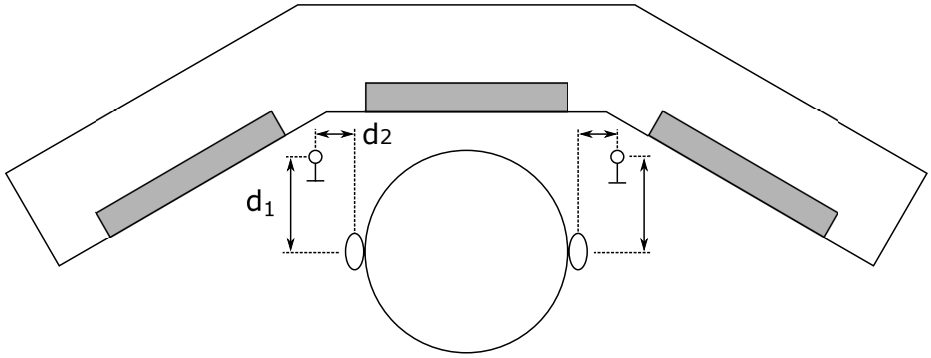

Figure 5.5: Geometry of the active headrest. The locations of the control microphones relative to the ears are given by the distances d_1 and d_2.

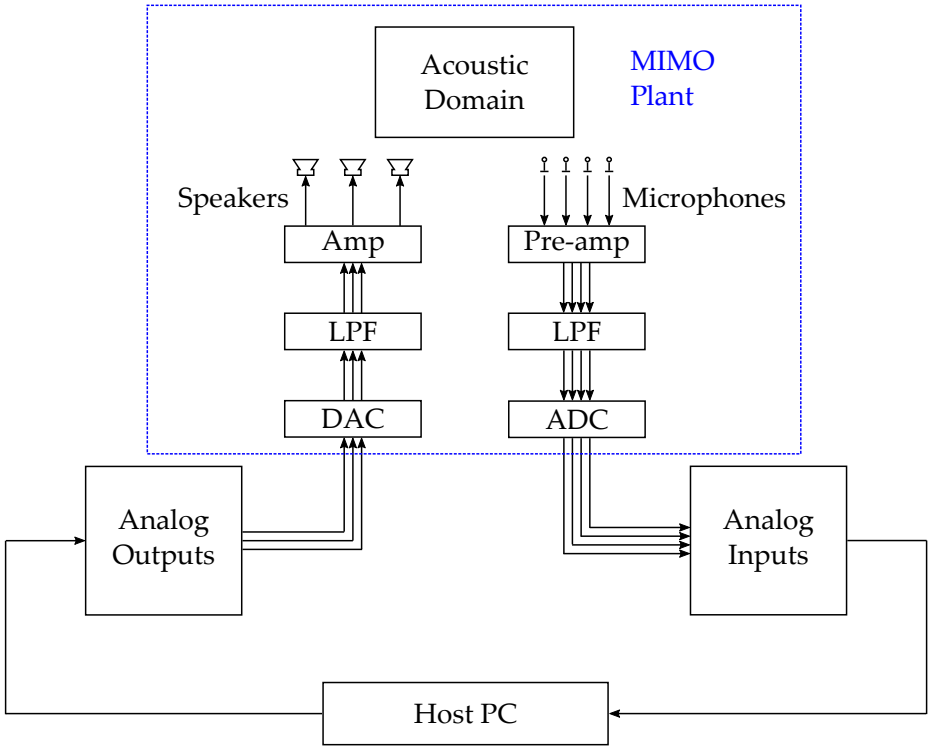

Figure 5.6: Signal diagram including all converters, low pass filters (LPF) for anti-aliasing and reconstruction, and power amplifiers. The plant consists of all hardware as well as the acoustic domain.

blocks are used in the model to communicate with the actuators and sensors when the control system is implemented in real-time. The model is compiled into C code and then downloaded onto the target machine where it can be run in real-time. The target machine, which is manufactured by Speedgoat, is interfaced with the microphones and loudspeakers using a IO104 input-output module consisting of 8 analog inputs and 4 analog outputs. The host computer, which is a personal laptop, communicates with the target machine via a local ethernet connection. The minimal achievable sample time with this target machine is reported as 8 μs, however, due to the complexity of the multichannel control systems implemented here, the minimum sample time was not achievable during execution of the control algorithm. For the results described here, all sample rates were set to 10 kHz.

5.2 System identification procedure

The plant includes the paths from each of the loudspeakers to each microphone. For an active headrest with three speakers and two physical microphones, six different paths must be modeled. If virtual sensors are incorporated into the control system, the paths from each speaker to the in-ear microphones would also need to be modeled, resulting in twelve identification tasks. Each path includes the dynamic response between the secondary speakers and the microphones. All electrical components such as A/D converters, anti-aliasing filters, D/A converters, power amplifiers, reconstruction filters, and loudspeaker and microphone responses are included in the plant. In reference to Figure 5.6, this corresponds to everything enclosed in the blue dashed box.

It is assumed that each path can be accurately modeled by a length J FIR filter such that the l-th microphone output due to the contribution of the m-th control source can be written as

$$y_{lm}(n) = \sum_{j=0}^{J-1} g_{lmj} x(n-j). \tag{5.1}$$

Here, $x(n)$ is the input signal to the m-th loudspeaker and g_{lmj} is the j-th coefficient of the FIR representing the path from the m-th loudspeaker to the l-th microphone.

The LMS algorithm [22] was used to estimate the FIR coefficients for each path. The FIR coefficients are adapted according to the update equation

$$\boldsymbol{g}_{lm}(n+1) = \boldsymbol{g}_{lm}(n) + \mu \boldsymbol{x}(n) e(n), \tag{5.2}$$

where $e(n)$ is the difference between the plant model output and the measured output. The column vector $\boldsymbol{g}_{lm}(n)$ contains the current estimate of the J FIR coefficients representing the path from the m-th loudspeaker to the l-th microphone and $\boldsymbol{x}(n)$ is given by

$$\boldsymbol{x}(n) = \begin{bmatrix} x(n) & x(n-1) & \cdots & x(n-J+1) \end{bmatrix}^T. \tag{5.3}$$

The accuracy of the identified models was verified by comparing them with the results obtained using the Wiener solution. The vector of FIR coefficients obtained using this approach is given by

$$\boldsymbol{g}_{lm,opt} = \boldsymbol{A}^{-1}\boldsymbol{b}, \tag{5.4}$$

where

$$\boldsymbol{A} = E\left[x(n)x^T(n)\right] \tag{5.5}$$

is the autocorrelation matrix of the input signal and

$$\boldsymbol{b} = E\left[x(n)y_{lm}(n)\right] \tag{5.6}$$

is the cross correlation vector between the input and output signals. It can be shown that the coefficients obtained using Equation 5.2 will converge to the optimal set under certain conditions [22]. If the input signal autocorrelation matrix is ill-conditioned, a regularization term can be included in the cost function such that the vector of FIR coefficients is given by

$$\boldsymbol{g}_{lm} = (\boldsymbol{A}^{-1} + \beta\boldsymbol{I})\boldsymbol{b}, \tag{5.7}$$

where β is a regularization factor used to improve the conditioning of the autocorrelation matrix.

For each identification task, the input was generated by passing a white noise signal through a low pass filter with a cut-off frequency of 4 kHz. Twenty seconds of the input signal and microphone responses were recorded, logged back to the host PC, and split into two 10 second long data sets. The first data set was used to identify the models using both the LMS algorithm and the Wiener solution. The second data set was used as a validation set to evaluate the accuracy of the model. The model accuracy was quantitatively assessed using the variance-accounted-for (VAF), which is given by

$$\text{VAF} = \left[1 - \frac{\text{var}\left(\boldsymbol{y} - \hat{\boldsymbol{y}}\right)}{\text{var}\left(\boldsymbol{y}\right)}\right] \times 100\%. \tag{5.8}$$

This quantity compares the measured plant output to the signal generated by filtering the input signal by the identified model. For a given path, the vector $\boldsymbol{y}$ contains the validation data set output signal and $\hat{\boldsymbol{y}}$ contains the signal obtained by filtering the input signal by the plant model. A variance-accounted-for of 100% implies that the plant model is perfect, and no uncorrelated measurement noise is present on the sensor output. The purpose of splitting the data into identification and validation data sets was to avoid the possibility of the identified model being sensitive to the specific excitation signal [84].

Finally, the frequency response for a given path is evaluated using the validation data set input-output signal spectra. The frequency response of the unknown plant can be expressed as

$$G_{xy}(f) = \frac{S_{yx}(f)}{S_{xx}(f)}, \tag{5.9}$$

where the spectra are evaluated at discrete frequencies f. The estimate of the transfer function given by Equation 5.9 is referred to as the H_1 estimator. The H_1 estimator provides an

estimate of the frequency response of the unknown transfer function, and hence does not take into account time-domain characteristics such as filter structure and causality. A simple visual comparison of the frequency response given by Equation 5.9 and the frequency response corresponding to the FIR obtained using Equation 5.2 was performed to further confirm that the identified model is accurate. The accuracy of the identified plant models are quantified by computing the variance accounted for, as shown earlier, for each path. We will refer to an *accurate* plant model as one that achieves a variance accounted for of at least 97%. In reverberant conditions, however, accurate identification of some cross paths is particularly difficult due to the reverberant nature of the field, as will be discussed further later.

5.2.1 Plant model

Each transfer path was modeled using the approach described in the previous section. The 20 seconds of I/O data was split into an identification set and a validation set, the latter of which was used to determine the accuracy of the model. In each case, the frequency response was computed using the Wiener filter solution, the H_1 estimator, and the LMS algorithm. The three models were evaluated qualitatively to study the accuracy of the estimated model. The variance accounted for (VAF) was then computed for each path to evaluate the model accuracy on a quantitative basis.

The frequency responses, measured in both anechoic and reverberant environments, of the paths from the right speaker to each of the four microphones are shown in the top portion of Figure 5.7. Due to the symmetry of the headrest and the relatively small separation distance between the ear microphones and the error microphones, the transfer paths are quite similar to one another. The cross paths are comparable to the direct paths with the exception that the magnitude response is roughly 10 dB less. The transfer paths from the center speaker to each microphone, which are shown in the bottom portion of Figure 5.7, are all very similar to one another due to the symmetry of the headrest. Although it is slightly difficult to observe in the phase diagram, it can be seen that the virtual paths have a slightly larger delay ($\approx$ 200-300 μs) than the transfer paths corresponding to the physical sensors. One other important characteristic of each path is the low magnitude response below about 250 Hz. This is due to the relatively small enclosures used to house the speakers effectively increasing the natural frequency of the secondary sources.

The plants measured in the reverberant environment are similar in shape to the anechoic plant, with the main difference being the damping of the acoustic environment. In a reverberant environment, the input-output signals used to identify each path were less correlated, due to the multiple reflections which were not present in the anechoic room. The coherence functions for each path are shown in Figure 5.8, and it can be seen that in a reverberant environment the coherence is significantly deteriorated compared to the anechoic environment.

The VAF values computed for each path are tabulated in Tables 5.1-5.2. In anechoic conditions, each model achieves a VAF of at least 97%, however it can be seen that the direct paths, *i.e.*,

Table 5.1: Variance accounted for values (%) for each path - anechoic

	Right speaker	**Left speaker**	**Center speaker**
Right PES	99.71	97.95	99.83
Left PES	99.24	99.82	99.90
Right VES	99.88	98.52	99.79
Left VES	98.48	99.87	99.74

Table 5.2: Variance accounted for values (%) for each path - reverberant

	Right speaker	**Left speaker**	**Center speaker**
Right PES	93.22	75.09	94.99
Left PES	75.27	94.64	94.70
Right VES	95.20	67.98	89.74
Left VES	64.83	96.22	88.68

from the right speaker to either the right PES or right VES, are slightly higher than the cross paths. This is due to the fact that the scattering of the head plays a larger role in the cross paths and adversely effects the certainty of the identified model. The decrease in the VAF for each of the paths in the reverberant room is due to poor I/O correlation properties as a result of multiple sound wave reflections. This is most pronounced for the cross paths because the path is dominated by sound waves reflected off of the head and room walls, rather than by the direct path from the source. The deterioration in the coherence functions measured in reverberant conditions can be seen in Figure 5.8. The plant delays have also been computed using cross correlation functions and are tabulated in Table 5.3. These delays heavily limit the performance of an adaptive feedback controller, as will be seen later in the chapter.

Table 5.3: Plant delays (ms)

	Right speaker	**Left speaker**	**Center speaker**
Right PES	1.4	2.4	1.4
Left PES	2.4	1.4	1.4
Right VES	1.5	2.5	1.6
Left VES	2.5	1.5	1.6

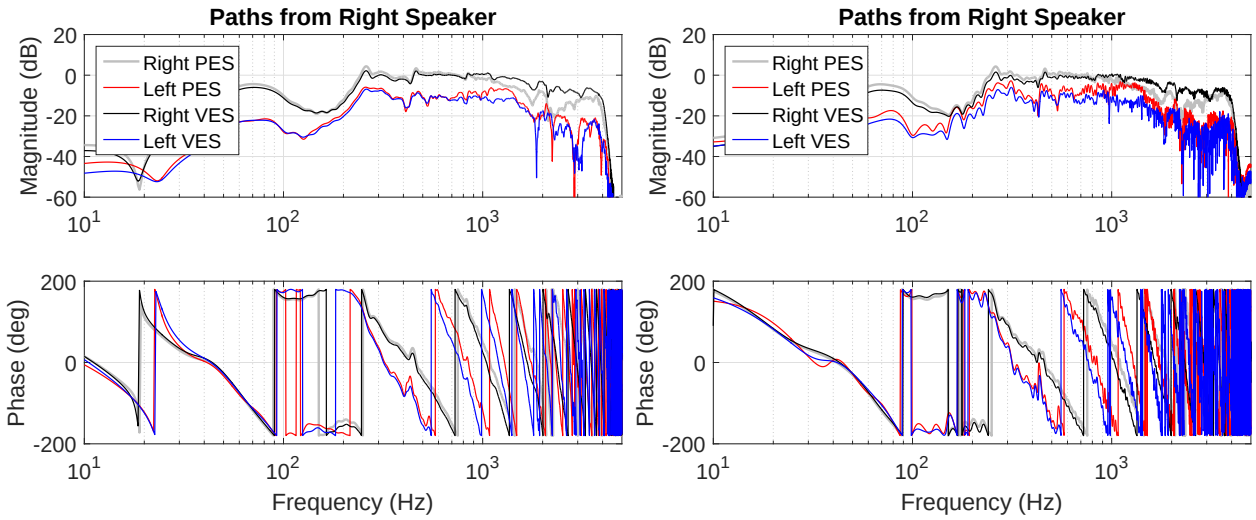

(a) Anechoic

(b) Reverberant

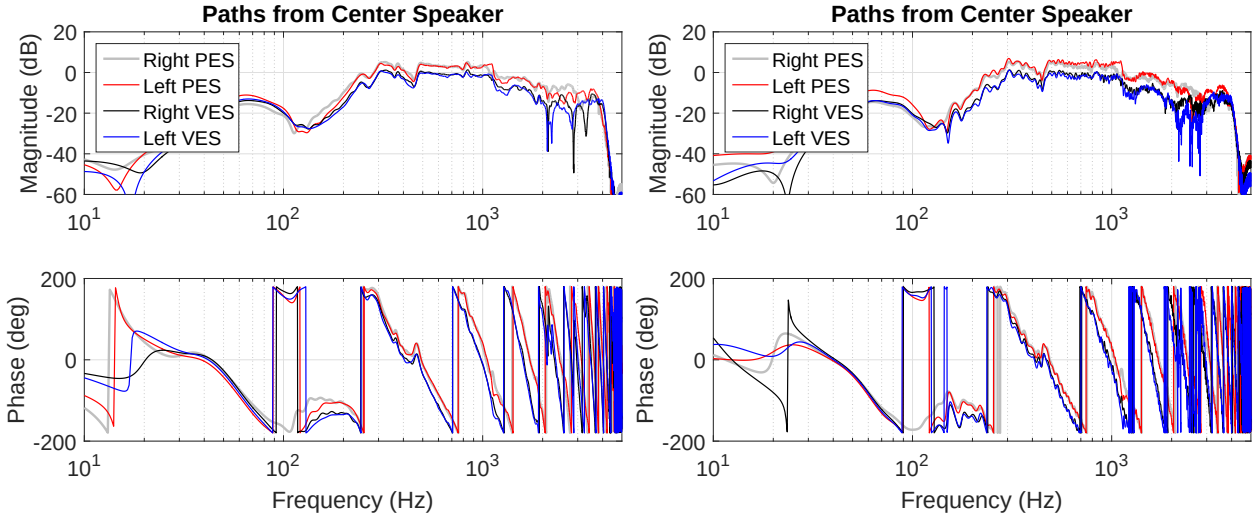

(c) Anechoic

(d) Reverberant

Figure 5.7: Transfer path estimates for the right and center speakers measured in anechoic and reverberant environments.

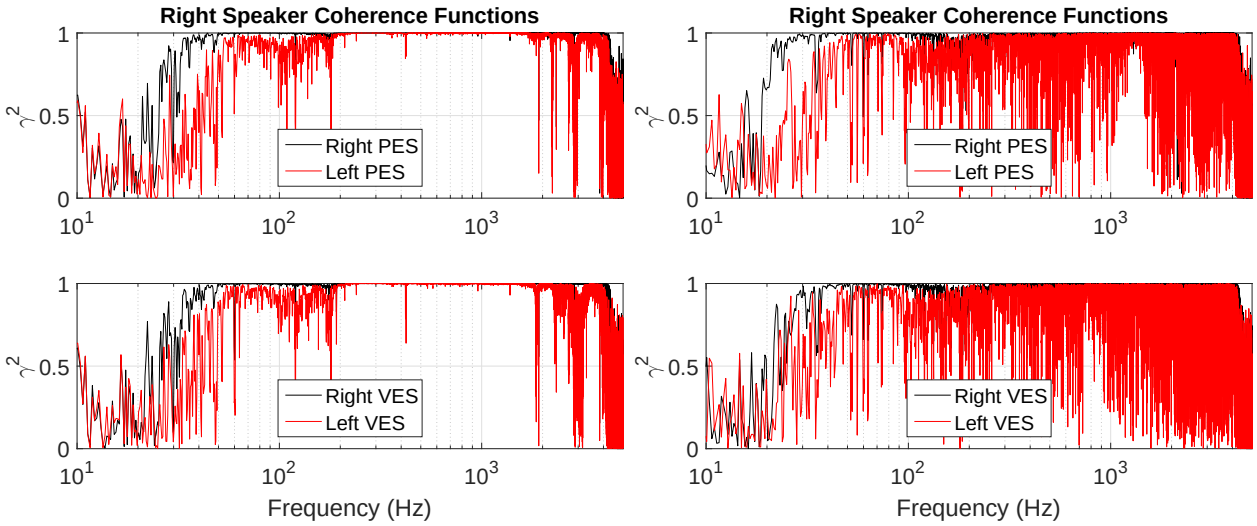

(a) Anechoic

(b) Reverberant

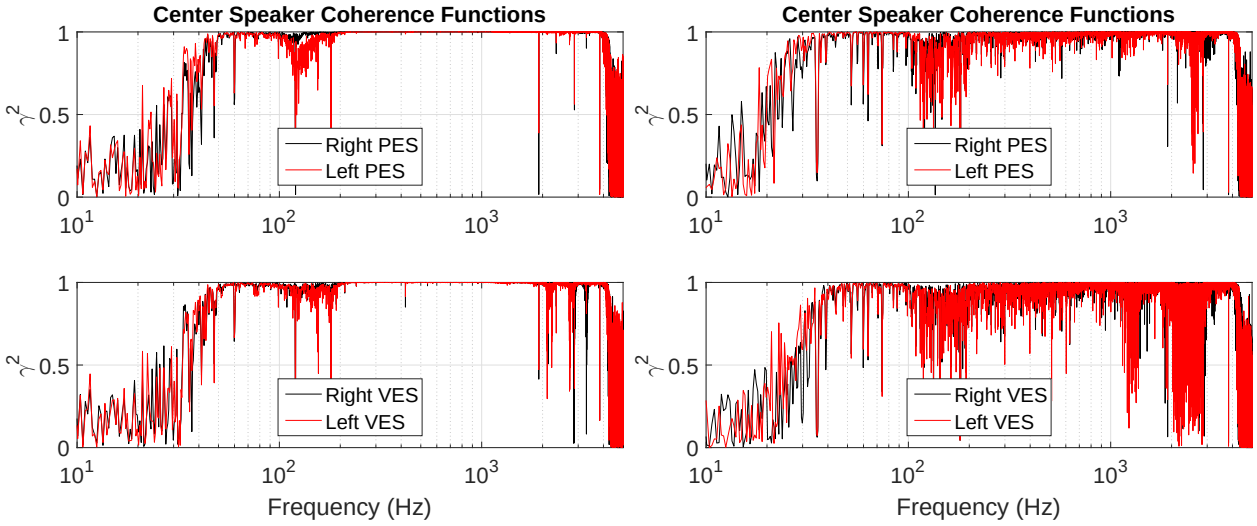

(c) Anechoic

(d) Reverberant

Figure 5.8: Coherence functions for the right and center speakers measured in anechoic and reverberant environments.

5.3 Control system design

The relevant equations in the feedback and feedforward controllers are presented in this section. The control filters are updated according to the multiple error LMS algorithm [9], hence much of this material can also be found in Chapter 2. The purpose of reviewing it here is to emphasize details regarding how the control signals are computed for the specific 3 actuator - 2 sensor configuration and to discuss certain real-time implementation details. In each control system implementation, the control filter lengths are set to I=512 with a corresponding sample rate of f_s=10 kHz.

5.3.1 Feedback control system

The terminology introduced in Chapter 2 refers to the control system as having K reference signals, L error sensors, and M actuators. For the feedback controller, the reference signals are synthesized using internal models for each path. Since the reference signals are estimates of the disturbance at the 2 error sensors, there will be $K = 2$ reference signals.

The control signals are computed according to

$$\begin{aligned} u_1(n) &= \sum_{i=0}^{I-1} w_{11i}(n)\hat{d}_1(n-i) + \sum_{i=0}^{I-1} w_{12i}(n)\hat{d}_2(n-i) \\ &= \boldsymbol{w}_{11}^T(n)\hat{\boldsymbol{d}}_1(n) + \boldsymbol{w}_{12}^T(n)\hat{\boldsymbol{d}}_2(n) \end{aligned} \tag{5.10}$$

$$\begin{aligned} u_2(n) &= \sum_{i=0}^{I-1} w_{21i}(n)\hat{d}_1(n-i) + \sum_{i=0}^{I-1} w_{22i}(n)\hat{d}_2(n-i) \\ &= \boldsymbol{w}_{21}^T(n)\hat{\boldsymbol{d}}_1(n) + \boldsymbol{w}_{22}^T(n)\hat{\boldsymbol{d}}_2(n) \end{aligned} \tag{5.11}$$

$$\begin{aligned} u_3(n) &= \sum_{i=0}^{I-1} w_{31i}(n)\hat{d}_1(n-i) + \sum_{i=0}^{I-1} w_{32i}(n)\hat{d}_2(n-i) \\ &= \boldsymbol{w}_{31}^T(n)\hat{\boldsymbol{d}}_1(n) + \boldsymbol{w}_{32}^T(n)\hat{\boldsymbol{d}}_2(n) \end{aligned} \tag{5.12}$$

The internally synthesized reference signals are given by subtracting the contribution of the controller from the error signals. This is written

$$\begin{aligned} \hat{d}_1(n) &= e_1(n) - \sum_{m=1}^{3}\sum_{j=0}^{J-1} \hat{g}_{1mj}u_m(n-j) \\ &= e_1(n) - \left(\hat{\boldsymbol{g}}_{11}^T\boldsymbol{u}_1(n) + \hat{\boldsymbol{g}}_{12}^T\boldsymbol{u}_2(n) + \hat{\boldsymbol{g}}_{13}^T\boldsymbol{u}_3(n)\right), \end{aligned} \tag{5.13}$$

$$\begin{aligned} \hat{d}_2(n) &= e_2(n) - \sum_{m=1}^{3}\sum_{j=0}^{J-1} \hat{g}_{2mj}u_m(n-j) \\ &= e_2(n) - \left(\hat{\boldsymbol{g}}_{21}^T\boldsymbol{u}_1(n) + \hat{\boldsymbol{g}}_{22}^T\boldsymbol{u}_2(n) + \hat{\boldsymbol{g}}_{23}^T\boldsymbol{u}_3(n)\right), \end{aligned} \tag{5.14}$$

where it is emphasized that $\hat{\boldsymbol{g}}_{lm}$ is an *estimate*, computed offline in the system identification phase, of the transfer path from the m-th actuator to the l-th error sensor. At each iteration, the vector of control filter coefficients is updated according to

$$\boldsymbol{w}(n+1) = \boldsymbol{w}(n) - \mu\hat{\boldsymbol{R}}(n)\boldsymbol{e}(n). \tag{5.15}$$

The matrix $\hat{\boldsymbol{R}}(n)$ contains the filtered reference signals and is defined as

$$\hat{\boldsymbol{R}}(n) = \begin{bmatrix} \hat{\boldsymbol{r}}_1(n) & \hat{\boldsymbol{r}}_1(n-1) & \cdots & \hat{\boldsymbol{r}}_1(n-I+1) \\ \hat{\boldsymbol{r}}_2(n) & \hat{\boldsymbol{r}}_2(n-1) & \cdots & \hat{\boldsymbol{r}}_2(n-I+1) \end{bmatrix}, \tag{5.16}$$

where

$$\hat{\boldsymbol{r}}_l(n) = \begin{bmatrix} \hat{r}_{l11}(n) & \hat{r}_{l12}(n) & \hat{r}_{l21}(n) & \hat{r}_{l22}(n) & \hat{r}_{l31}(n) & \hat{r}_{l32}(n) \end{bmatrix}. \tag{5.17}$$

The filtered reference signals are obtained by filtering the estimated disturbance signals by estimates of the secondary paths such that the k-th reference signal filtered by an estimate of the path from the m-th actuator to the l-th error sensor is given by

$$\begin{aligned} \hat{r}_{lmk}(n) &= \sum_{j=0}^{J-1} \hat{g}_{lmj}\hat{d}_k(n-j) \\ &= \hat{\boldsymbol{g}}_{lm}^T\hat{\boldsymbol{d}}_k(n). \end{aligned} \tag{5.18}$$

5.3.2 Feedforward control system

In the anechoic environment, a single primary source is used as the disturbance, hence the feedforward control system makes use of K=1 reference signal. In the reverberant environment however, four primary sources are used to generate the disturbance. In this case, the filters are driven by K=4 reference signals. The control signals are computed according to

$$\begin{aligned} u_1(n) &= \sum_{k=1}^{K}\sum_{i=0}^{I-1} w_{1i}(n)x_k(n-i) \\ &= \sum_{k=1}^{K} \boldsymbol{w}_1^T(n)\boldsymbol{x}_k(n) \end{aligned} \tag{5.19}$$

$$\begin{aligned} u_2(n) &= \sum_{k=1}^{K}\sum_{i=0}^{I-1} w_{2i}(n)x_k(n-i) \\ &= \sum_{k=1}^{K} \boldsymbol{w}_2^T(n)\boldsymbol{x}_k(n) \end{aligned} \tag{5.20}$$

$$\begin{aligned} u_3(n) &= \sum_{k=1}^{K}\sum_{i=0}^{I-1} w_{3i}(n)x_k(n-i) \\ &= \sum_{k=1}^{K} \boldsymbol{w}_3^T(n)\boldsymbol{x}_k(n), \end{aligned} \tag{5.21}$$

where $x(n)$ is the reference signal. At each iteration, the vector of control filter coefficients is updated according to

$$\boldsymbol{w}(n+1) = \boldsymbol{w}(n) - \mu\hat{\boldsymbol{R}}(n)\boldsymbol{e}(n). \tag{5.22}$$

The matrix $\hat{\boldsymbol{R}}(n)$ contains the filtered reference signals and is again defined by Equations 5.16-5.17, with the only exception being that the filtered reference signals are given by

$$\begin{aligned} r_{lmk}(n) &= \sum_{k=1}^{K}\sum_{j=0}^{J-1}\hat{g}_{lmj}x_k(n-j) \\ &= \sum_{k=1}^{K}\hat{\boldsymbol{g}}_{lm}^T\boldsymbol{x}_k(n). \end{aligned} \tag{5.23}$$

5.3.3 Virtual sensing

In both of the virtual sensing algorithms used here, the objective is to estimate the error signals at the virtual microphones. The vector of virtual error signals is given by

$$\boldsymbol{e}_v(n) = \boldsymbol{d}_v(n) + \boldsymbol{G}_v\boldsymbol{u}(n), \tag{5.24}$$

where subscript v denotes signal values measured at the virtual locations. The matrix $\boldsymbol{G}_v$ contains the FIR filters modeling the paths from each speaker to each virtual microphone and is obtained offline in the system identification step. In real-time operation, the virtual error signals must be estimated according to

$$\hat{\boldsymbol{e}}_v(n) = \hat{\boldsymbol{d}}_v(n) + \hat{\boldsymbol{G}}_v\boldsymbol{u}(n), \tag{5.25}$$

where $\hat{(\cdot)}$ represents an estimated quantity. Both virtual sensing approaches considered here require an additional system identification task with microphones temporarily located at the virtual locations. The next sections describe how estimates of the virtual disturbance and virtual error signals are obtained according to the virtual microphone arrangement and the remote microphone technique.

Virtual microphone arrangement

In the virtual microphone arrangement, the primary sound field is assumed not to change significantly between the physical and virtual locations. That is,

$$\hat{\boldsymbol{d}}_v(n) \approx \boldsymbol{d}_p(n). \tag{5.26}$$

In this case, the virtual pressure signals can be computed as

$$\hat{\boldsymbol{e}}_v(n) = \hat{\boldsymbol{d}}_p(n) + \hat{\boldsymbol{G}}_v\boldsymbol{u}(n). \tag{5.27}$$

The disturbance signals at the physical locations are estimated by subtracting the contribution of the control sources from the physical error signals such that

$$\hat{\boldsymbol{d}}_p(n) = \boldsymbol{e}_p(n) - \hat{\boldsymbol{G}}\boldsymbol{u}(n). \tag{5.28}$$

The virtual error signals are computed in real-time according to

$$\hat{\boldsymbol{e}}_v(n) = \hat{\boldsymbol{e}}_p(n) - \left(\hat{\boldsymbol{G}} - \hat{\boldsymbol{G}}_v\right)\boldsymbol{u}(n). \tag{5.29}$$

Remote microphone technique

In the remote microphone technique (RMT), an additional matrix of observation filters is used to estimate the virtual microphone signals from the physical microphone signals. The physical disturbance signals are filtered by the matrix of observation filters to provide estimates of primary disturbance signals at the virtual sensors such that

$$\hat{\boldsymbol{d}}_v(n) = \boldsymbol{O}\hat{\boldsymbol{d}}_p(n), \tag{5.30}$$

where the primary disturbance signals are again estimated according to Equation 5.28. The virtual error signals are then estimated according to

$$\hat{\boldsymbol{e}}_v(n) = \boldsymbol{O}\hat{\boldsymbol{d}}_p(n) + \hat{\boldsymbol{G}}_v\boldsymbol{u}(n). \tag{5.31}$$

The matrix of observation filters is computed in the offline system identification step by minimizing the estimation error

$$\boldsymbol{\xi}(n) = \boldsymbol{d}_v(n) - \hat{\boldsymbol{d}}_v(n), \tag{5.32}$$

where $\boldsymbol{d}_v(n)$ is a vector of the measured signals at the virtual sensors and $\hat{\boldsymbol{d}}_v(n)$ is a vector of estimates given by Equation 5.30. To compute the coefficients of the observation matrix, the problem will be formulated as a multichannel filtering problem [2], where each observation filter is modeled as a J length FIR filter.

For a system consisting of N_p physical microphones and N_v virtual microphones, the estimate of the disturbance signal at the n_v-th virtual microphone is given by

$$\hat{d}_{n_v}(n) = \sum_{n_p=1}^{N_p}\sum_{j=0}^{J-1} o_{n_v n_p j}\, d_{n_p}(n-j), \tag{5.33}$$

where $o_{n_v n_p j}$ is the j-th coefficient of the FIR representing the observation filter from the n_p-th physical microphone to the n_v-th virtual microphone. The matrix of optimal observation filters minimizes, in a least squares sense, the estimation error given by Equation 5.32. The physical disturbance signals, which are the reference signals in this multichannel filtering problem, are filtered by a matrix of observation filters such that the estimation error can be written in vector form as

$$\boldsymbol{\xi}(n) = \boldsymbol{d}_v(n) - \sum_{j=0}^{J-1}\boldsymbol{O}_j\boldsymbol{d}_p(n). \tag{5.34}$$

The $N_v \times N_p$ matrix of observation filter coefficients is defined as

$$\boldsymbol{O}_j = \begin{bmatrix} o_{11j} & o_{12j} & \cdots & o_{1N_pj} \\ o_{21j} & o_{22j} & & \\ \vdots & & \ddots & \\ o_{N_v1j} & \cdots & & o_{N_vN_pj} \end{bmatrix}. \tag{5.35}$$

The $N_p \times 1$ vector of physical disturbances is defined as

$$\boldsymbol{d}_p(n) = \begin{bmatrix} d_{p_1}(n) & d_{p_2}(n) & \cdots & d_{p_{N_p}}(n) \end{bmatrix}^T, \tag{5.36}$$

along with the vector of virtual disturbance estimates given by

$$\boldsymbol{d}_v(n) = \begin{bmatrix} d_{v_1}(n) & d_{v_2}(n) & \cdots & d_{v_{N_v}}(n) \end{bmatrix}^T. \tag{5.37}$$

The optimal set of filter coefficients minimizes the squared estimation error given by

$$\begin{aligned} J &= E\left[\boldsymbol{\xi}^T(n)\boldsymbol{\xi}(n)\right] \\ &= \text{trace}\left\{E\left[\boldsymbol{\xi}(n)\boldsymbol{\xi}^T(n)\right]\right\}. \end{aligned} \tag{5.38}$$

The least squares solution is found by differentiating Equation 5.38 with respect to the filter coefficients and equating to zero. This results in the optimal set of filter coefficients given by

$$\boldsymbol{O}_{opt} = \boldsymbol{R}_{pp}\boldsymbol{R}_{pv}^{-1}, \tag{5.39}$$

where the $N_pJ \times N_pJ$ of auto and cross correlation elements for the reference signals is given by

$$\boldsymbol{R}_{pp} = \begin{bmatrix} \boldsymbol{R}_{pp}(0) & \boldsymbol{R}_{pp}(-1) & \cdots & \boldsymbol{R}_{pp}(1-J) \\ \boldsymbol{R}_{pp}(1) & \boldsymbol{R}_{pp}(0) & & \\ \vdots & & \ddots & \\ \boldsymbol{R}_{pp}(J-1) & \cdots & & \boldsymbol{R}_{pp}(0) \end{bmatrix}, \tag{5.40}$$

and the $N_pJ \times N_v$ matrix of cross correlation elements as

$$\boldsymbol{R}_{pv} = \begin{bmatrix} \boldsymbol{R}_{pv}(0) & \boldsymbol{R}_{pv}(1) & \cdots & \boldsymbol{R}_{pv}(J-1) \end{bmatrix}^T. \tag{5.41}$$

The individual auto and cross correlation matrices that make up the elements of the matrices in Equations 5.40-5.41 are defined as

$$\boldsymbol{R}_{pp}(m) = E\left[\boldsymbol{d}_p(n+m)\boldsymbol{d}_p^T(n)\right], \tag{5.42}$$

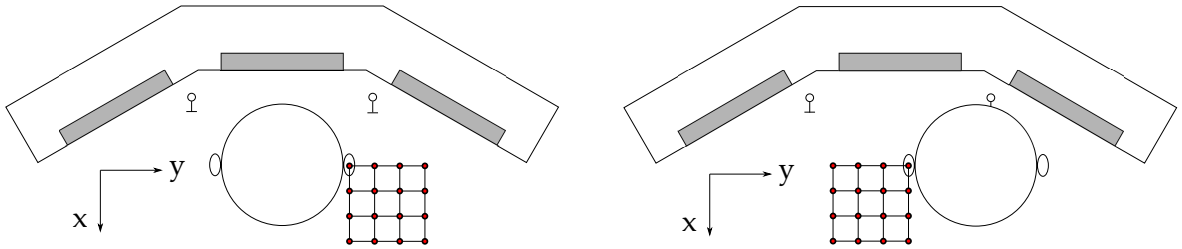

(a) Left ear measurement locations (b) Right ear measurement locations

Figure 5.9: Grid of various head positions.

$$\boldsymbol{R}_{pv}(m) = E\left[\boldsymbol{d}_v(n+m)\boldsymbol{d}_p^T(n)\right]. \tag{5.43}$$

With the matrix of observation filters computed, the virtual error signals can be computed in real-time according to Equation 5.31. It is worth noting that if the primary sound field is tonal and deterministic, each observation filter can be parameterized as a J=2 length FIR whose coefficients are adjusted to match the exact magnitude and phase shift between the physical and virtual microphones, hence providing a perfect estimate of the virtual signals. This will also depend on the accuracy of the identified plant responses $\boldsymbol{G}$ and $\boldsymbol{G}_v$. On the other hand, if the sound field is random, *e.g.*, a diffuse sound field, the matrix of observations filters minimizes statistically averaged signal quantities, and hence will not provide a perfect estimate of the virtual signals for any given realization of the sound field.

5.4 Results

The performance of the active headrest is quantified by measuring the spatial extent of the quiet zone. This is accomplished by moving the manikin head to 16 different positions and measuring the noise reduction at each ear. The noise reduction at each ear was measured after moving the head in 1" increments to the side and forward. Figure 5.9 shows the points where the noise reduction was measured for each ear. Due to the symmetry of the headrest, the head was only moved in one lateral direction, *i.e.*, the $+y$ direction. For each measurement location, the controller was allowed to re-adapt until it converged to a nearly steady state solution. This is in contrast to some previous studies of an active headrest [48], where the performance of a fixed controller was evaluated for various head positions. It should also be emphasized that the procedure used to measure the quiet zones accounts for plant variations, which is in contrast to some past studies [49, 50].

Initially, the main objective of the testing was to measure the spatial extent of the quiet zones for a series of tonal disturbances in both anechoic and reverberant sound fields. After a preliminary investigation into the performance of the headrest in a reverberant sound field, it was found that a tonal diffuse sound field was not realizable in the reverberation chamber, at least for the low frequencies considered here. For tonal primary sound fields, the acoustic response of

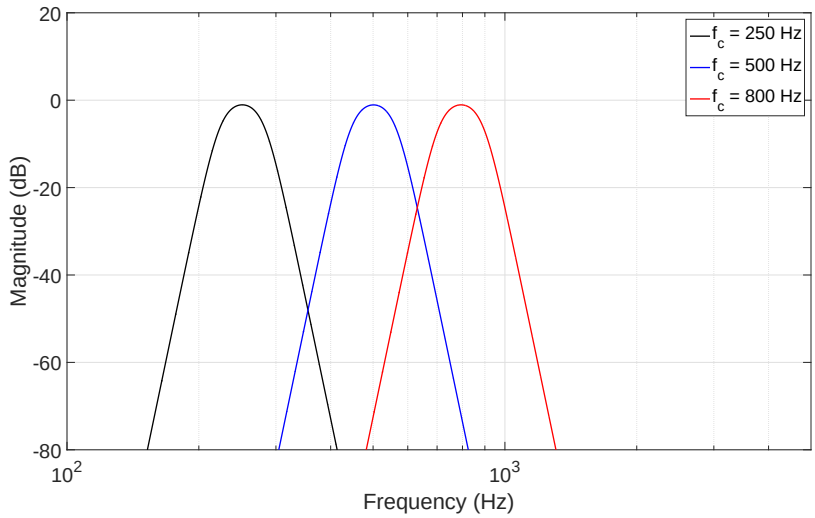

Figure 5.10: Disturbance spectra

the room is dominated by modes, and hence could not be treated as diffuse. A more detailed discussion of this behavior is provided in Appendix A.

In order to increase the diffusivity of the primary sound field, band-limited disturbances were considered as an alternative to individual tones. By increasing the frequency bandwidth of the primary sound field, more room modes were excited and a more spatially uniform/diffuse sound field was realized. The primary disturbances used in this study contained frequency content within various one-third octave bands. The lower, center, and upper frequency limits for the one-third octave bands are outlined in Table 5.4. The 250 Hz, 500 Hz, and 800 Hz one-third octave bands were chosen to generate the primary sound fields. The spectra of the three candidate disturbances are shown in Figure 5.10.

5.4.1 Anechoic: tonal disturbance

The first series of tests in the anechoic environment considered tonal primary sound fields. For each of the 16 manikin head positions shown in Figure 5.9, the noise reduction at each ear was measured. This was accomplished by turning on the primary disturbance followed immediately by the controller, which was allowed to converge for 40 seconds before measuring the controlled signals. The primary source was placed 3 meters behind the headrest such that the primary field consists of a plane wave. The performance was measured for three different fundamental frequencies, namely 300 Hz, 500 Hz, and 700 Hz. For these tests the controller is entirely feedforward, with the signal generating the primary disturbance acting simultaneously as the reference signal. In the first configuration, the control system was adjusted to minimize the signals at the physical microphones, as is done in traditional ANC systems. Next, the two virtual sensing algorithms described above were implemented in the control system to minimize

Table 5.4: One-third octave band frequency limits

Lower frequency (Hz)	Center frequency (Hz)	Upper frequency (Hz)
70	80	89
89	100	112
112	125	141
141	160	178
178	200	224
224	250	282
282	315	355
355	400	447
447	500	562
562	630	708
708	800	891
891	1000	1122

the estimated signals at the manikin ears.

After measuring the noise reduction for each ear at the 16 locations, the grid was interpolated so that the quiet zones could be visualized for each frequency and control approach. The 5 dB, 10 dB, and 15 dB quiet zones are shown in Figures 5.11-5.12. The first column corresponds to the case where the controller minimizes the signals at the physical error sensors (PES). For the results shown in the middle column, the controller minimizes the virtual signals estimated according to the virtual microphone arrangement (VMA). The results corresponding to the remote microphone technique (RMT) are shown in the third column.

At 300 Hz, all three approaches result in at least 10 dB of attenuation at each ear when the head is in the nominal position, however, the spatial extent of the 10 dB quiet zone is greatly improved when virtual sensing is used to estimate the signals at the manikin ears. At 500 Hz, the only approach capable of achieving at least 10 dB reduction is the RMT. At this frequency and higher, the assumption of equal pressure at the physical and virtual locations, as made in the VMA, becomes increasingly less valid as the characteristic wavelengths of the primary field decrease. The directivity of the secondary sources also becomes more pronounced at higher frequencies, as discussed in Chapter 4, leading to variations in the spatial extent of the quiet zones. At 700 Hz, no control strategy is able to reduce the primary sound field by at least 10 dB over a practical range of head positions. The RMT, however, does achieve about 10 dB of reduction for the nominal head position, which is more than the other two approaches.

The spatial extent of the quiet zones, most notably for tonal disturbances, is heavily influenced

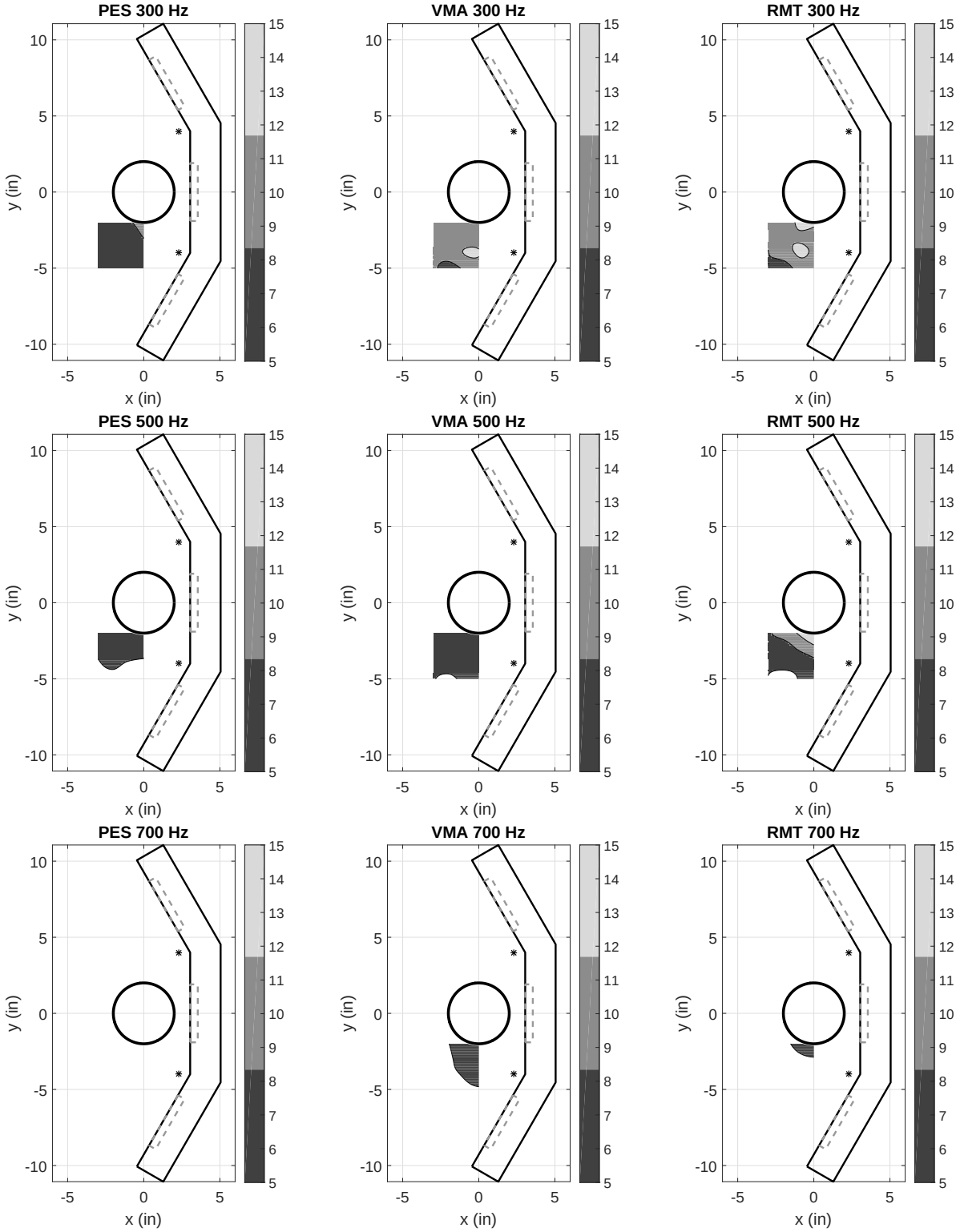

Figure 5.11: Anechoic conditions. 5 dB, 10 dB, and 15 dB quiet zones measured at the left manikin ear for a tonal primary sound field.

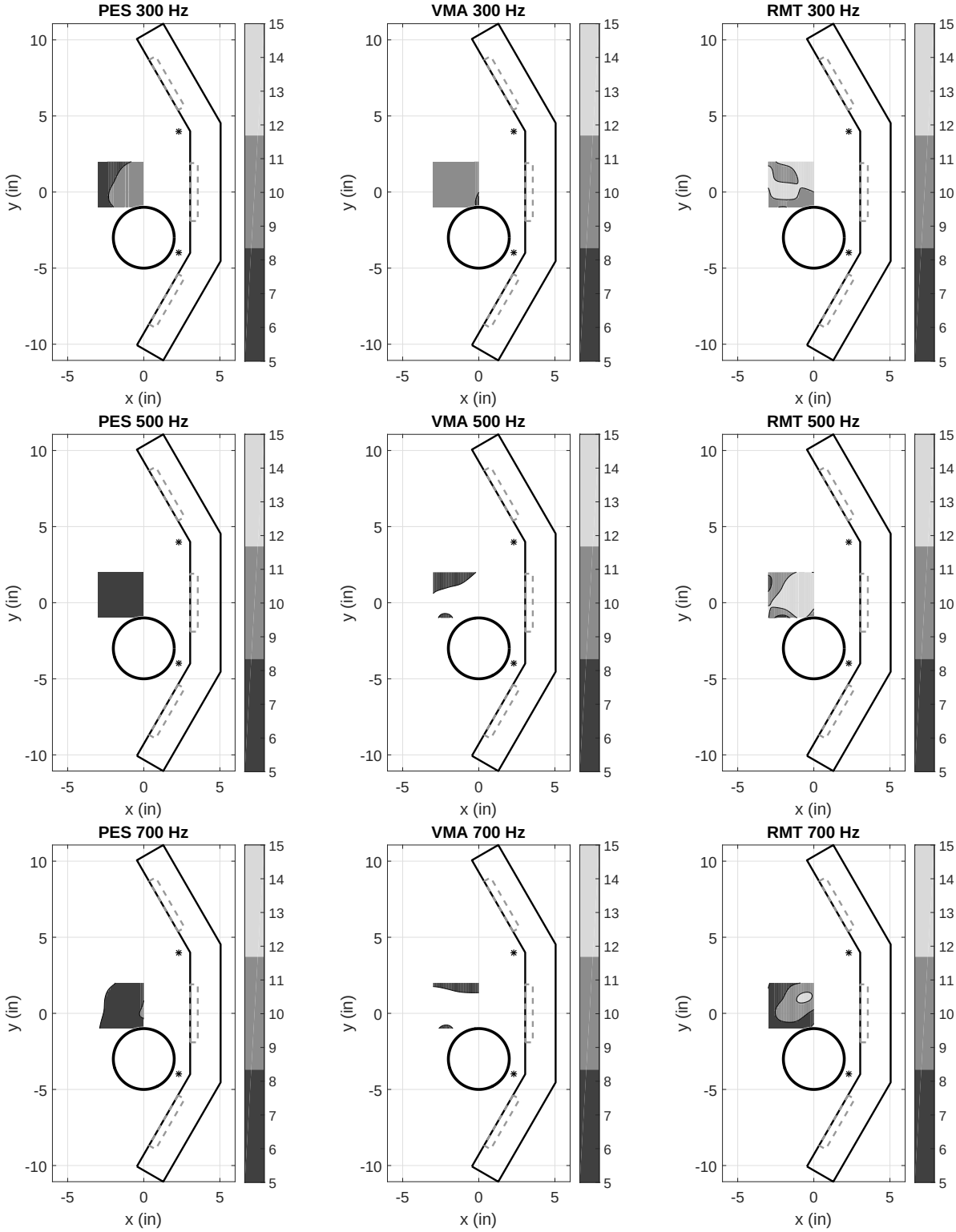

Figure 5.12: Anechoic conditions. 5 dB, 10 dB, and 15 dB quiet zones measured at the right manikin ear for a tonal primary sound field.

by the positions of the physical error sensors relative to the head and secondary loudspeakers. Much better performance could be achieved if, for example, the error sensors were moved forward, such that the distance d_1 in Figure 5.5 approaches zero. However, this constrained the lateral movement of the head, and was deemed an unfit configuration. The spatial extent of the quiet zones presented here are thus representative of a practical scenario in which the error sensors are located behind the head, as to not interfere with an occupant's head movement. For primary sound fields consisting of plane waves at a single frequency, significantly improved performance can be achieved by estimating the virtual disturbance signals using a matrix of observation filters, as is done in the RMT.

5.4.2 Anechoic: band-limited disturbance

Feedforward control

In this section, the performance of the active headrest is evaluated for disturbances with frequency content in various one-third octave bands. The three disturbance spectra considered here are shown in Figure 5.10. To quantify the noise reduction over a finite bandwidth, the reduction in sound pressure level was integrated over each one-third octave band. The noise reduction, in dB, is thus given by

$$\mathrm{NR} = 10\log_{10}\left(\sum_{f=f_l}^{f_u} P_u(f)\right) - 10\log_{10}\left(\sum_{f=f_l}^{f_u} P_c(f)\right), \tag{5.44}$$

where $P_u(f)$ and $P_c(f)$ are the power spectra of the uncontrolled and controlled microphone signals and f_l and f_u are the lower and upper frequencies for each band.

In the first series of tests, the feedforward control system described above is employed, with the signal driving the primary disturbance source acting simultaneously as the reference. Although it may be argued that a perfect reference signal would not be available in practice, this approach helps to form an upper limit on the acoustic performance of the headrest.

The 5 dB and 10 dB quiet zones for the left and right manikin ears are shown in Figures 5.13-5.14. The first column shows the resulting quiet zones when the controller was adjusted to cancel the signals at the physical error sensors (PES). The second and third columns correspond to results where the controller is adjusted to minimize the virtual signal estimates according to the virtual microphone arrangement (VMA) and the remote microphone technique (RMT), respectively. For the 250 Hz one-third octave band disturbance, all three approaches achieve at least 5 dB of noise reduction at each ear for head movements of ± 3" laterally and forward. Using virtual sensing, however, reductions of at least 10 dB can be achieved in this frequency range for a practical range of head movements.

For the 500 Hz one-third octave band disturbance, the quiet zones corresponding to cancellation at the physical error sensors and the remote microphone technique are comparable and

provide at least 5 dB reductions over the majority of measurement locations. For the VMA, about 5 dB reduction is achieved at the nominal head position, although the reduction at the right ear is degraded for any lateral head movements greater than 1". This is likely due to the assumption that the pressure is similar at the physical and virtual locations becoming less valid as the virtual sensor is moved away from the physical sensor. The opposite is true for the left ear, where slightly increased noise reductions are achieved due to the virtual sensor moving closer to the physical sensor. For the 800 Hz one-third octave band disturbance, no approaches are able to generate significant quiet zones. It is worth noting that, when minimizing the signals at the physical sensors, the attenuation at the right ear improves drastically as the head is moved laterally. This implies that for this approach, the quiet zone is focused at the center of the head, which is somewhat intuitive given the spatial arrangement of the loudspeakers and physical microphones.

One issue worth noting, which arose when implementing the remote microphone technique, involved modeling the matrix of observation filters. To perfectly estimate the matrix of observation filters, a causal relationship between the physical and virtual sensor must exist. For the tonal disturbances described in the previous section, this was not an issue, and the matrix of observation filters could be computed such that accurate estimates of the virtual signals were predicted. For the one-third octave band disturbances considered here, the causality constraint limits the accuracy of the matrix of observation filters. Since the noise source is behind the headrest, the plane wave should reach the physical sensors before the virtual sensors, albeit only by the time it takes the wave to propagate ≈5", *i.e.*, 300-400 μs. Due to the finite bandwidth of the primary disturbance spectra, realizing a causal filter that accurately describes the relationship between the physical and virtual locations was not possible. This was confirmed by computing the frequency response of the transfer function given by $O = S_{pv}/S_{pp}$ and observing that the phase was either zero or positive in the frequency bandwidth of interest.

Feedback control

In many cases, a well correlated reference signal may not be available, and use of feedback control is appealing. In this section, the spatial extent of the quiet zone is characterized again for one-third octave band disturbances, but with a feedback control architecture. The feedback control system described in Section 5.3.1 is employed here and uses an internal model of the plant to synthesize driving signals for the feedback filters. The noise reduction capabilities of the feedback system depend heavily on plant delays, plant model accuracy, and disturbance bandwidth, and hence are not expected to be comparable to the feedforward results. Since in this case the integrated reductions are much lower, the results are presented in terms of 3 dB, 4 dB, and 5 dB quiet zones.

For the one-third octave band disturbances with center frequencies of 500 Hz and 800 Hz, no sensing approach resulted in significant noise reductions at the manikin ears. For the 250 Hz one-third octave band disturbance, however, the use of virtual sensors offers improved perfor-

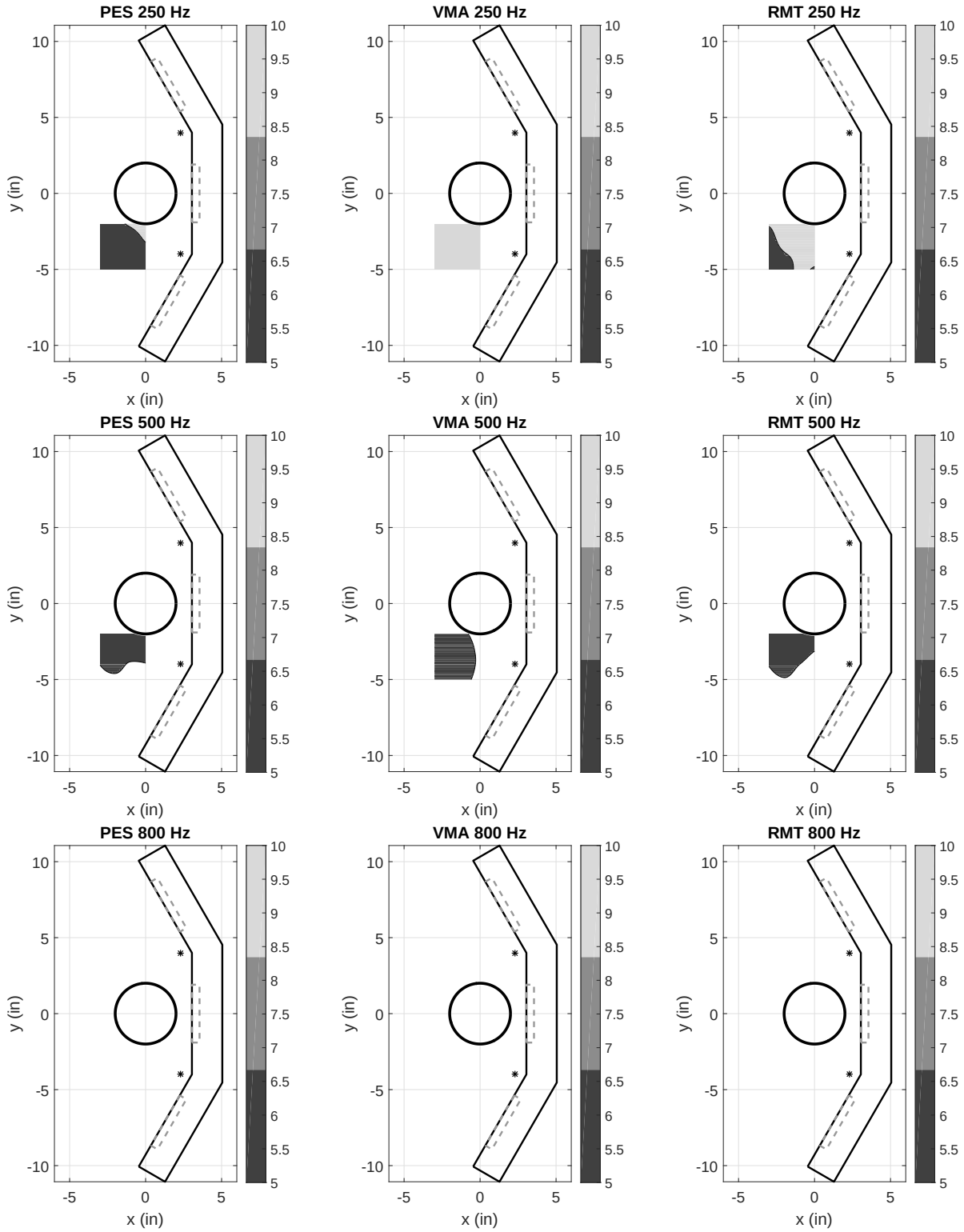

Figure 5.13: Anechoic conditions. 5 dB and 10 dB quiet zones measured at the left manikin ear for one-third octave band disturbances when the controller is feedforward with a perfect reference signal.

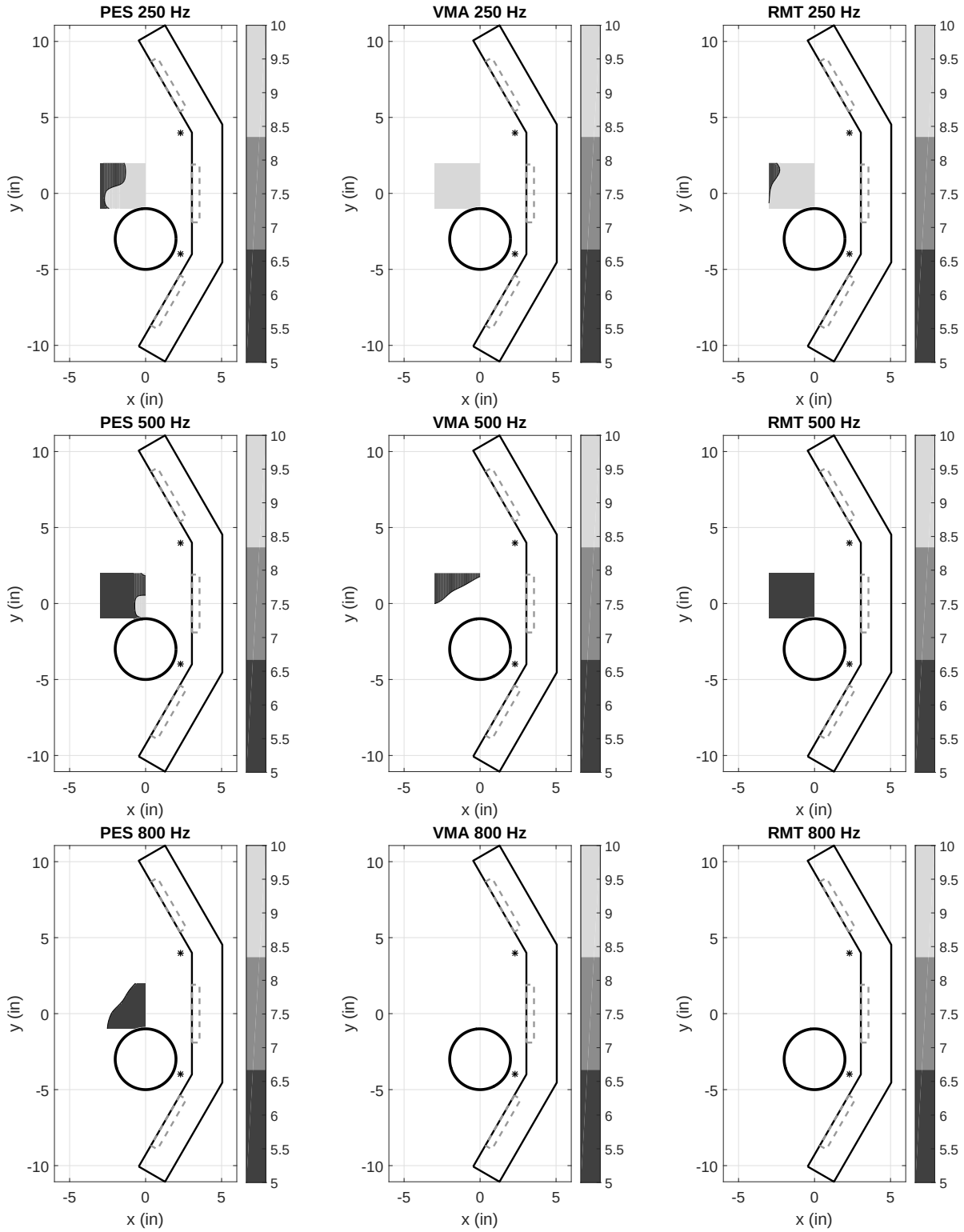

Figure 5.14: Anechoic conditions. 5 dB and 10 dB quiet zones measured at the right manikin ear for one-third octave band disturbances when the controller is feedforward with a perfect reference signal.

mance. For this disturbance spectrum, the quiet zones are shown in Figure 5.16, for each of the three techniques. When the feedback controller was adjusted to minimize the signals at the physical error sensors (PES), only about 3-4 dB of reduction was achieved at the ears, although these reductions were observed over the entire grid of measurement locations. When the controller was adjusted to minimize the virtual signals, estimated according to the remote microphone technique (RMT), only about 2-3 dB reductions were seen. The virtual microphone arrangement (VMA), which assumes the primary sound field is roughly equivalent at the physical and virtual locations, was able to achieve 5-6 dB reduction for head movements of about ± 2" laterally and in the forward direction.

It is interesting to note that the remote microphone technique performed significantly better in a feedforward configuration as opposed to a feedback one. The reason for this can be explained as follows. When feedforward control, with a perfect reference, was employed, the remote microphone technique and virtual microphone arrangement performed very similarly for the 250 Hz one-third octave band disturbance. In the feedback configuration, however, the virtual microphone arrangement achieves about 3-4 dB more reduction than the remote microphone technique. This can be attributed to inaccuracies in the matrix of observation filters propagating through the control system to result in inaccurate driving signals for the feedback filters. To clarify, consider the block diagram in Figure 5.15, which shows a single channel feedback system employing the remote microphone technique. The feedback system synthesizes a reference signal, which is meant to be an estimate of the disturbance at the virtual location. In the remote microphone technique, the disturbance signal at the virtual location is generated by filtering the disturbance signal at the physical locations by the observation filter, $O(z)$ (Equation 5.30), which is in error, mainly due to the non-causal relationship between the physical and virtual microphones. In the feedforward configuration, a perfect reference was available to drive the filters, hence the system was less influenced by inaccuracies in the matrix of observation filters.

5.4.3 Reverberant: band-limited disturbance

Feedforward control

Feedforward control relies on the availability of a reference signal that is well correlated with the disturbance to be canceled. In an anechoic environment where the sound field is dominated by the direct path from the speaker, the signal driving the primary source will be well correlated with the digitally sampled signal from a microphone placed at any point in the field. In a reverberant environment however, the sound field is dominated by reflections and this will no longer be the case.

The coherence functions computed for one reference signal and one microphone signal, corresponding to each of the three one-third octave band disturbance spectra, are shown in Figure 5.17, and are representative of all other coherence functions. It is only necessary that the sig-

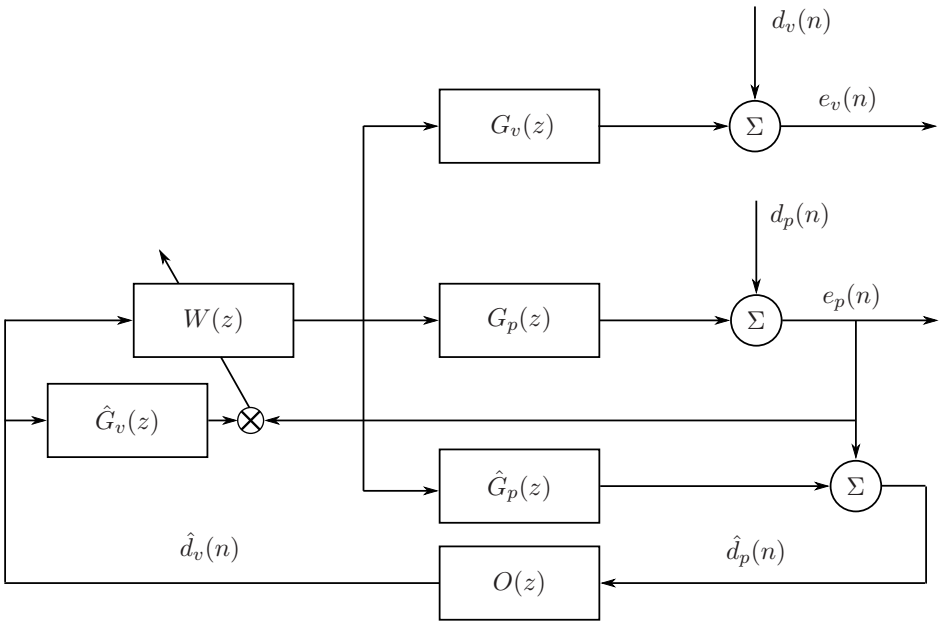

Figure 5.15: Block diagram of a single channel feedback system employing the remote microphone technique and FxLMS.

nals be coherent in the disturbance bandwidth, however it can be seen that the coherence is rarely greater than about 0.5 in any case. To understand the effect that this has on controller performance, one might consider the single channel case. In order to achieve at least 10 dB attenuation in a single channel system, the coherence must be at least 0.9 [2]. To obtain 20 dB, the coherence must be at least 0.99 [2]. In computing these bounds, some assumptions regarding the frequency response of the plant and the causality of the optimal filter are made, hence they are not strictly enforced. Due to the poor coherence between the reference and disturbance signals, the feedforward control system was only able to achieve about 1 dB integrated reduction for any disturbance bandwidth.

Feedback control

The feedback control system described in Section 5.3.1 has been employed to minimize one-third octave band disturbances in a reverberant sound field. As was the case in all prior tests, the feedback system was incapable of achieving significant noise reductions for the disturbances with center frequencies of 500 Hz and 800 Hz. For the disturbance with a center frequency of 250 Hz, however, the control system achieved integrated reductions of 3-5 dB for the majority of measurement locations.

The measured noise reductions, presented in terms of 3 dB, 4 dB, and 5 dB quiet zones, are shown in Figure 5.18. The first column corresponds to cancellation at the physical error sensors (PES). The second and third column correspond to cases where the virtual microphone

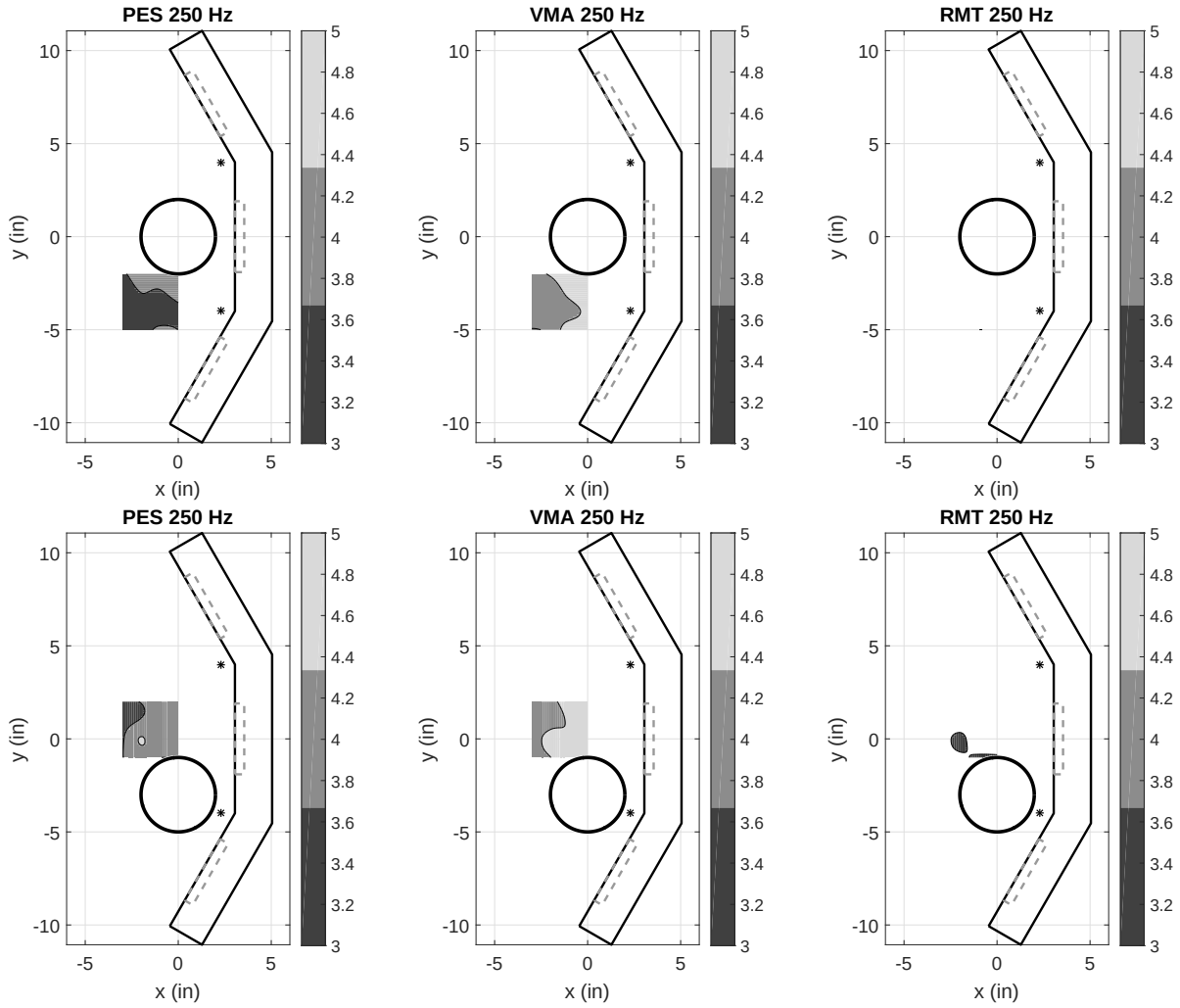

Figure 5.16: Anechoic conditions. 3 dB, 4 dB, and 5 dB quiet zones measured at the left and right manikin ears for one-third octave band disturbances when the controller is feedback.

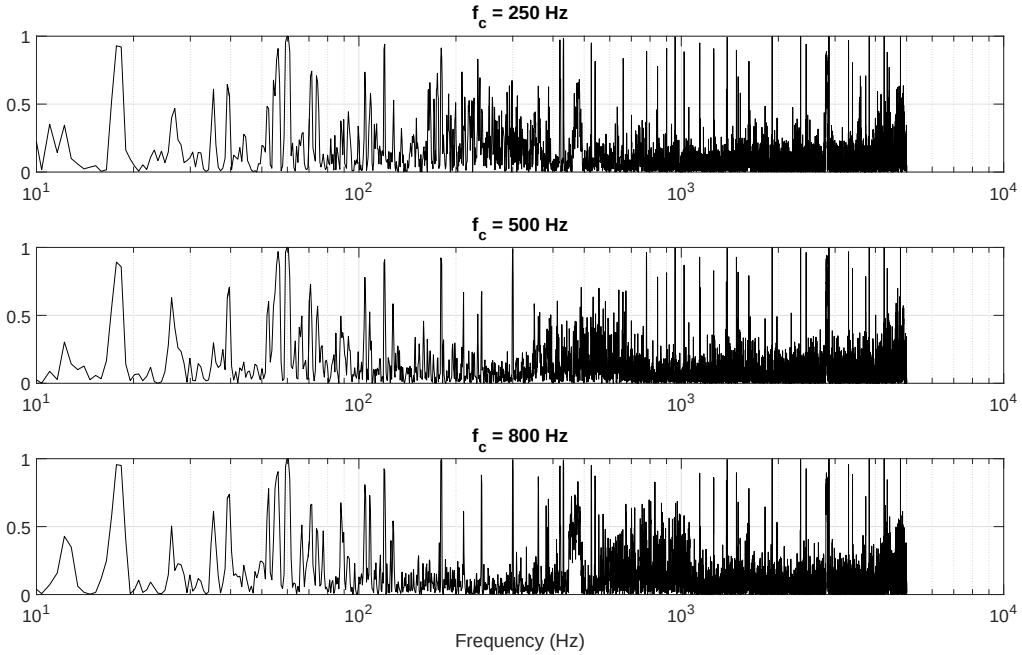

Figure 5.17: Reference signal - disturbance signal coherence functions.

arrangement (VMA) and the remote microphone technique (RMT) were used to estimate the virtual signals. Using the virtual microphone arrangement to estimate the virtual signals does not provide any significant improvement in terms of the spatial extent of the zone of quiet relative to cancellation at the physical sensors. This difference was more pronounced in the tests performed in an anechoic environment and is likely not seen here because of the added complexity of the sound field. Incoherent waves traveling in many directions have, evidently, resulted in the assumption of equal pressure at the physical and virtual locations being less valid. Although the sound level is more or less uniform, the phase at any point in the field is random. As a consequence, the assumption of equal primary pressure (amplitude *and* phase) at the physical and virtual locations is less valid in a diffuse sound field. As was also seen in the anechoic tests, the remote microphone technique results in negligible noise reduction. This is again due to inaccuracies in the matrix of observation filters. Moreover, these modeling errors are augmented in a reverberant sound field due to poor coherence between physical and virtual sensor signals.

Insight into the performance of the feedback controller in contrasting acoustic environments can be gained by comparing Figures 5.16 and 5.18. On average, the integrated noise reductions measured in a reverberant sound field are about 1-2 dB less than what can be achieved in anechoic conditions. This is an intuitive result, and is due to the fundamental differences in the nature of the sound field in the two environments. For an active headrest, the use of virtual sensors also provides a smaller benefit in reverberant sound fields as compared to ane-

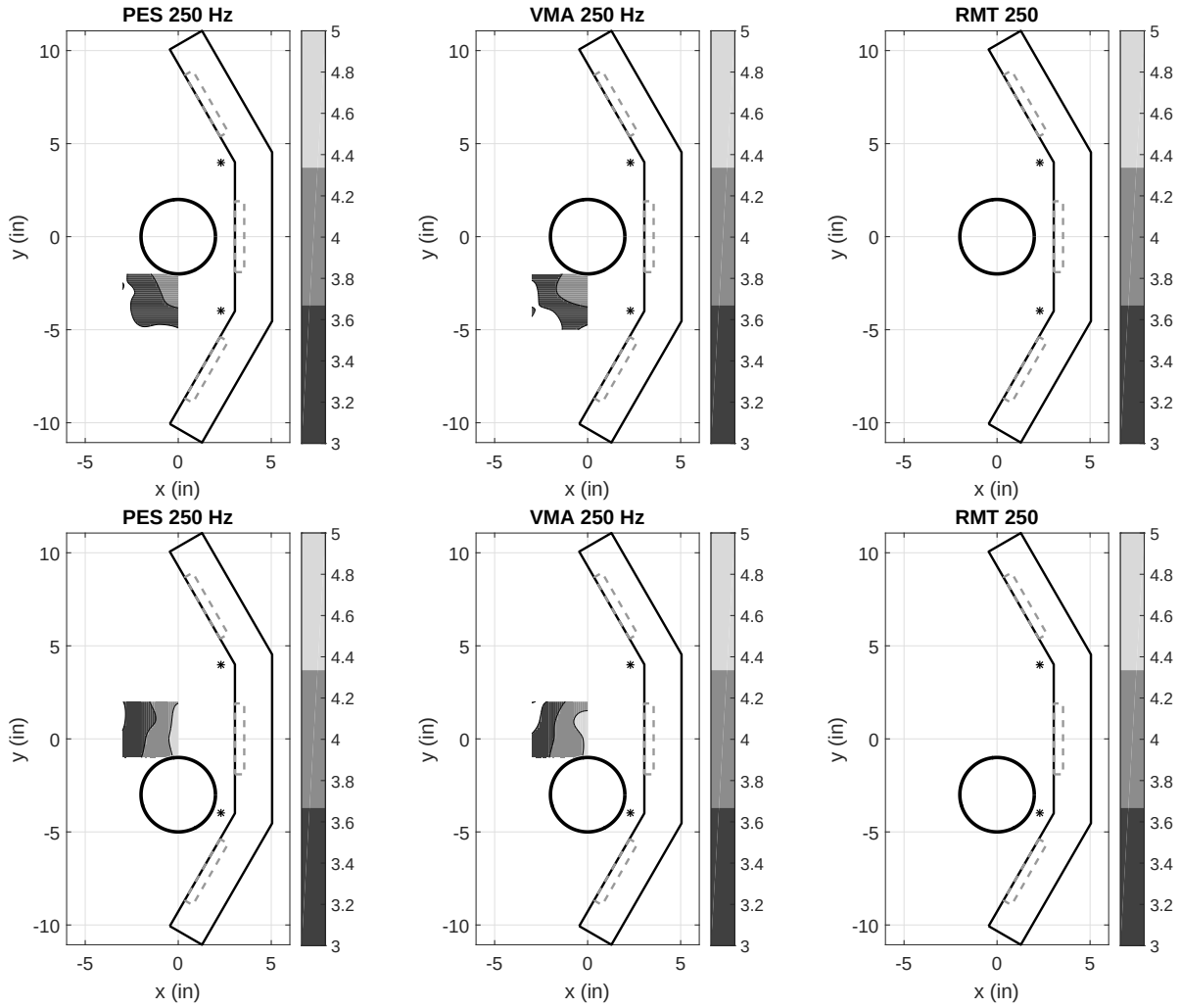

Figure 5.18: Reverberant conditions. 3 dB, 4 dB, and 5 dB quiet zones measured at the left and right manikin ears for one-third octave band disturbances when the controller is feedback.

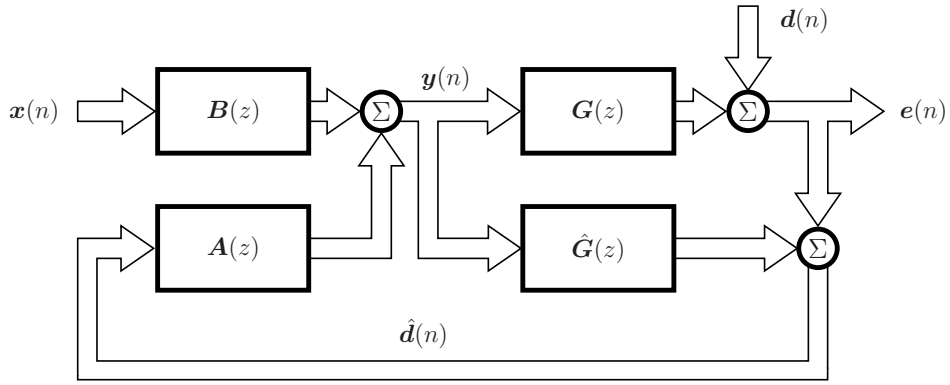

Figure 5.19: Block diagram of a multichannel hybrid active noise control system.

choic conditions. Furthermore, for a feedback controller employing an internal plant model, successful implementation of the remote microphone technique hinges upon accurately identifying the matrix of observation filters and ensuring that a causal relationship exists between the noise source, and the physical and virtual sensors.

5.4.4 Combined feedforward-feedback control

The noise reduction performance of the active headrest prototype has been thoroughly assessed for various control strategies and primary sound field conditions. In this section, the performance of a combined feedforward-feedback control system, commonly referred to as a hybrid system, will be investigated. For each test described here, measurements were taken with the headrest located in a normal room with cement floors and various laboratory equipment present. This is meant to represent a practical acoustic environment in which the sound field is semi-reverberant, such as the acoustic environment inside the crew module shown in Figure 4.1.

Consider the multichannel hybrid control system shown in Figure 5.19. The matrices of feedforward and feedback control filters, $\boldsymbol{A}(z)$ and $\boldsymbol{B}(z)$, are driven by the reference signals $\boldsymbol{x}(n)$ and the internally synthesized disturbance signal estimates $\hat{\boldsymbol{d}}(n)$. Both sets of control filters are updated according to the multiple error LMS algorithm [26]. In this hybrid control system, the feedforward controller attenuates signal components that are correlated with the reference signal while the feedback controller simultaneously attenuates uncorrelated disturbance components.

Results

In the following tests, the reference signal consists of a band-limited disturbance with energy in the 200-400 Hz bandwidth. The disturbance signal consists of the reference signal plus an ad-

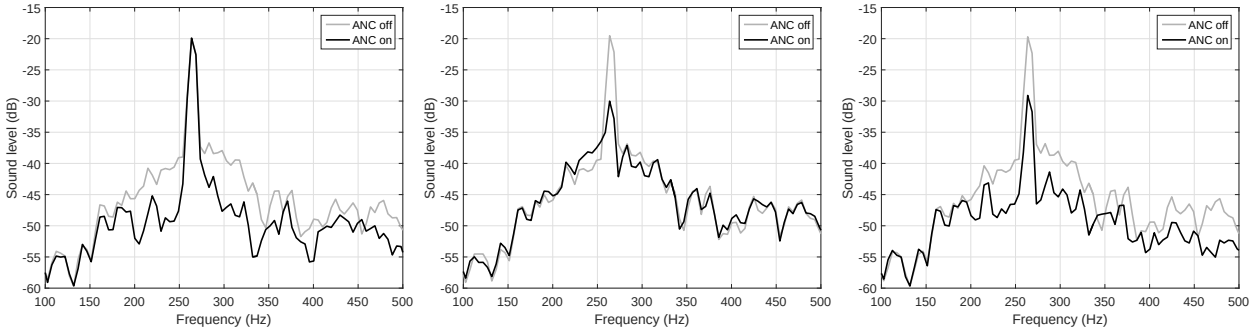

(a) Feedforward (b) Feedback (c) Hybrid

Figure 5.20: Power spectra measured at the right manikin ear.

ditional tone at 265 Hz. This is meant to represent a scenario where the reference signal is only partially correlated with the disturbance. In each case, the virtual microphone arrangement is employed to estimate the signals at the ear microphones.

The power spectra before and after the control has been applied, measured with the manikin head in the nominal position, is shown in Figure 5.20 for feedforward, feedback, and hybrid control architectures. The power spectra correspond to the microphone located in the right manikin ear, although the performance is similar for the left ear. The feedforward controller achieves broadband reductions of 5-10 dB, however, the tone is not attenuated at all because it is uncorrelated with the reference signal. The feedback controller is capable of attenuating the tone by 10 dB. Due to plant delays and the random nature of the disturbance, no significant broadband reductions are observed. The hybrid controller combines the desirable performance associated with each system and is capable of producing broadband attenuations comparable with the feedforward controller while simultaneously attenuating the uncorrelated tone by 10 dB.

Because the virtual microphone arrangement has been used to estimate the pressure at the ear microphones, the spatial extent of the quiet zones will be similar to the corresponding plots shown in the previous section. Figure 5.11-5.12 indicate the spatial extent over which suppression of tonal disturbances can be expected while Figures 5.13-5.14 show similar results for band-limited disturbances. The benefit of employing a hybrid control system is not necessarily improved acoustic performance; it is the ability of the system to attenuate both disturbances for which a correlated reference is available and uncorrelated tonal/narrow-band signals

5.5 Conclusions

The performance of an active headrest system consisting of three control sources, two physical microphones, and two virtual microphones, was studied in this chapter. Initially, the performance was considered in an anechoic environment meant to represent free field acoustic

conditions. The spatial extent of the quiet zone was measured for tonal disturbances as well as disturbances described in terms of one-third octave bands. Multichannel feedforward and feedback control systems were implemented in three configurations:

- Minimize the signals at the physical error sensors (PES)
- Minimize the signals at the virtual error sensors as estimated according to the virtual microphone arrangement (VMA)
- Minimize the signals at the virtual error sensors as estimated according to the remote microphone technique (RMT)

In an anechoic environment and for tonal disturbances, the use of virtual sensors offered improved performance compared to ANC using the physical sensors. Virtual sensing using the remote microphone technique, which uses a matrix of observation filters to estimate the virtual signals, resulted in the best performance, providing 10-15 dB reductions for head movements of ± 3" laterally and forward.

For the one-third octave band disturbances, the feedforward controller outperformed the feedback controller due to the availability of a perfect reference signal. In a feedforward configuration, at least 5 dB integrated reductions were seen for all three techniques for the 250 Hz and 500 Hz one-third octave band disturbances. The remote microphone technique was capable of providing the largest reductions. In a feedback configuration, however, the virtual microphone arrangement performed the best, achieving 5-6 dB integrated reductions for the 250 Hz one-third octave band frequency. The remote microphone technique was only able to achieve 2-3 dB in a feedback configuration due to errors in the matrix of observation filters propagating through the controller and contaminating the reference signals for the feedback filters.

The performance of the headrest was then investigated in a reverberant sound field. Due to the incoherent nature of the sound field, feedforward control was not possible. A well correlated reference signal was unavailable and the resulting noise reductions were hence negligible. In a feedback configuration, the quiet zones generated by controlling the physical error sensors were similar to those obtained using the virtual microphone arrangement. On average, the integrated noise reductions measured in a reverberant sound field were about 1-2 dB less than what was measured in anechoic conditions. This is attributed to the spatially random nature of the sound field and multiple sound wave arrival angles.

In a tonal sound field relatively free from reflections, or a broadband sound field where an accurate reference signal is available, the remote microphone technique offers significant performance benefits relative to cancellation at the physical sensors or virtual sensing using the virtual microphone arrangement. However, if an accurate reference signal is unavailable and feedback control must be used, the virtual microphone arrangement was found to offer the best performance over a practical range of head movements. In a reverberant sound field, the virtual microphone arrangement offered the best performance, although improvements over traditional ANC using physical sensors were marginal.

Chapter 6

Conclusions and Future Work

This dissertation has provided a comprehensive presentation of concepts relevant to the design and analysis of an active noise canceling headrest. The noise canceling capabilities of the headrest was studied through the use of analytical and finite element modeling tools as well as real-time experiments. The main contributions and conclusions drawn from this work are summarized below.

1. Novel control algorithm for combined feedforward-feedback control systems (Chapter 3).
    - Exact update equations, based on the method of steepest descent, for single and multichannel hybrid control systems were presented.
    - The exact update equation was found to contain a term that is a recursive function of the plant modeling error and provides insight into the effects that modeling error has on an adaptive hybrid control system.
    - When an accurate estimate of the modeling error is available, as may be the case when the uncertainties are structured in nature, the exact solution provides moderately faster convergence relative to the approximate solution used in the filtered reference least mean squares algorithm. In most other cases, when the modeling error is unknown, the exact and approximate solutions result in similar performance.
2. Development of an active headrest finite element (FE) model to allow evaluation of various headrest configurations/parameters (Chapter 4).
    - Using the FE model, effects of adding additional secondary sources as well as physical and virtual sensors were easily investigated.
    - It was found that, without varying the geometry/form-factor of the active headrest, a three loudspeaker configuration performs comparably to systems with more secondary sources. This conclusion is drawn based upon the specific geometry, actuator/sensor placement, and virtual sensing approaches considered here.

- For the geometrical arrangement of loudspeakers and error microphones considered in this study, it was shown that the attenuation and spatial extent of the quiet zone can be drastically improved by using virtual sensors to shift the cancellation point toward the ears. Although the remote microphone technique, which accounts for the response between the physical and virtual microphones, results in the greatest attenuation at the ears, the spatial extent of the 10 dB quiet zone is largely similar to that computed using the virtual microphone arrangement due to the uniform radiation pattern of the secondary sources at low frequencies. It was also concluded that minimizing the pressure over arrays of closely spaced virtual error sensors results in degraded performance due to the issue of collinearity.
- Headrest performance in primary sound fields consisting of individual plane waves was compared to performance in diffuse primary sound fields. It was shown that the overall attenuation as well as the spatial extent of the quiet zone were degraded in spatially random pressure fields. Although virtual sensors helped to improve the attenuation in a diffuse sound field, the range of head movements over which at least 10 dB of attenuation could be expected was significantly less as compared to a plane wave primary sound field.
- When the primary sound field is predictable, *e.g.*, a plane wave, and an accurate estimate of the response between the physical and virtual microphones can be formed, the remote microphone technique results in the best performance. When the sound field is spatially random, however, and the relationship between the physical and virtual microphone is described in a statistical sense, the virtual microphone arrangement was found to provide the best performance.
- For the headrest geometry/form-factor considered in this study, the best acoustic performance was achieved for a system consisting of three loudspeakers and two virtual error sensors. The three loudspeaker configuration was found to perform better than many previously proposed active headrests, which mimic the arrangement of active headsets by using a single loudspeaker for each ear.

3. Design and construction of an active headrest prototype for real-time testing of multichannel adaptive control systems (Chapter 5).

    - Adaptive multichannel feedforward and feedback control systems were initially tested in anechoic conditions for tonal primary sound fields. The feedforward and feedback controllers resulted in similar attenuation since an adaptive feedback controller is capable of perfectly canceling tonal disturbances. In this simple sound field, the remote microphone technique provided the best attenuation because the amplitude and phase relationship between the physical and virtual microphones could be accurately modeled for a given frequency.
    - The active headrest control systems were tested in both anechoic and fully reverberant conditions for band-limited primary sound fields. In anechoic conditions, the feedforward controller provided the best attenuation due to the availability of

a time-advanced reference signal. In a reverberant sound field, however, a well-correlated reference signal was unavailable and feedforward control resulted in negligible attenuation. When feedback control was employed, the virtual microphone arrangement resulted in the best performance. The remote microphone technique, when used in a feedback setting, was found to be ineffective in canceling band-limited disturbances. This is due to the fact that a causal digital filter that accurately described the relationship between the physical and virtual microphones could not be realized.

- It was shown that combined feedforward-feedback, or hybrid, control systems offer improved performance relative to solely feedforward or feedback systems in certain situations. In scenarios where the primary disturbance contains both correlated and uncorrelated spectral components, hybrid control systems provide a distinct performance advantage. In a real-time test of the multichannel active headrest control system, it was shown that a hybrid control system is capable of attenuating disturbance components for which a correlated reference is available as well as uncorrelated tonal disturbances.
- It is concluded that a multichannel adaptive feedback control system is capable of attenuating band-limited disturbances over a practical range of listener head movements.

The above summarizes the conclusions and overarching contributions of this work, although smaller contributions have been noted and can be found throughout the dissertation. Altogether, this dissertation serves to provide a comprehensive analysis of active headrest systems. Both real-time control system implementation as well as investigations of the local acoustic environment in an active headrest were extensively studied using finite element tools as well as real-time experiments. A significant amount of attention was paid to the concept of virtual sensing and some new results and insights into the benefits and limitations associated with using this approach were presented and studied.

6.1 Future work

Active headrests have been successfully demonstrated in numerous academic studies, yet their use in practical applications is extremely limited. This is mainly due to the fact that the quiet zones generated using loudspeakers of practical sizes are very small and do not follow the ears of an occupant as the head is moved. The following list provides some interesting new research directions that may help to alleviate this issue and make active headrests a viable solution for improving personal acoustic environments in loud or noisy vehicles.

- Topological optimization of an active headrest. Begin by defining a design space limited by the number and placement of actuators and sensors as well as some geometrical con-

straints. Using a platform to rapidly evaluate the acoustic performance, such as the FE modeling tool described in this dissertation, employ a genetic algorithm or comparable search routine that finds an *optimal* headrest geometry in the design space that maximizes the quiet zone over a predefined range of head movements and maximizes the attenuation for the nominal head position.

- Methods of significantly reducing the hardware delay such that feedback systems can provide a greater degree of attenuation (perform ANC on field programmable gate arrays).
- Application-specific active headrests. For instance, an active headrest applied to a rotorcraft could use a tachometer as a reference transducer and potentially achieve appreciable reductions in the blade passage frequency.

Appendix A

The effects of room modes on controller performance

The initial objective of testing in the reverberation chamber was to quantify the spatial extent of the quiet zones in tonal diffuse sound fields. After a series of initial tests, it was determined that tonal diffuse sound fields, at least for the low frequencies at which ANC in a headrest is realistic, were not realizable in the reverberation chamber in the NASA Langley Structural Acoustics Loads and Transmission (SALT) facility. This appendix provides some details regarding the room diffusivity and a justification for using band-limited disturbances as opposed to pure tones.

A.1 Reverberation chamber diffusivity

The purpose of testing in the reverberation chamber is to quantify the acoustic performance of the active headrest in a diffuse sound field. A discussion on the diffusivity of the room is therefore necessary to fully understand the experimental results. The information in this section can also be found in [111], in which a detailed characterization of the reverberation chamber was presented, but is reproduced here due to it's importance in understanding the test results.

At low frequencies, the acoustic response of a room can be described using a modal approach, where the different room modes are well separated in frequency. At higher frequencies the modes begin to overlap, until above a certain frequency, which is determined by characteristics of the room, the modal density is large enough such that the sound field can be treated in a statistical sense. In this case the sound field is referred to as diffuse. In a diffuse sound field, there is an equal probability of acoustic energy flowing in all directions. The diffusivity of the room is influenced by factors such as the acoustic modal response, the chamber volume, and the chamber dimension ratios.

Several different standards have been suggested to ensure the diffusivity of a reverberation chamber. For example, the International Standard ISO 3741 has suggested that a minimum chamber volume of 200 m^3 is necessary for diffuse field measurements down to the 100 Hz one-third octave band, whereas the ISO 354 standard requires that

$$I_{max} < 1.9V^{1/3}, \tag{A.1}$$

where I_{max} is the longest straight line dimension of the chamber and V is the chamber volume. Other standards regarding the number of modes present in a given one-third octave band as well as the required frequency spacing of room modes for a diffuse field have been proposed in [113, 114]. Perhaps the most common measure of when a field may be considered diffuse is given by the Schroeder cut-off frequency [115]

$$f_s = \sqrt{\frac{c^3 T}{4\ln 10 * V}}, \tag{A.2}$$

where c is the sound speed and T is the chamber reverberation time. Table A.1, which is adapted from [111], shows the variation in the Schroeder cut-off frequency as a function of mean reverberation times for each one-third octave band. This indicates that below about 400 Hz, the room response is characterized by a finite number of acoustic modes and cannot be treated as diffuse. Furthermore, since the mean reverberation times in Table A.1 correspond to a primary sound field with frequency content in various one-third octave bands, it follows that most of the modes in the corresponding one-third octave band will be excited. In contrast, if the primary sound field is a single tone, only the room mode at that specific frequency will be excited, as opposed to all modes in a given one-third octave band. Since the diffusivity of the sound field depends directly on the number of modes present in the room, we can expect that mean reverberation times computed assuming primary sound fields with frequency content in various one-third octave bands will be longer (*i.e.*, a more diffuse field) than mean reverberation times computed assuming a tonal primary sound field. In accordance with this reasoning, the values in Table A.1 that indicate the lower frequency bound where the field can be treated as diffuse are likely lower than the lower frequency bounds if the primary sound field was a single tone. This implies that for a single frequency, the field is modally dominated for single frequencies even greater than 400 Hz. To generate a tonal diffuse field at frequencies lower than about 500 Hz, a reverberation chamber with larger dimensions would be required.

Table A.1: Schroeder cut-off frequencies as a function of the mean reverberation times.

One-third octave band center frequency (Hz)	**Reverberation Time (s)**	**Schroeder cut-off frequency (Hz)**
80	14.81	483.2
100	12.81	449.4
125	13.14	455.0
160	13.61	463.2
200	12.41	442.2
250	10.95	415.5
315	10.44	405.6
400	9.79	392.7
500	8.13	358.0
630	7.65	347.3
800	6.70	324.8
1000	6.19	312.3

The modal acoustic response of the room was observed in many of the tests as a significant variation in the sound level at different microphone locations, namely the two microphones located in the manikin ears. Figure A.1 shows the magnitude of the primary disturbance measured over 100 separate tests for three frequencies. The mean and standard deviation are also shown in the figure. In each test, four acoustic sources were driven with tonal signals and random phases. Because of this, the modal structure in the room also changed from test to test. If the tonal frequency exceeds the Schroeder frequency, a diffuse field representation can be formed by averaging over space. To clarify, the sound field in the reverberation room is still composed of modes, with numerous peaks and valleys. The sound pressure level is hence *not* constant at every point. However, the sound pressure integrated over a sufficiently large space *would* be constant [116].

The effect that this had on the control system was that very erratic noise reductions were obtained seemingly arbitrarily. For instance, it can be seen that for test 44 at 300 Hz, the left ear microphone is clearly located near a node of the sound field. This resulted in large signal amplifications at this microphone when control was applied. The use of disturbances described in terms of one-third octave bands for the most part remedied this problem. With a finite bandwidth primary field, a larger amount of room modes were excited, leading to a more diffuse sound field.

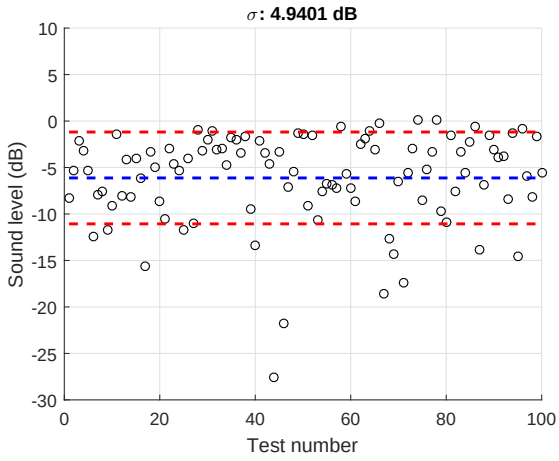

(a) 300 Hz: Left ear microphone

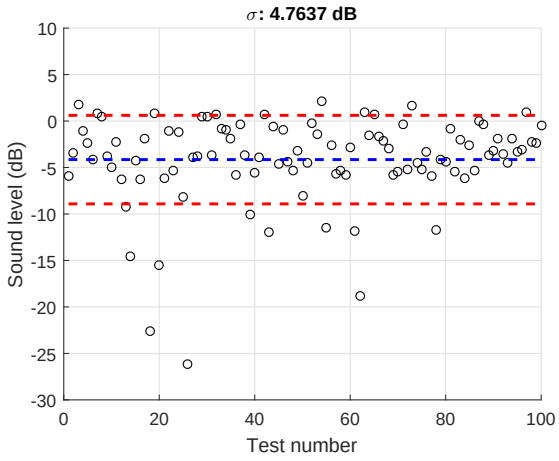

(b) 300 Hz: Right ear microphone

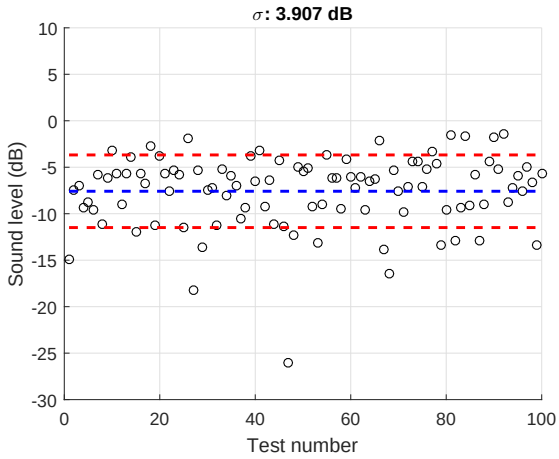

(c) 500 Hz: Left ear microphone

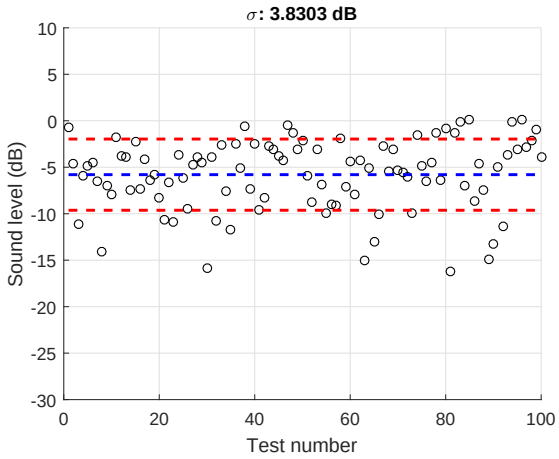

(d) 500 Hz: Right ear microphone

(e) 700 Hz: Left ear microphone

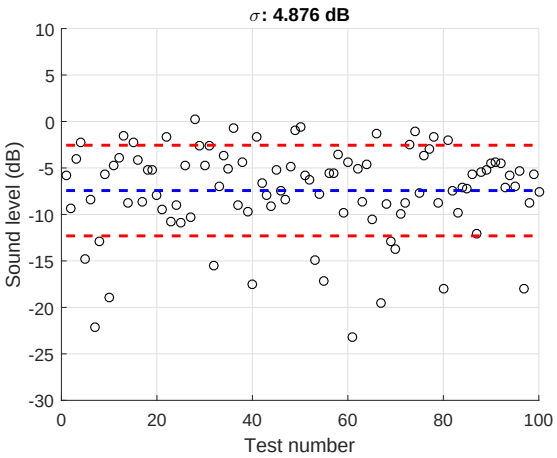

(f) 700 Hz: Right ear microphone

Figure A.1: Primary sound field variation for multiple realizations.

Appendix B

Headrest Acoustic Performance Simulations

In Chapter 4, some results corresponding to plane wave primary sound fields were presented, however, the main focus was on diffuse sound fields. In this appendix, a more comprehensive description of the performance of the active headrest in plane wave primary fields is provided. Also mentioned in Chapter 4 was that the relative geometry of the active headrest plays a large role in the acoustic performance. With this in mind, simulation results corresponding to an alternate headrest geometry are included here. In this new geometry, the angles of the side speakers are adjusted so that they directly face the ears. In this case, the active surface of the two secondary sources on the side are perfectly aligned with the control and virtual microphones.

B.1 Plane wave primary field

In each simulation, the uniform field is generated by assuming that the disturbance is a plane wave traveling in the $+x$ direction. In general, the zones of quiet generated in a uniform primary field are larger than for the diffuse field case. Nonetheless, these simulations should provide guidelines for the expected performance if a headrest of similar geometry is tested in an anechoic environment.

Figures B.1-B.4 can be compared with Figures 4.11-4.14 in Chapter 4 to gain insight into the performance differences in plane wave and diffuse primary sound fields. As discussed in the chapter, the size and shape, as well as the attenuation at the virtual locations, are significantly degraded in diffuse sound fields. In Figures B.1 and B.3, the control sources are adjusted to cancel the pressure at the control microphones. In Figures B.2 and B.4, however, the virtual pressures, estimated according to the virtual microphone technique, are minimized. This is again seen to offer a dramatic improvement in the acoustic performance of the active headrest.

It was mentioned earlier that the size and shapes of the quiet zones are heavily influenced by the relative geometry of the secondary sources and microphones relative to the head. Here, the

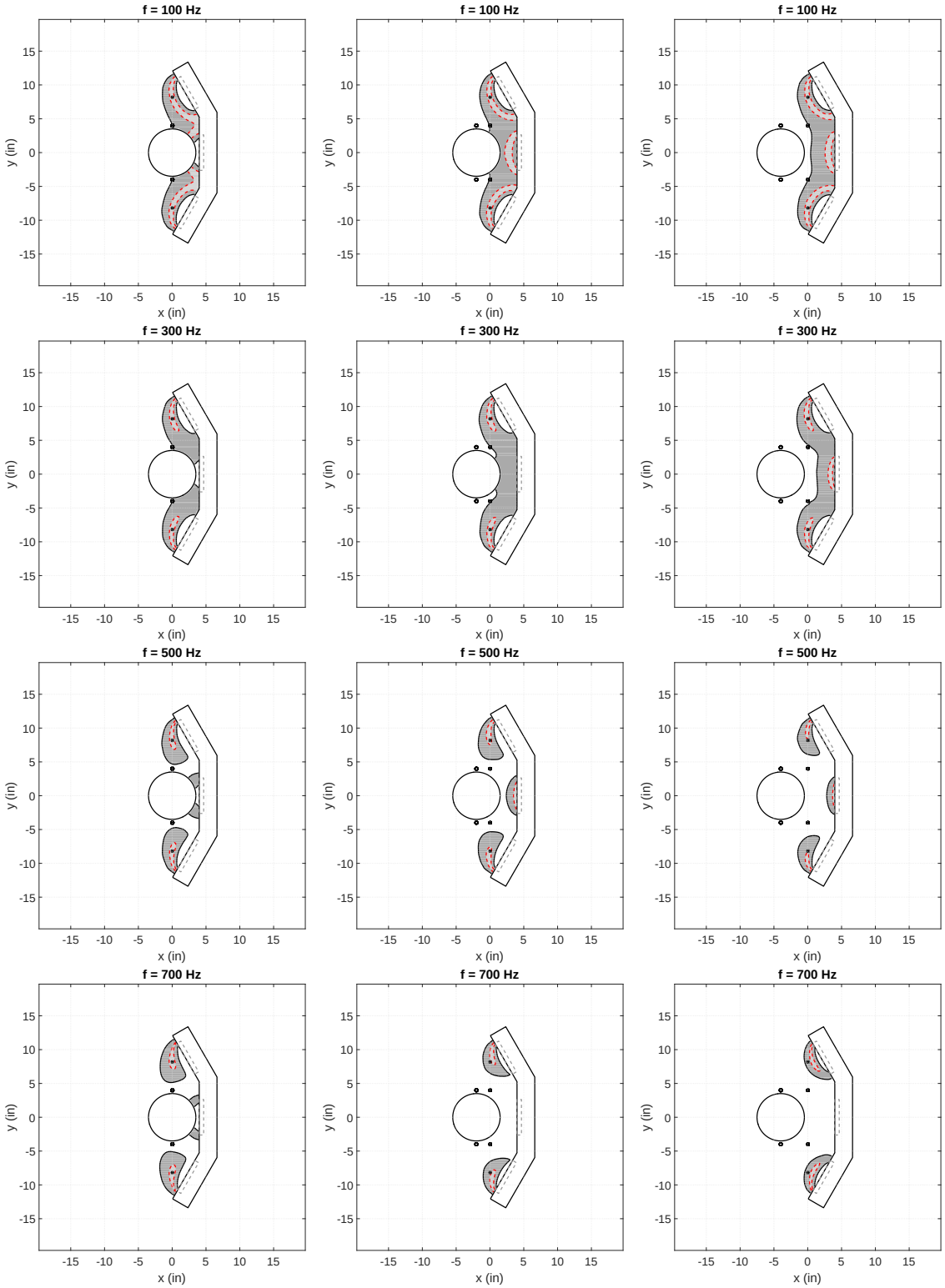

Figure B.1: Cancellation at control microphones in a plane wave primary field for forward head positions of $x = 0$", 2", and 4".

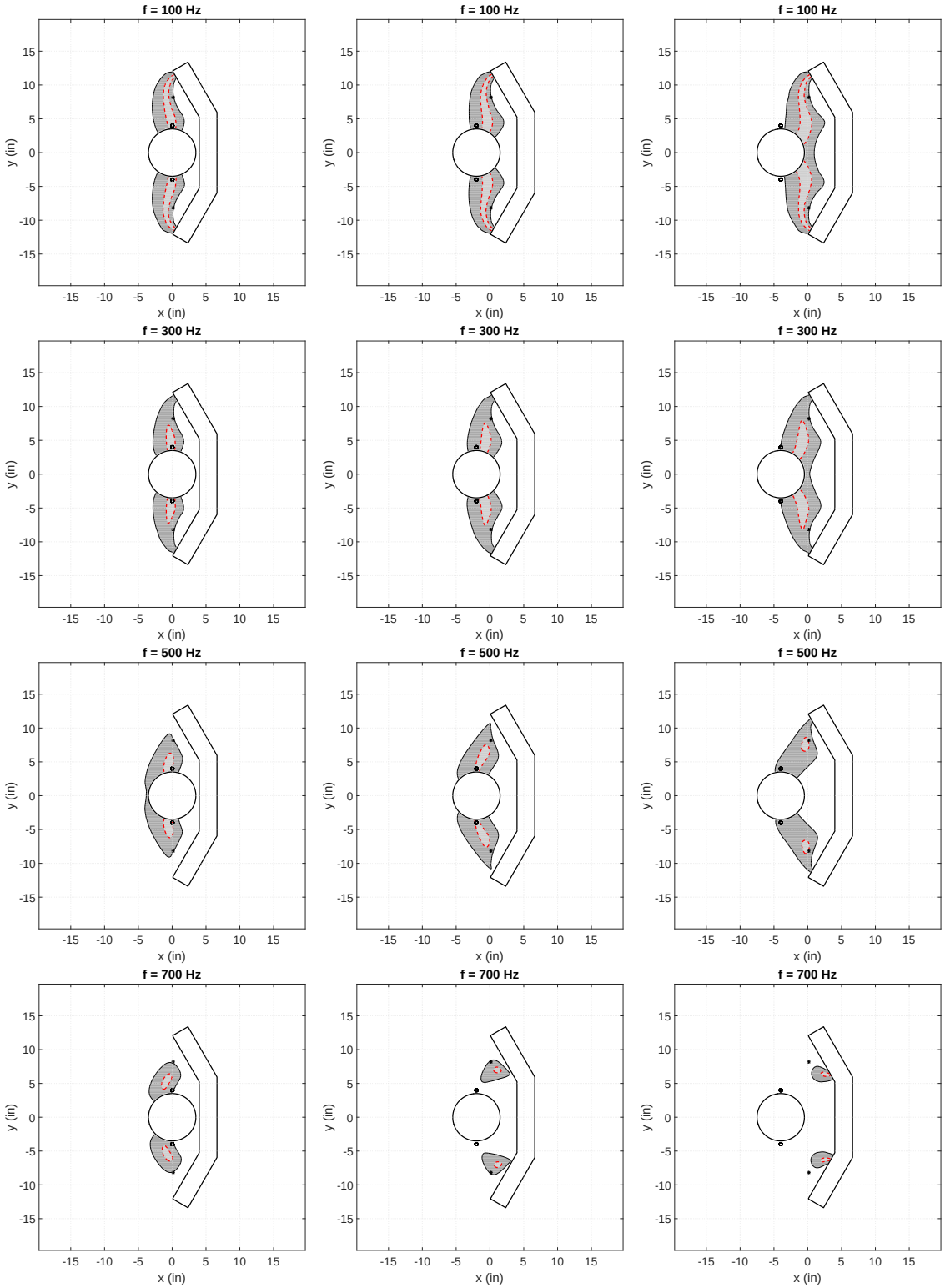

Figure B.2: Minimizing the virtual error signals estimated according to the virtual microphone arrangement in a plane wave primary field for forward head positions of $x = 0$", 2", and 4".

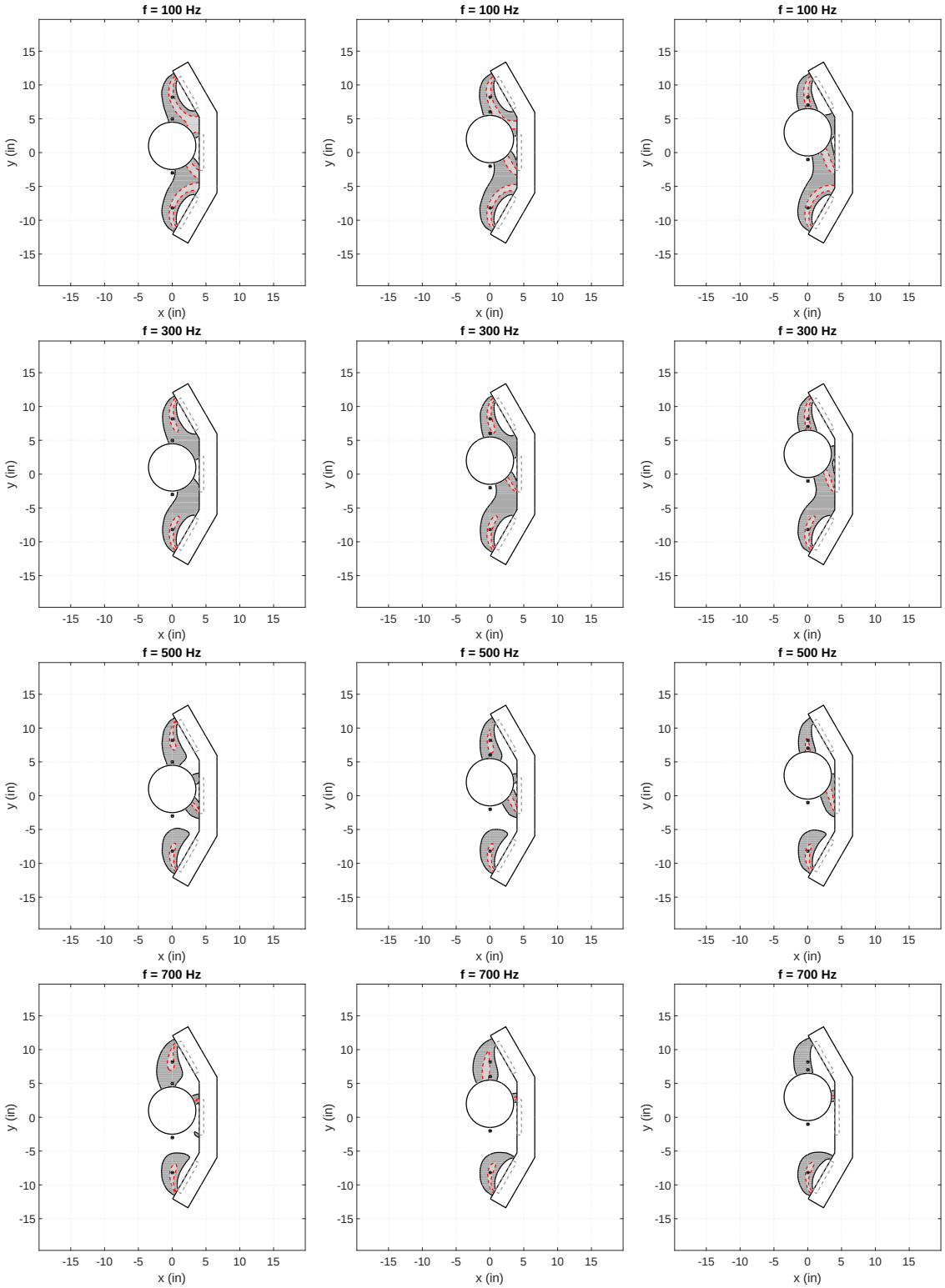

Figure B.3: Cancellation at control microphones in a plane wave primary field for lateral head positions of $y = 1"$, $2"$, and $3"$.

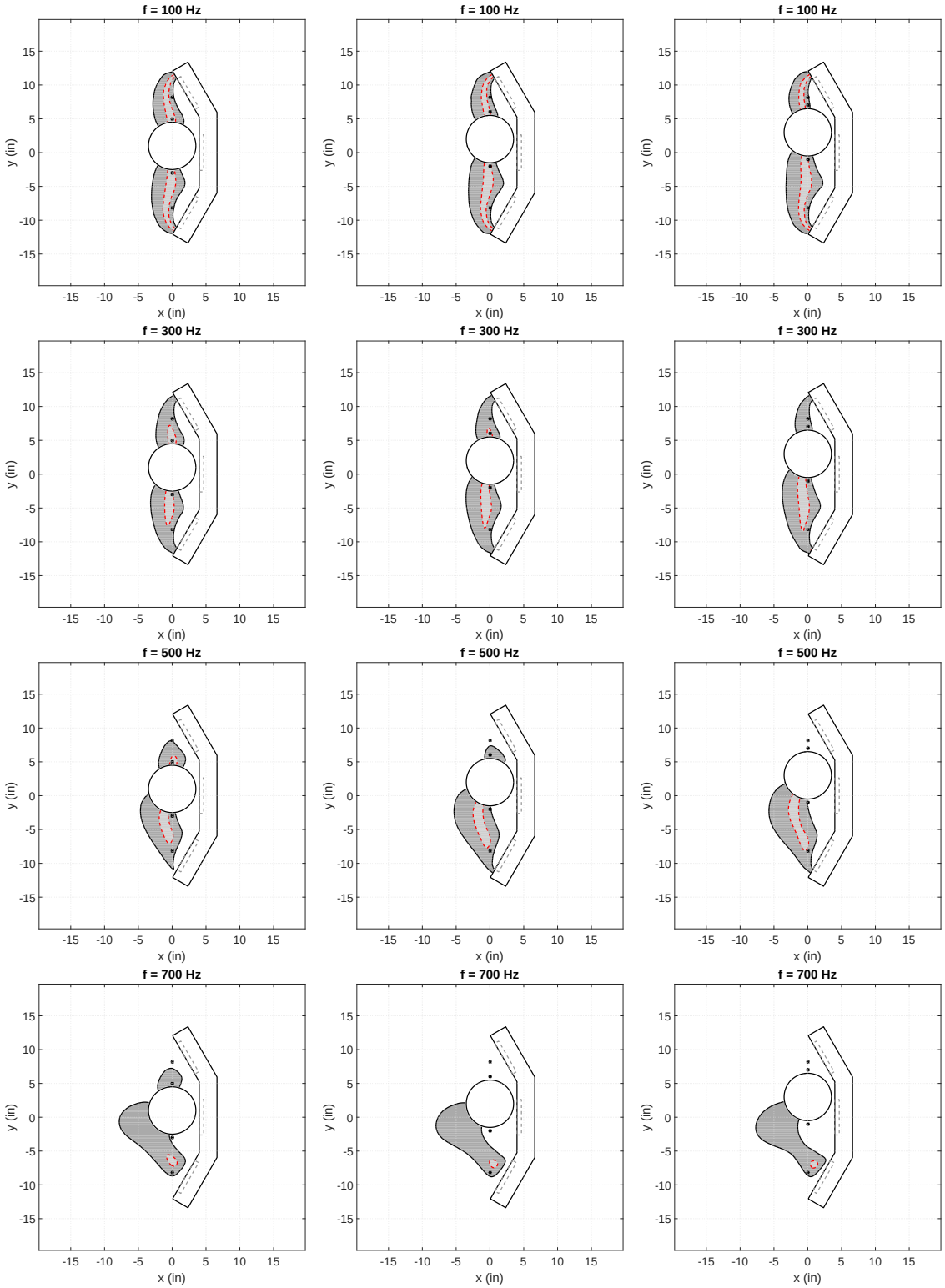

Figure B.4: Minimizing the virtual error signals estimated according to the virtual microphone arrangement in a plane wave primary field for lateral head positions of $y = 1"$, $2"$, and $3"$.

geometry of the headrest is adjusted so that the secondary sources to either side of the head directly face the virtual microphones. The spatial extent of the quiet zones are shown for this new geometry in Figure B.5-B.8. Comparing Figures B.5-B.8 with Figures B.1-B.4, it is apparent that, when virtual sensors are used in the control system, the attenuation at the ears can be improved by choosing the geometry such that the axis of symmetry of the secondary sources aligns with the ears. This finding is confirmed by prior work documenting the behavior of quiet zones near diffracting surfaces [17] and on the off-axis of baffled pistons [108, 117].

B.2 Diffuse field simulations

The quiet zone plots shown in Figures B.9-B.12 are meant to complement the diffuse field simulation results presented in Chapter 4, except for a different geometry. Again it can be seen that the new geometry improves the spatial extent of the quiet zone for diffuse fields as well. For instance, in the original headrest geometry presented in Chapter 4, the attenuation does not reach 10 dB for a 700 Hz primary disturbance. With the new geometry, the attenuation as well as the size of the quiet zones are much improved. The spreading of the quiet zone, which is due to the zero pressure gradient enforced by the presence of the rigid head, is quite apparent in this new geometry.

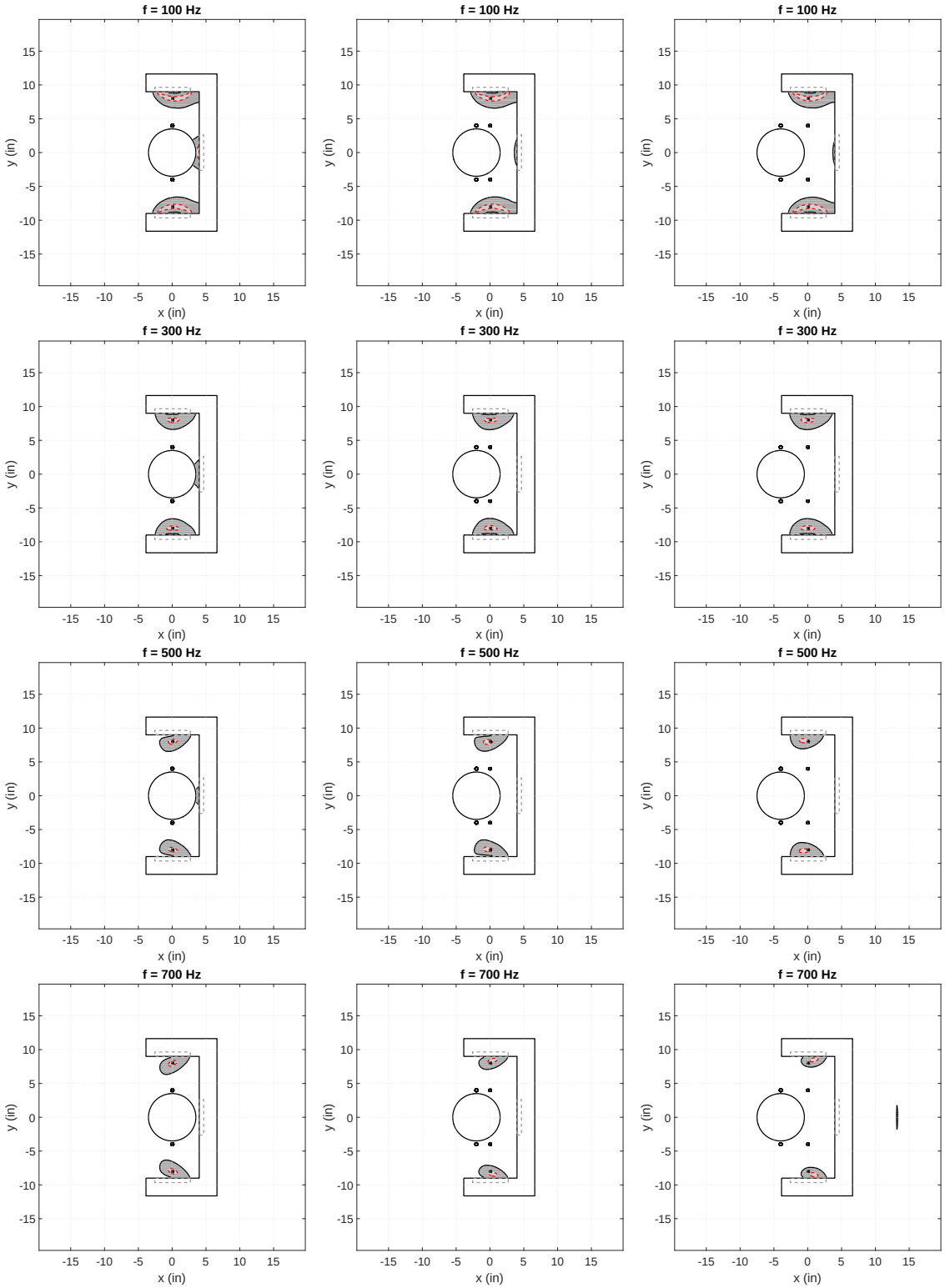

Figure B.5: Cancellation at control microphones in a plane wave primary field for forward head positions of $x = 0$", 2", and 4".

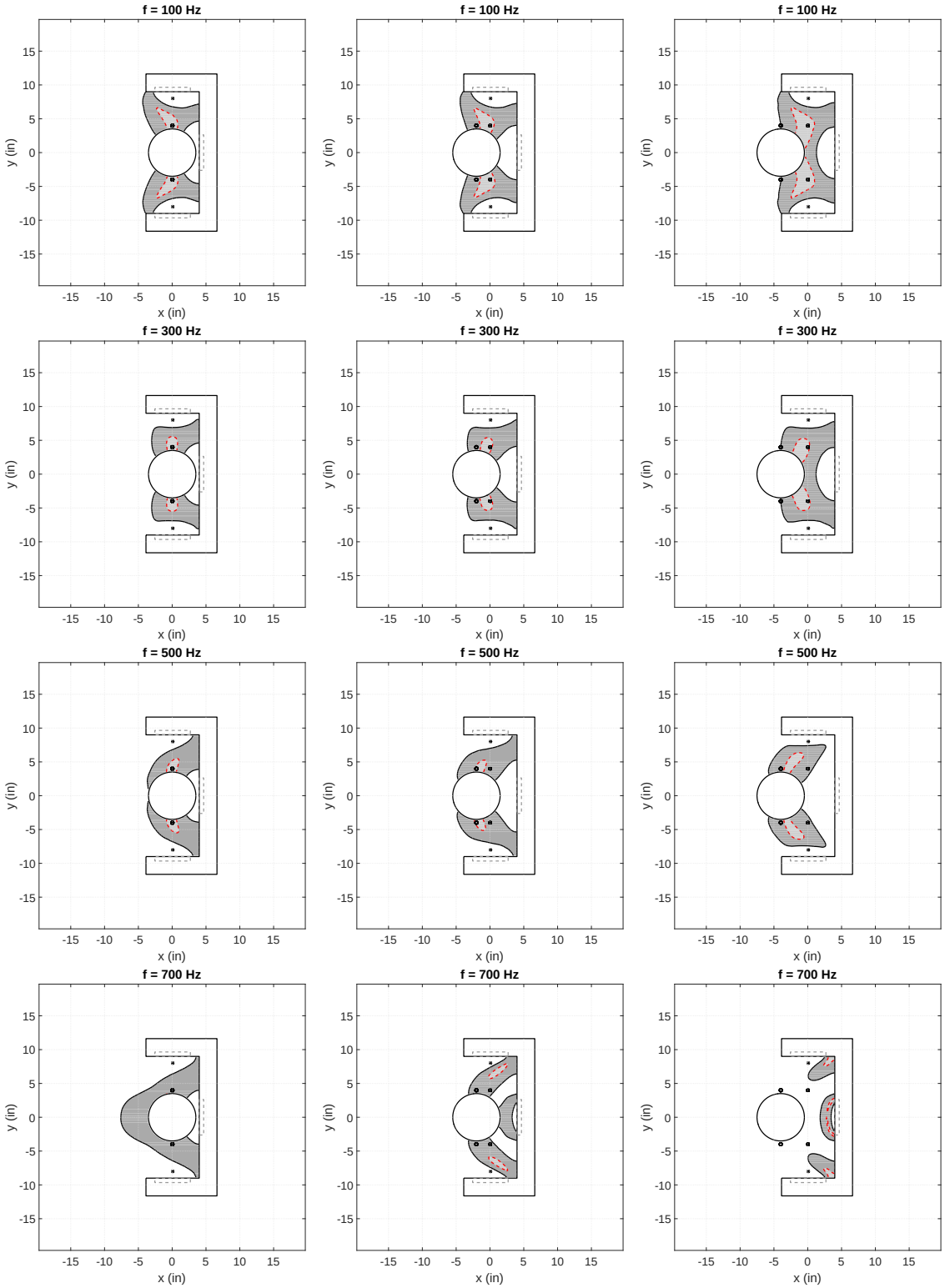

Figure B.6: Minimizing the virtual error signals estimated according to the virtual microphone arrangement in a plane wave primary field for forward head positions of $x = 0$", 2", and 4".

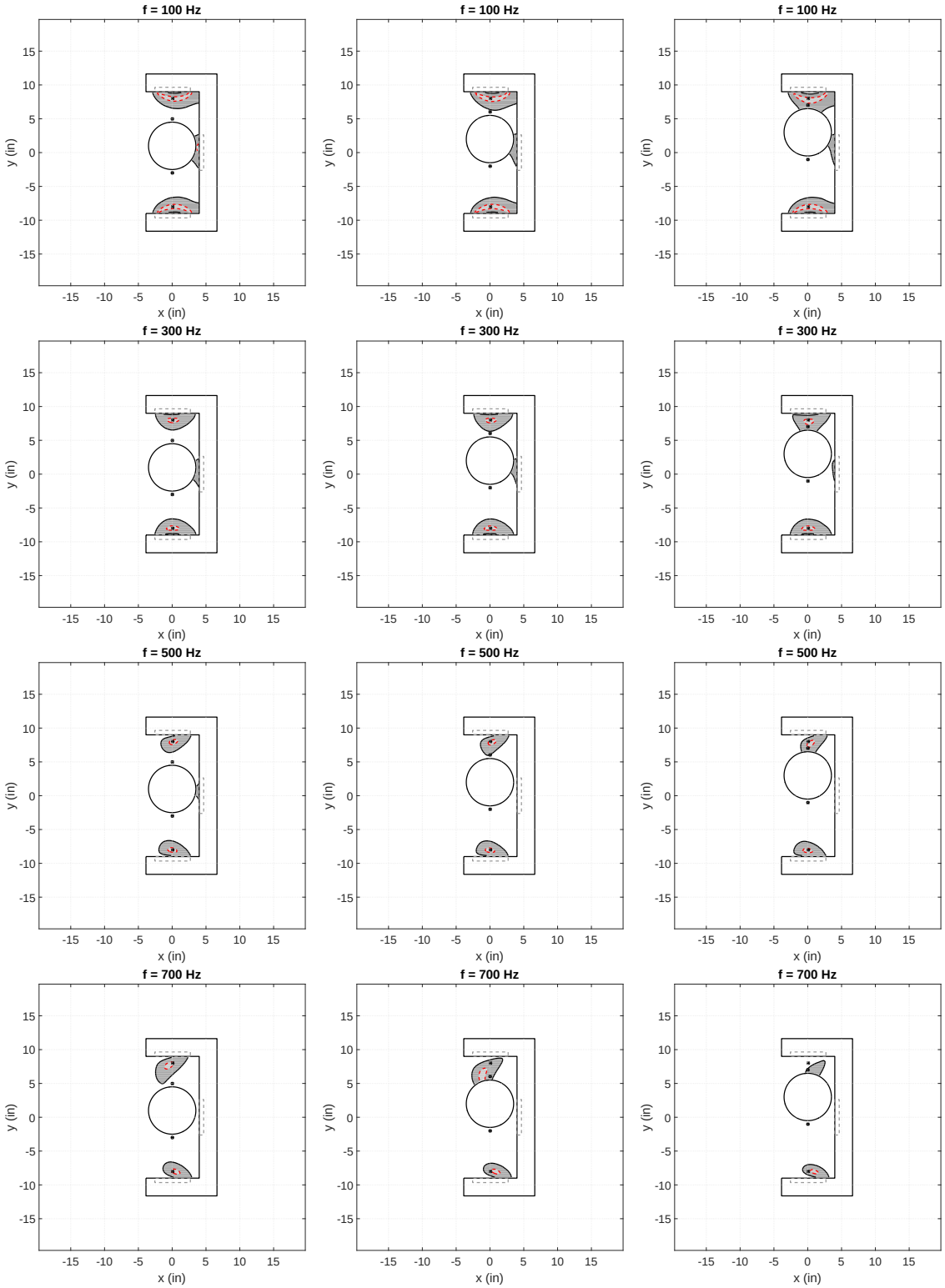

Figure B.7: Cancellation at control microphones in a plane wave primary field for lateral head positions of $y = 1"$, $2"$, and $3"$.

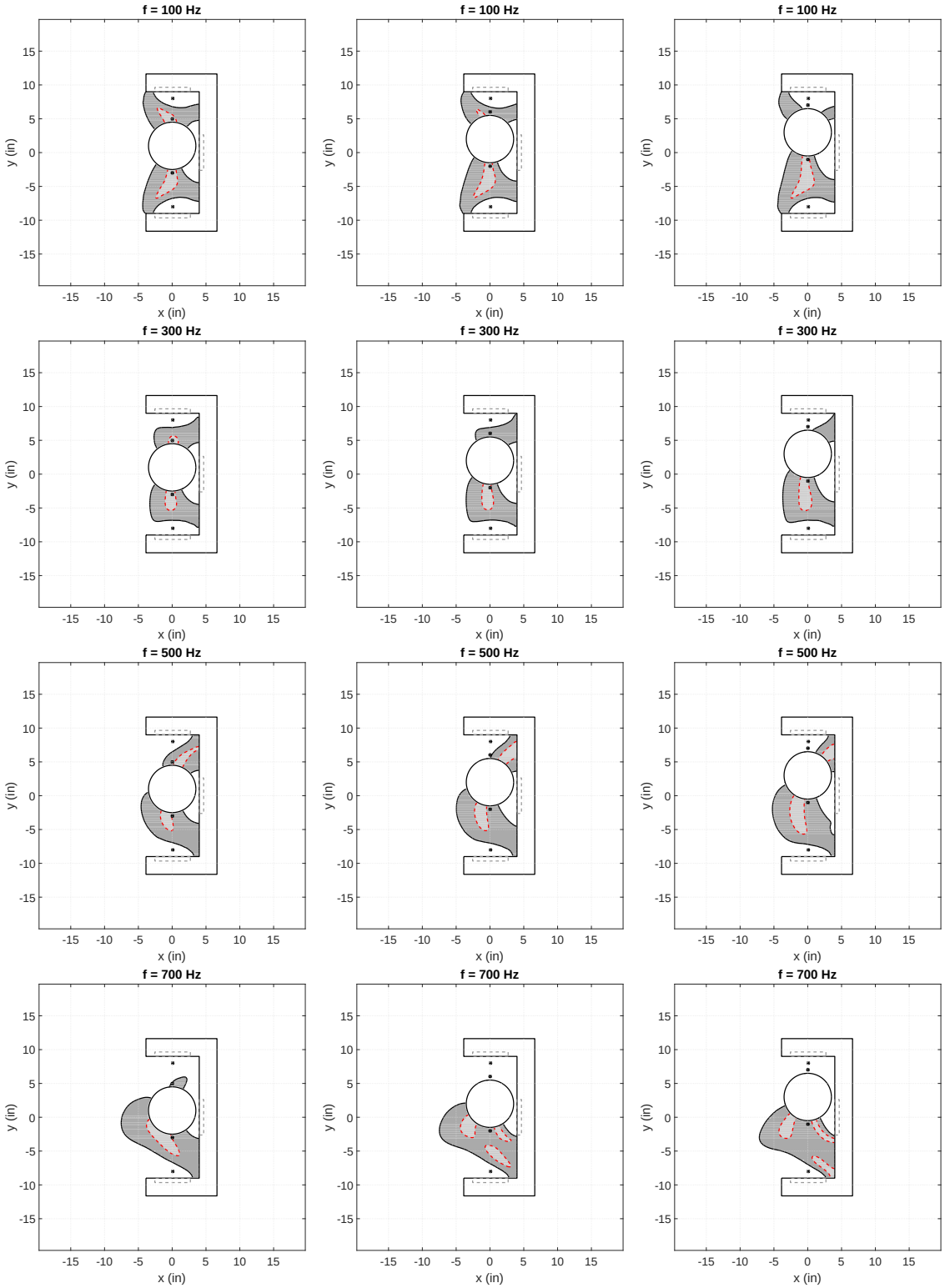

Figure B.8: Minimizing the virtual error signals estimated according to the virtual microphone arrangement in a plane wave primary field for lateral head positions of $y = 1"$, $2"$, and $3"$.

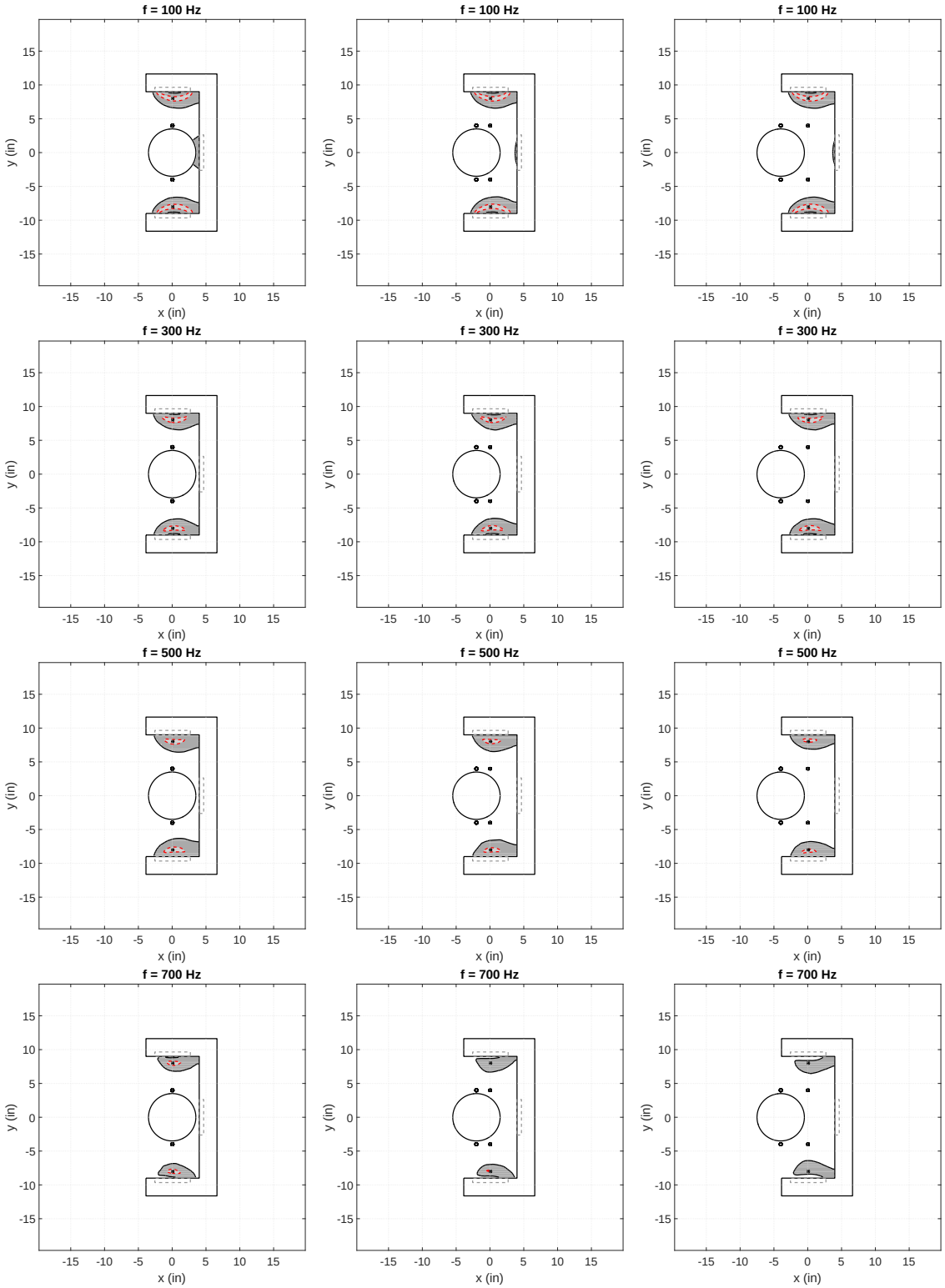

Figure B.9: Cancellation at control microphones in a pure tone diffuse field for forward head positions of $x = 0$", 2", and 4".

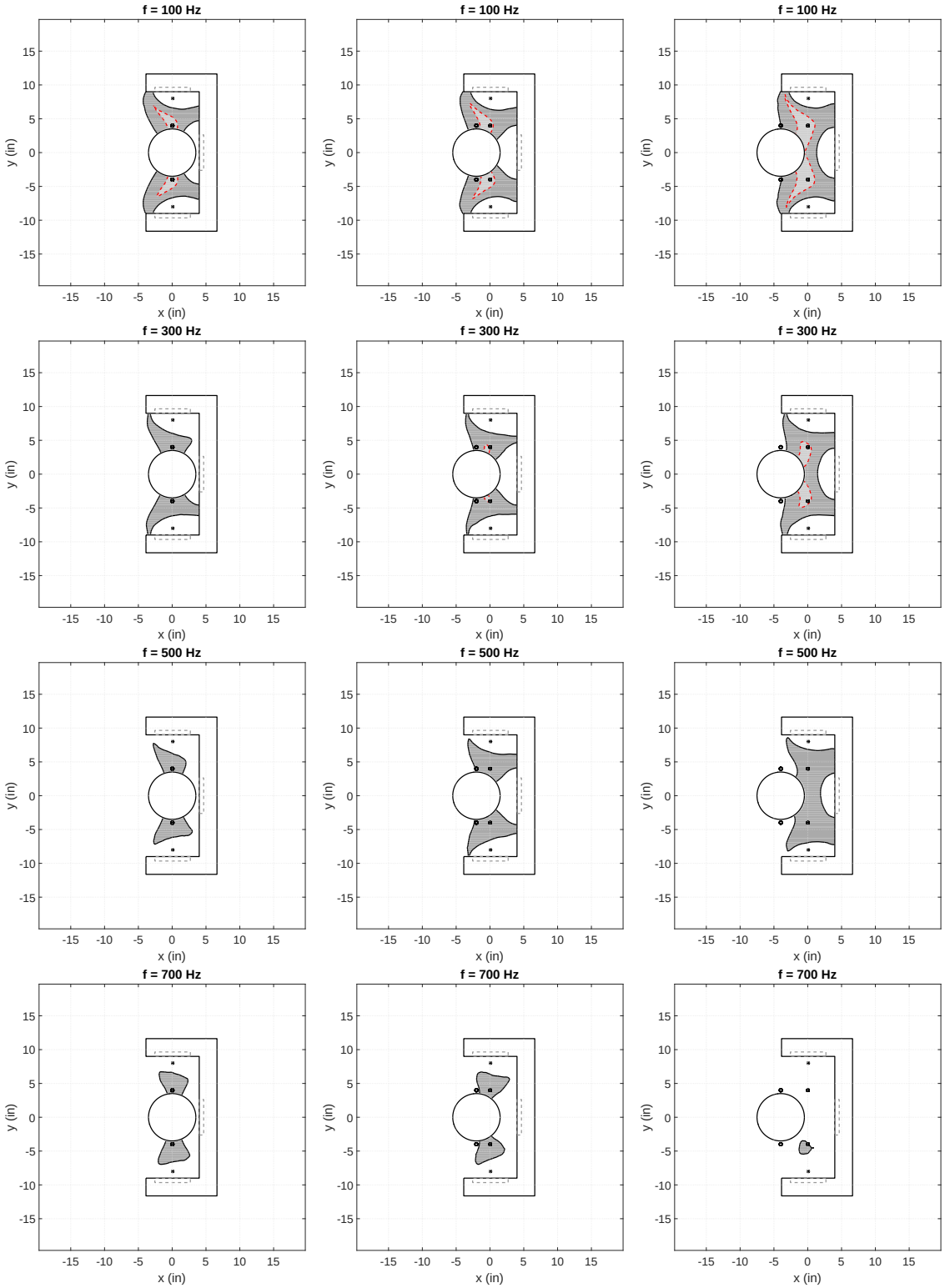

Figure B.10: Minimizing the virtual error signals estimated according to the virtual microphone arrangement in a pure tone diffuse field for forward head positions of $x = 0$", 2", and 4".

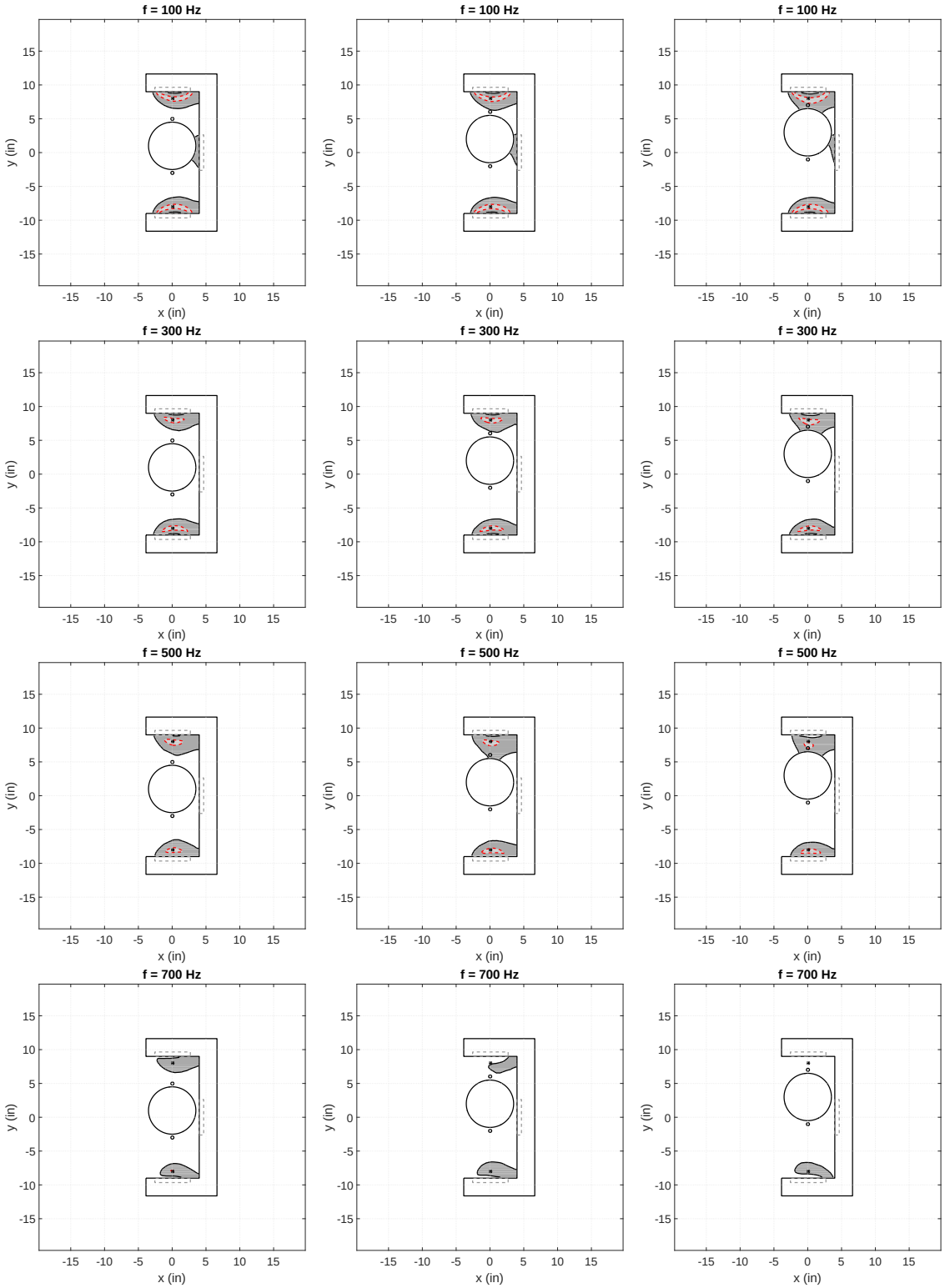

Figure B.11: Cancellation at control microphones in a pure tone diffuse field for lateral head positions of $y = 1"$, $2"$, and $3"$.

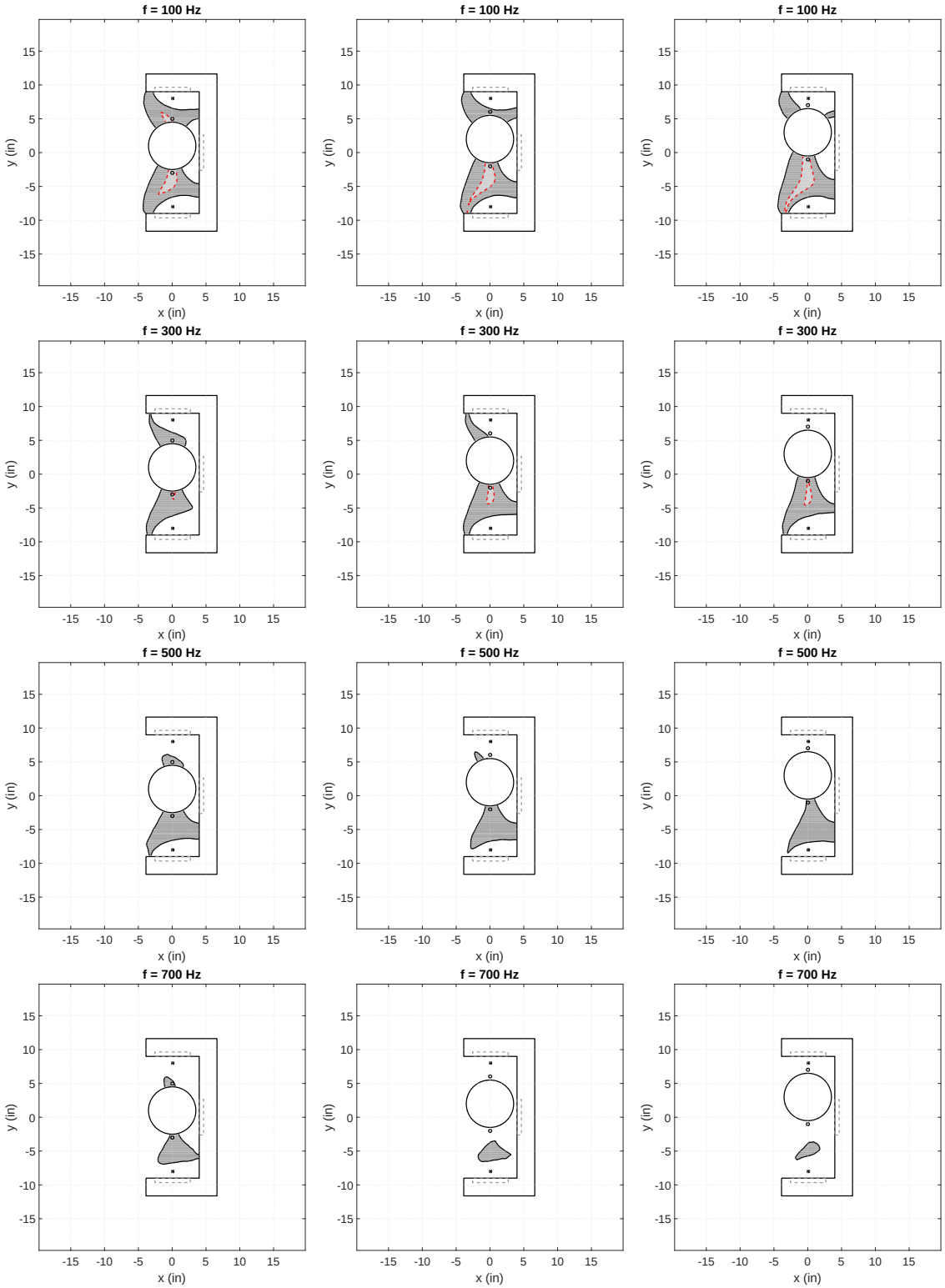

Figure B.12: Minimizing the virtual error signals estimated according to the virtual microphone arrangement in a pure tone diffuse field for lateral head positions of $y = 1"$, $2"$, and $3"$.

Appendix C

A single channel hybrid control experiment using virtual sensors

In this appendix, the results of a single channel hybrid control experiment using a virtual microphone are presented. An initial objective of this research project was the combination of feedforward and feedback control, hence this is included mainly for completeness. The first section provides simulation details. Results of the real-time control experiment are then subsequently presented. Single channel feedforward, feedback, and hybrid control architectures are compared to illustrate the advantages and limitations of each approach.

A diagram of the experimental setup is shown in Figure C.1. The primary sound field is generated by the primary source and the secondary source is used to control the local sound field. A reference microphone is located directly in front of the primary source such that a well correlated reference is available to the control system. A physical microphone, where initially the primary sound will be minimized, is located in the vicinity of the secondary source. A third microphone, which will be referred to as the virtual microphone, is located several inches away from the physical microphone. The virtual microphone is not used in the operation of the control system, but is present to monitor control performance and examine the ability of the control system to shift the quiet zone away from the physical microphone and towards the virtual microphone.

C.1 Simulation

In the first simulation, each controller aims to minimize the error signal directly measured at the virtual microphone. This represents the case where we are able to place an error microphone directly at the desired point of cancellation. The disturbance is chosen to consist of two components: a filtered version of the reference noise and a narrow-band signal $v_{nb}(n)$ that is

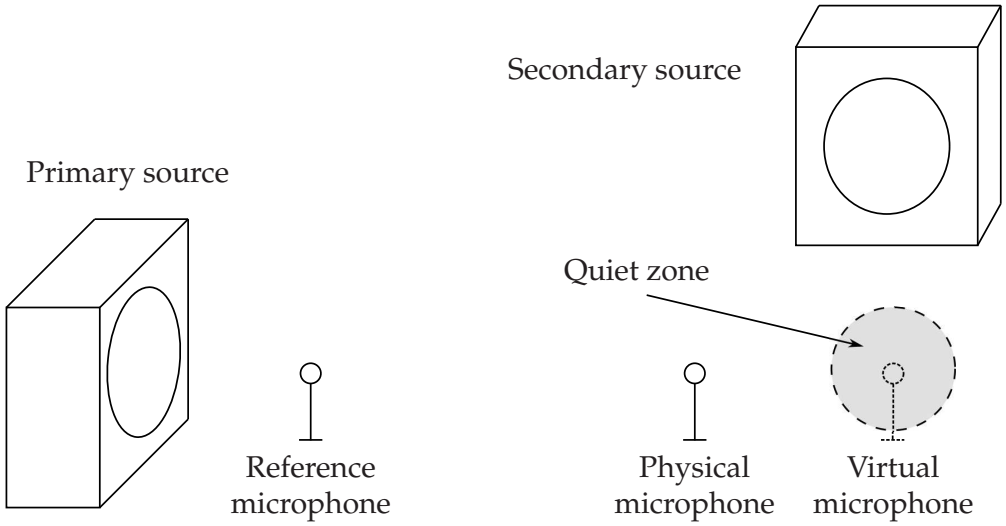

Figure C.1: Diagram of the single channel active noise control experiment.

uncorrelated with the reference,

$$d(n) = P(z)x(n) + v_{nb}(n). \tag{C.1}$$

The reference noise $x(n)$ consists of a broadband component and a sinusoid with frequency ω_1. The quantity $v_{nb}(n)$ is a sinusoid with frequency ω_2. Thus, the disturbance will consist of a broadband and a narrow-band signal, which are correlated with the reference, as well as an uncorrelated narrow-band component $v_{nb}(n)$. This condition represents a scenario in which the reference sensor is unable to observe part of the narrow-band noise. The frequencies are chosen arbitrarily as ω_1=150 Hz and ω_2=225 Hz.

Results of computer simulations for each control system are shown in Figure C.2. As expected, the feedforward controller is capable of attenuating only the disturbance that is correlated with the reference. The uncorrelated narrow-band disturbance at ω_2=225 Hz is minimally reduced. The feedback controller, which makes no use of the reference signal, is capable of attenuating both narrow-band disturbances. No broadband attenuation is achieved due to the random nature of the signal. The hybrid controller outperforms both the feedforward and feedback controllers, canceling both the disturbance correlated with the reference as well as the uncorrelated narrow-band disturbance. In situations where a noise source is not easily identifiable or measurable, hybrid control structures offer significant performance advantages over the traditional feedforward and feedback approaches.

In the second set of simulations, it will be assumed that we do not have direct access to the virtual microphone signal and it must be estimated based on the physical microphone signal. In these simulations, the remote microphone technique [77] is used to perform this estimation task. The reference and disturbance signals are the same as in the first simulation. The results of the simulation are shown in Figure C.3. The overall behavior is similar to if the virtual

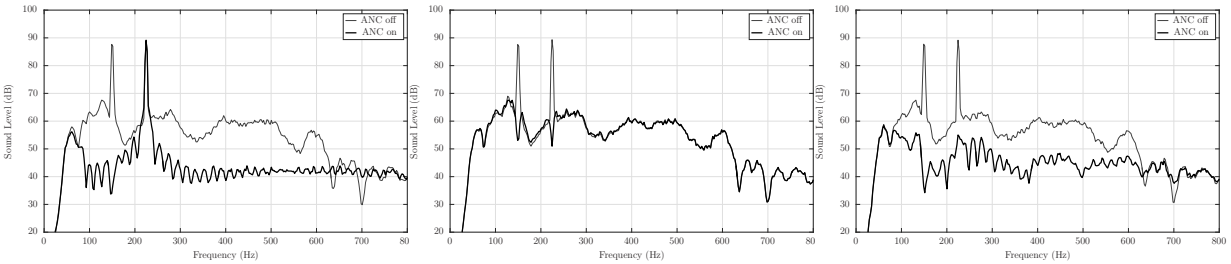

Figure C.2: Simulation results for feedforward, feedback, and hybrid control structures. The reference signal consists of a 150 Hz tone and a broadband signal. The disturbance is the reference signal filtered through $P(z)$ plus an uncorrelated sinusoid of frequency 225 Hz.

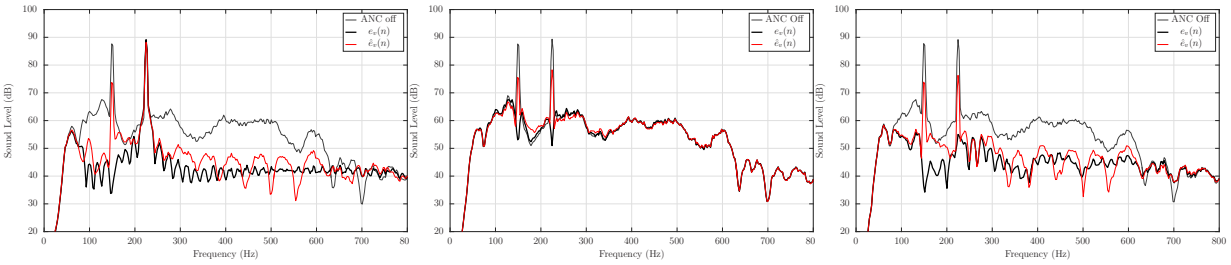

Figure C.3: Simulation results for feedforward, feedback, and hybrid control structures. Shown are the spectra obtained from directly minimizing the virtual pressure and minimizing the estimate. The reference signal consists of a 150 Hz tone and a broadband signal. The disturbance is the reference signal filtered through $P(z)$ plus an uncorrelated sinusoid of frequency 225 Hz.

pressure is directly minimized. As was the case in the first simulation, the feedforward controller minimizes only the disturbance correlated with the reference noise. The feedback controller achieves nearly 10 dB reduction in the narrow-band disturbances with minimal spillover. The hybrid controller again outperforms the others. Using the estimate of the virtual pressure rather than the direct measurement results in significantly less attenuation for the tonal disturbances. While the tones are almost completely canceled when minimizing the exact virtual pressure, $e_v(n)$, only a 10-15 dB reduction is achieved when minimizing the estimate, $\hat{e}_v(n)$. This is mainly due to modeling errors in the secondary path transfer functions. If perfect transfer function models are available, the attenuation levels obtained by minimizing $e_v(n)$ and $\hat{e}_v(n)$ are theoretically identical.

C.2 Control Experiments

The series of single channel ANC experiment depicted in Figure C.1 was carried out in a 3×3×4 m hemi-anechoic room where each of the scenarios described in the simulations were created. Simulink models of each control structure were built and an XPC Target computer was used to interface with the control system components. This machine is used with Simulink Real-Time

to compile Simulink models, download them to the target machine, and run themin real-time.

It has been clearly demonstrated that an advantage of the hybrid controller is its ability to attenuate uncorrelated narrow-band disturbances while maintaining the performance of a feedforward controller. This scenario is easy to devise in a simulation environment, but has not received much attention in ANC experiments. This is mainly because in laboratory experiments, the reference sensors are judiciously placed as to observe all of the disturbance components.

In these experiments, a novel method of creating disturbances described by Equation C.1 is implemented. This results in correlated broadband and narrow-band disturbances as well as uncorrelated narrow-band disturbances. The uncorrelated disturbance is created by passing the reference signal through a notch filter with notch frequency ω_n. The notch frequency is set equal to the tonal disturbance frequency ω_2=225 Hz. This results in a reference signal used by the controller that is coherent with the disturbance everywhere except ω_n.

Before operation of the ANC system, all secondary paths must be modeled in a preliminary identification stage. The secondary paths between the secondary source and the physical and virtual microphones, $G(z)$ and $G_v(z)$ respectively, are each modeled as FIR filters with 400 coefficients. The virtual path $O(z)$ is modeled as an FIR filter with 300 coefficients. Although the sensor at the virtual location is not used during operation of the ANC system, it remains in place to monitor control performance. In the first experiment, the controller aims to minimize the pressure directly measured at the virtual microphone, *i.e.*, no virtual sensing. This is the standard approach taken by most ANC systems. The results are shown in Figure C.4 and confirm the simulation results from Figure C.2. The feedforward controller attenuates all disturbances correlated with the reference. Only control of tonal disturbances is achieved by the feedback controller. The hybrid controller shows a reduction in both narrow-band and broadband disturbance components.

In the next experiment, the virtual microphone signal is not available and is estimated according to the remote microphone technique. The virtual microphone is located 10 cm from the physical microphone. The signal at the virtual location is estimated using the remote microphone technique, which accounts for the response between physical and virtual locations. A microphone at the virtual location is used to measure the true virtual signal. Results are shown in Figure C.5. Less attenuation is achieved over the disturbance bandwidth when using a virtual sensor. This may be attributed to inaccuracies in secondary path modeling. The hybrid controller again outperforms the feedforward and feedback controllers. The tonal disturbances are attenuated by 15-20 dB and the broadband disturbances are reduced by 10-15 dB.

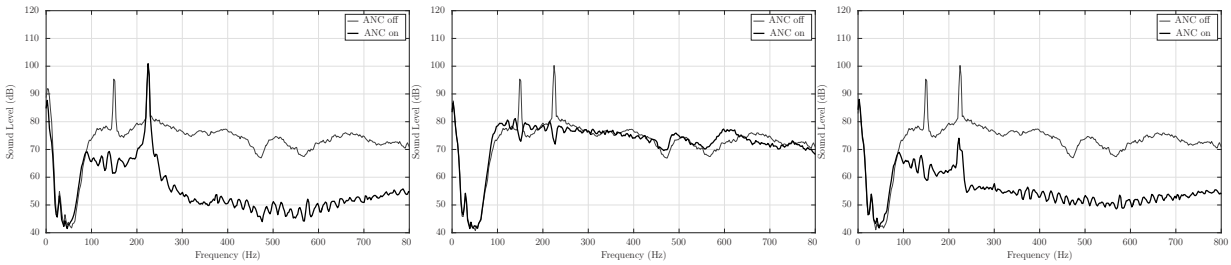

Figure C.4: Experimental results of minimizing the pressure directly at the physical error sensor. The reference signal consists of a 150 Hz tone and a broadband signal. The disturbance is the reference signal filtered through $P(z)$ plus an uncorrelated sinusoid of frequency 225 Hz.

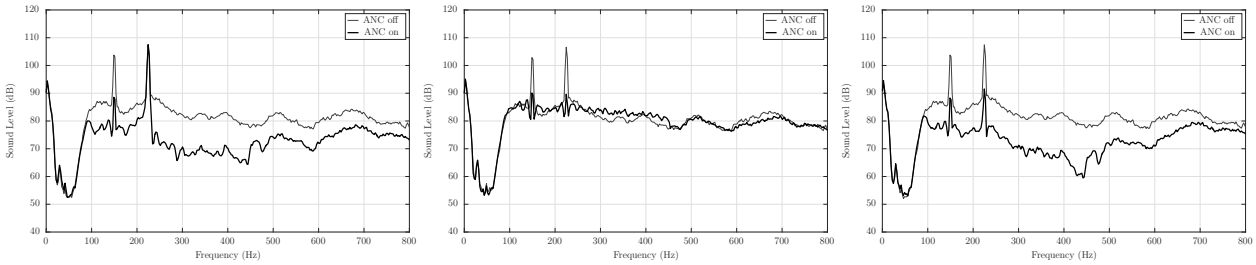

Figure C.5: Experimental results of minimizing the estimated pressure at the virtual location. The reference signal consists of a 150 Hz tone and a broadband signal. The disturbance is the reference signal filtered through $P(z)$ plus an uncorrelated sinusoid of frequency 225 Hz.

Bibliography

[1] C. Fuller, S. Elliott, and P. Nelson. *Active control of vibration*. Academic Press, 1996.

[2] S. Elliott. *Signal processing for active control*. Academic press, 2000.

[3] L. Paul. Process of silencing sound oscillations, June 9 1936. US Patent 2,043,416.

[4] J. Burgess. Active adaptive sound control in a duct: A computer simulation. *The Journal of the Acoustical Society of America*, 70(3):715–726, 1981.

[5] A. Hull, C. Radcliffe, and S. Southward. Global active noise control of a one-dimensional acoustic duct using a feedback controller. *Journal of Dynamic Systems, Measurement, and Control*, 115(3):488–494, 1993.

[6] C. Petersen, R. Fraanje, B. Cazzolato, A. Zander, and C. Hansen. A kalman filter approach to virtual sensing for active noise control. *Mechanical Systems and Signal Processing*, 22(2):490–508, 2008.

[7] P. Nelson, A. Curtis, S. Elliott, and A. Bullmore. The active minimization of harmonic enclosed sound fields, part i: Theory. *Journal of Sound and Vibration*, 117(1):1–13, 1987.

[8] A. Bullmore, P. Nelson, A. Curtis, and S. Elliott. The active minimization of harmonic enclosed sound fields, part ii: A computer simulation. *Journal of Sound and Vibration*, 117(1):15–33, 1987.

[9] S. Elliott, A. Curtis, A. Bullmore, and P. Nelson. The active minimization of harmonic enclosed sound fields, part iii: Experimental verification. *Journal of Sound and Vibration*, 117(1):35–58, 1987.

[10] J. Parkins, S. Sommerfeldt, and J. Tichy. Narrowband and broadband active control in an enclosure using the acoustic energy density. *The Journal of the Acoustical Society of America*, 108(1):192–203, 2000.

[11] Y. Park and S. Sommerfeldt. Global attenuation of broadband noise fields using energy density control. *The Journal of the Acoustical Society of America*, 101(1):350–359, 1997.

[12] S. Sommerfeldt and P. Nashif. An adaptive filtered-x algorithm for energy-based active control. *The Journal of the Acoustical Society of America*, 96(1):300–306, 1994.

[13] W. Gan and S. Kuo. An integrated audio and active noise control headset. *IEEE Transactions on Consumer Electronics*, 48(2):242–247, 2002.

[14] S. Elliott, P. Joseph, A. Bullmore, and P. Nelson. Active cancellation at a point in a pure tone diffuse sound field. *Journal of Sound and Vibration*, 120(1):183–189, 1988.

[15] S. Elliott and J. Garcia-Bonito. Active cancellation of pressure and pressure gradient in a diffuse sound field. *Journal of Sound and Vibration*, 186(4):696–704, 1995.

[16] J. Garcia-Bonito and S. Elliott. Active cancellation of acoustic pressure and particle velocity in the near field of a source. *Journal of Sound and Vibration*, 221(1):85–116, 1999.

[17] J. Garcia-Bonito, S. Elliott, and M. Bonilha. Active cancellation of pressure at a point in a pure tone diffracted diffuse sound field. *Journal of Sound and Vibration*, 201(1):43–65, 1997.

[18] S. Elliott and P. Nelson. Active noise control. *IEEE Signal Processing Magazine*, 10(4):12–35, 1993.

[19] S. Kuo and D. Morgan. *Active noise control systems: algorithms and DSP implementations*. John Wiley & Sons, Inc., 1995.

[20] S. Kuo and D. Morgan. Active noise control: a tutorial review. *Proceedings of the IEEE*, 87(6):943–973, 1999.

[21] S. Haykin. *Adaptive filter theory*. Pearson Education India, 2008.

[22] B. Widrow and S. Stearns. *Adaptive Signal Processing*. Prentice Hall, 1985.

[23] E. Bjarnason. Active noise cancellation using a modified form of the filtered-x LMS algorithm. *Proc. EUSIPCO'92, Signal Processing VI, Brussels, Belgium*, 2:1053–1056, 1992.

[24] E. Wan. Adjoint LMS: An efficient alternative to the filtered-x LMS and multiple error LMS algorithms. In *International Conference on Acoustics, Speech, and Signal Processing, 1996.*, volume 3, pages 1842–1845. IEEE, 1996.

[25] R. Fraanje, A. Sayed, M. Verhaegen, and N. Doelman. A fast-array kalman filter solution to active noise control. *International Journal of Adaptive Control and Signal Processing*, 19(2-3):125–152, 2005.

[26] S. Elliott, I. Stothers, and P. Nelson. A multiple error LMS algorithm and its application to the active control of sound and vibration. *IEEE Transactions on Acoustics, Speech, and Signal Processing*, 35(10):1423–1434, 1987.

[27] S. Elliott. Optimal controllers and adaptive controllers for multichannel feedforward control of stochastic disturbances. *IEEE Transactions on Signal Processing*, 48(4):1053–1060, 2000.

[28] R. Cabell and C. Fuller. A principal component algorithm for feedforward active noise and vibration control. *Journal of Sound and Vibration*, 227(1):159–181, 1999.

[29] R. Clark. Adaptive feedforward modal space control. *The Journal of the Acoustical Society of America*, 98(5):2639–2650, 1995.

[30] S. Gay. The fast affine projection algorithm. In *Acoustic Signal Processing for Telecommunication*, pages 23–45. Springer, 2000.

[31] R. Kwong and E. Johnston. A variable step size LMS algorithm. *IEEE Transactions on Signal Processing*, 40(7):1633–1642, 1992.

[32] Z. Bo, Chao. Sun, Y. Xu, and S. Jiang. A variable momentum factor filtered-x weighted accumulated LMS algorithm for narrowband active noise control systems. *Measurement*, 48:282–291, 2014.

[33] C. Ruckman and C. Fuller. Optimizing actuator locations in active noise control systems using subset selection. *Journal of Sound and Vibration*, 186(3):395–406, 1995.

[34] D. Morgan. An adaptive modal-based active control system. *The Journal of the Acoustical Society of America*, 89(1):248–256, 1991.

[35] J. Garcia-Bonito, S. Elliott, and C. Boucher. Generation of zones of quiet using a virtual microphone arrangement. *The Journal of the Acoustical Society of America*, 101(6):3498–3516, 1997.

[36] S. Elliott and A. David. A virtual microphone arrangement for local active sound control. In *Proceedings of the 1st International Conference on Motion and Vibration Control*, pages 1027–1031. Yokohama Japan, 1992.

[37] J. Vipperman, R. Burdisso, and C. Fuller. Active control of broadband structural vibration using the LMS adaptive algorithm. *Journal of Sound and Vibration*, 166(2):283–299, 1993.

[38] C. Fuller. Analysis of active control of sound radiation from elastic plates by force inputs. In *INTERNOISE and NOISE-CON Congress and Conference Proceedings*, volume 1988, pages 1061–1064. Institute of Noise Control Engineering, 1988.

[39] C. Fuller. Experiments on reduction of aircraft interior noise using active control of fuselage vibration. *The Journal of the Acoustical Society of America*, 78(S1):S88–S88, 1985.

[40] H. Olson and E. May. Electronic sound absorber. *The Journal of the Acoustical Society of America*, 25(6):1130–1136, 1953.

[41] J. Cheer and S. Elliott. Multichannel control systems for the attenuation of interior road noise in vehicles. *Mechanical Systems and Signal Processing*, 60-61:753–769, August 2015.

[42] D. Sachau. Feedback active noise control in a crew rest compartment mock-up. *SL: Structural Longevity*, 8(1):23–35, 2012.

[43] L. Macchi, J. Caillet, F. Marrot, and F. Simon. A feedback multi-tone algorithm for the control of helicopter gearbox noise in an active headrest. In *NOISE-CON*, 2014.

[44] J. Diaz, J. Egana, and J. Vinolas. A local active noise control system based on a virtual-microphone technique for railway sleeping vehicle applications. *Mechanical systems and Signal Processing*, 20(8):2259–2276, 2006.

[45] J. Cheer and S. Elliott. Active noise control of a diesel generator in a luxury yacht. *Applied Acoustics*, 105:209–214, 2016.

[46] J. Doyle, B. Francis, and A. Tannenbaum. *Feedback control theory*. Courier Corporation, 2013.

[47] B. Rafaely and S. Elliott. H_2/H_∞ active control of sound in a headrest: design and implementation. *IEEE Transactions on Control Systems Technology*, 7(1):79–84, 1999.

[48] B. Rafaely, S. Elliott, and J. Garcia-Bonito. Broadband performance of an active headrest. *The Journal of the Acoustical Society of America*, 106(2):787–793, 1999.

[49] M. Pawelczyk. Multiple input–multiple output adaptive feedback control strategies for the active headrest system: design and real-time implementation. *International Journal of Adaptive Control and Signal Processing*, 17(10):785–800, 2003.

[50] M. Pawelczyk. Adaptive noise control algorithms for active headrest system. *Control Engineering Practice*, 12(9):1101–1112, 2004.

[51] T. Shan and T. Kailath. Adaptive algorithms with an automatic gain control feature. *IEEE Transactions on Circuits and Systems*, 35(1):122–127, 1988.

[52] M. Morari and E. Zafiriou. *Robust process control*. Prentice Hall Englewood Cliffs, NJ, 1989.

[53] Y. Xiao, R. Ward, L. Ma, and A. Ikuta. A new LMS-based fourier analyzer in the presence of frequency mismatch and applications. *IEEE Transactions on Circuits and Systems I: Regular Papers*, 52(1):230–245, 2005.

[54] A. Nehorai. A minimal parameter adaptive notch filter with constrained poles and zeros. *IEEE Transactions on Acoustics, Speech, and Signal Processing*, 33(4):983–996, 1985.

[55] E. Kim, B. Kim, and S. Lee. Active noise control in a duct system based on a frequency-estimation algorithm and the FxLMS algorithm. *International Journal of Automotive Technology*, 14(2):291–299, 2013.

[56] M. Bodson and S. Douglas. Adaptive algorithms for the rejection of sinusoidal disturbances with unknown frequency. *Automatica*, 33(12):2213–2221, 1997.

[57] J. Yang and M. Kaveh. Adaptive eigensubspace algorithms for direction or frequency estimation and tracking. *IEEE Transactions on Acoustics, Speech, and Signal Processing*, 36(2):241–251, 1988.

[58] B. Sayyarrodsari, J. How, B. Hassibi, and A. Carrier. An H_∞-optimal alternative to the fxlms algorithm. In *Proceedings of American Control Conference*, volume 2, pages 1116–1121. IEEE, 1998.

[59] S. Yu and J. Hu. Controller design for active noise cancellation headphones using experimental raw data. *IEEE/ASME Transactions on Mechatronics*, 6(4):483–490, 2001.

[60] C. Bao, R. Paurobally, and J. Pan. Design and test of a feedback controller for attenuating low frequency noise in a room. *Acoustics Australia*, 37(2-61), 2009.

[61] D. Cox, G. Gibbs, R. Clark, and J. Vipperman. Experimental robust control of structural acoustic radiation. *ASME Journal of Vibration and Acoustics*, 121:433–439, 1999.

[62] Y. Zhou, Q. Zhang, X. Li, and W. Gan. On the use of an SPSA-based model-free feedback controller in active noise control for periodic disturbances in a duct. *Journal of Sound and Vibration*, 317(3):456–472, 2008.

[63] R. Clark and G. Gibbs. A novel approach to feedforward higher-harmonic control. *The Journal of the Acoustical Society of America*, 96(2):926–936, 1994.

[64] D. Kewley, R. Clark, and S. Southward. Feedforward control using the higher-harmonic, time-averaged gradient descent algorithm. *The Journal of the Acoustical Society of America*, 97(5):2892–2905, 1995.

[65] M. Vaudrey, W. Baumann, and W. Saunders. Time-averaged gradient control of thermoacoustic instabilities. *Journal of Propulsion and Power*, 19(5):830–836, 2003.

[66] L. Wu, X. Qiu, I. Burnett, E. Cheng, and Y. Guo. A decoupled hybrid structure for active noise control with uncorrelated narrowband disturbances. In *Inter. Noise 2014*, pages 1–9. Australian Acoustical Society, 2014.

[67] H. Sakai, T. Someda, and S. Miyagi. Analysis of an adaptive filter algorithm for hybrid anc system. In *Acoustics, Speech, and Signal Processing (ICASSP)*, volume 2, pages II–1553. IEEE, 2002.

[68] L. Wu, X. Qiu, I. Burnett, and Y. Guo. Decoupling feedforward and feedback structures in hybrid active noise control systems for uncorrelated narrowband disturbances. *Journal of Sound and Vibration*, 350:1–10, 2015.

[69] K. Beemanpally, K. Pottim, and S. Kuo. Multi-channel hybrid active noise control system for infant incubators. In *Electro/Information Technology (EIT), 2010 IEEE International Conference on*, pages 1–8. IEEE, 2010.

[70] L. Ray, J. Solbeck, A. Streeter, and R. Collier. Hybrid feedforward-feedback active noise reduction for hearing protection and communication. *The Journal of the Acoustical Society of America*, 120(4):2026–2036, 2006.

[71] B. Rafaely and M. Jones. Combined feedback-feedforward active noise-reducing headset - The effect of the acoustics on broadband performance. *The Journal of the Acoustical Society of America*, 112(3):981–989, 2002.

[72] A. Streeter, L. Ray, and R. Collier. Hybrid feedforward-feedback active noise control. In *American Control Conference*, volume 3, pages 2876–2881. IEEE, 2004.

[73] R. Castane-Selga and R. Pena. Active noise hybrid time-varying control for motorcycle helmets. *IEEE Transactions on Control Systems Technology*, 18(3):602–612, 2010.

[74] W. Tseng, B. Rafaely, and S. Elliott. Combined feedback–feedforward active control of sound in a room. *The Journal of the Acoustical Society of America*, 104(6):3417–3425, 1998.

[75] M. Akhtar and W. Mitsuhashi. Improving performance of hybrid active noise control systems for uncorrelated narrowband disturbances. *IEEE transactions on Audio, Speech, and Language Processing*, 19(7):2058–2066, 2011.

[76] X. Kong, P. Liu, and S. Kuo. Multiple channel hybrid active noise control systems. *IEEE transactions on Control Systems Technology*, 6(6):719–729, 1998.

[77] A. Roure and A. Albarrazin. The remote microphone technique for active noise control. In *INTERNOISE and NOISE-CON Congress and Conference Proceedings*, volume 1999, pages 1233–1244. Institute of Noise Control Engineering, 1999.

[78] C. Radcliffe and S. Gogate. Model based feedforward noise control algorithm for vehicle interiors. *AMSE, Dynamic Systems and Control Division*, 52:299–304, 1993.

[79] D. Moreau, B. Cazzolato, A. Zander, and C. Petersen. A review of virtual sensing algorithms for active noise control. *Algorithms*, 1(2):69–99, 2008.

[80] D. Das, D. Moreau, and B. Cazzolato. Performance evaluation of an active headrest using the remote microphone technique. *Proceedings of Acoustics*, 2011.

[81] B. Cazzolato. *Sensing systems for active control of sound transmission into cavities*. PhD thesis, 1999.

[82] B. Cazzolato. An adaptive LMS virtual microphone. In *INTERNOISE and NOISE-CON Congress and Conference Proceedings*, number 7, pages 105–116. Institute of Noise Control Engineering, 2002.

[83] D. Moreau, J. Ghan, B. Cazzolato, and A. Zander. Active noise control in a pure tone diffuse sound field using virtual sensing. *The Journal of the Acoustical Society of America*, 125(6):3742–3755, 2009.

[84] L. Ljung and T. Söderström. *Theory and practice of recursive identification*, volume 5. JSTOR, 1983.

[85] J. Shynk. Adaptive IIR filtering. *IEEE ASSP Magazine*, 6(2):4–21, 1989.

[86] J. Cioffi and T. Kailath. Fast, recursive-least-squares transversal filters for adaptive filtering. *IEEE Transactions on Acoustics, Speech, and Signal Processing*, 32(2):304–337, 1984.

[87] A. Wang and W. Ren. Convergence analysis of the filtered-U algorithm for active noise control. *Signal Processing*, 73(3):255–266, 1999.

[88] P. Nelson and S. Elliott. *Active control of sound*. Academic press, 1991.

[89] S. Elliot, P. Nelson, I. Stothers, and C. Boucher. In-flight experiments on the active control of propeller-induced cabin noise. *Journal of Sound and Vibration*, 140(2):219–238, 1990.

[90] N. Schiller, R. Cabell, and C. Fuller. Decentralized control of sound radiation using iterative loop recovery. *The Journal of the Acoustical Society of America*, 128(4):1729–1737, 2010.

[91] G. Golub and C. Van Loan. *Matrix computations*, volume 3. JHU Press, 2012.

[92] Y. Song, Y. Gong, and S. Kuo. A robust hybrid feedback active noise cancellation headset. *IEEE transactions on Speech and Audio Processing*, 13(4):607–617, 2005.

[93] B. Rafaely. *Feedback control of sound*. PhD thesis, 1997.

[94] S. Skogestad and I. Postlethwaite. *Multivariable feedback control: analysis and design*, volume 2. Wiley New York, 2007.

[95] B. Rafaely and S. Elliott. Adaptive internal model controller: Stability analysis. In *International congress on noise control engineering*, pages 983–988, 1996.

[96] J. Doyle, K. Glover, P. Khargonekar, and B. Francis. State-space solutions to standard H_2 and H_∞ control problems. *IEEE Transactions on Automatic control*, 34(8):831–847, 1989.

[97] M. Sternad and A. Ahlén. Robust filtering and feedforward control based on probabilistic descriptions of model errors. *Automatica*, 29(3):661–679, 1993.

[98] G. Goodwin and D. Miller. Robust performance optimization based on stochastic model errors: the stable case. *International Journal of Robust and Nonlinear Control*, 12(14):1191–1208, 2002.

[99] A. MacFarlane and I. Postlethwaite. The generalized nyquist stability criterion and multivariable root loci. *International Journal of Control*, 25(1):81–127, 1977.

[100] S. Elliott and T. Sutton. Performance of feedforward and feedback systems for active control. *IEEE Transactions on Speech and Audio Processing*, 4(3):214–223, 1996.

[101] M. Vaudrey, W. Baumann, and W. Saunders. Stability and operating constraints of adaptive LMS-based feedback control. *Automatica*, 39(4):595–605, 2003.

[102] D. Smith and A. Jackman. Space launch system. 2016.

[103] N. Schiller, A. Allen, J. Herlan, and B. Rosenthal. Experimental evaluation of tuned chamber core panels for payload fairing noise control. In *Aerospace Testing Seminar*, 2015.

[104] N. Schiller, A. Allen, B. Zalewski, and B. Beck. Sound transmission loss through a corrugated-core sandwich panel with integrated acoustic resonators. In *Proceedings of the ASME 2014 International Mechanical Engineering Congress & Exposition*, 2014.

[105] COMSOL Multiphysics. Comsol multiphysics user guide (version 4.3 a). *COMSOL, AB*, 2012.

[106] B. Rafaely. Spatial-temporal correlation of a diffuse sound field. *The Journal of the Acoustical Society of America*, 107(6):3254–3258, 2000.

[107] F. Jacobsen. The diffuse sound field. *The Acoustics Laboratory, Technical University of Denmark, Report*, (27), 1979.

[108] A. David and S. Elliott. Numerical studies of actively generated quiet zones. *Applied Acoustics*, 41(1):63–79, 1994.

[109] R. Cook, R. Waterhouse, R. Berendt, S. Edelman, and M. Thompson Jr. Measurement of correlation coefficients in reverberant sound fields. *The Journal of the Acoustical Society of America*, 27(6):1072–1077, 1955.

[110] S. Elliott and J. Cheer. Modeling local active sound control with remote sensors in spatially random pressure fields. *The Journal of the Acoustical Society of America*, 137(4):1936–1946, 2015.

[111] F. Grosveld. Characterization of the reverberation chamber at the nasa langley structural acoustics loads and transmission (SALT) facility. 2013.

[112] F. Grosveld. Calibration of the structural acoustics loads and transmission facility at nasa langley research center. In *INTERNOISE and NOISE-CON Congress and Conference Proceedings*, number 2, pages 1541–1546. Institute of Noise Control Engineering, 1999.

[113] P. Morse and K. Ingard. *Theoretical acoustics*. Princeton University Press, 1968.

[114] T. Schultz. Diffusion in reverberation rooms. *Journal of Sound and Vibration*, 16(1):17–28, 1971.

[115] M. Schroeder. Die statistischen parameter der frequenzkurven von groβen räumen. *Acta Acustica united with Acustica*, 4(5):594–600, 1954.

[116] H. Kuttruff. *Room acoustics*. Crc Press, 2016.

[117] P. Joseph, S. Elliott, and P. Nelson. Near field zones of quiet. *Journal of Sound and Vibration*, 172(5):605–627, 1994.